Characterization and Modeling to Improve Efficiency of the $0.946\mu m$ Nd:YAG Laser

by

Ryan M. Springer

A dissertation submitted to The Johns Hopkins University in conformity with the requirements for the degree of Doctor of Philosophy.

Baltimore, Maryland

October, 2015

Distribution Statement A - Approved for public release; distribution is unlimited, as submitted under NAVAIR Public Release Authorization 2015-811.

Abstract

The Nd:YAG laser has become a critical part of optical science since it was first demonstrated at Bell Labs in 1964. The $0.946\mu m$ transition in Nd:YAG is of particular interest for two reasons: the proximity of $0.946\mu m$ to the peak responsivity of silicon photodiodes and the increased transmittance through ocean waters of the frequency doubled $0.946\mu m$ emission. The author hypothesizes that a more through characterization and modeling of Nd:YAG gain media will enable more accurate laser design models, leading to improved efficiency and greater average power $0.946\mu m$ Nd:YAG laser systems.

Materials under study include undoped, 1%, 1.5%, 2%, 4%, 6%, and 10% atomic (at.) Nd doped polycrystalline YAG, and undoped and 1% (at.) Nd doped single crystal YAG. Advantages of polycrystalline versus single crystal material include higher maximum doping percentage, tailored non-uniform doping deposition, and reduced material strain.

Room temperature transmittance measurements for all samples are performed between the mid-infrared and ultraviolet edge of absorption band. Temperature de-

ABSTRACT

pendent transmittance measurements are conducted on 1% and 6% polycrystalline Nd:YAG material. The temperature dependent stimulated emission cross section is determined for Nd:YAG at $0.946\mu m$.

In-plane bidirectional scatterance distribution function (BSDF) measurements are collected at multiple discrete wavelengths from $0.405\mu m$ to $1.55\mu m$ for all samples. Scatterance data is fit to standard models and a total integrated scatter (TIS) for each sample at various wavelengths is determined. A coated sphere anomalous diffraction (ADA) model is developed and applied to polycrystalline material. A Kubelka-Munk wavelength dependent diffuse scatter coefficient model is developed using the ADA model.

Fluorescence and absorption derived line width measurements for polycrystalline Nd doped YAG are reported. Polycrystalline YAG material is found to have broader intrinsic line width than single crystal material.

This work is the first known full characterization of the optical properties with this polycrystalline host. A comparison of strengths and weaknesses of single crystal and polycrystalline is presented.

Primary Reader: Dr. Jacob Khurgin

Secondary Reader: Dr. Michael E. Thomas

Acknowledgments

I want to acknowledge the support I have received from many individuals. First, I want to recognize the extensive guidance and tremendous support of my longtime advisor and mentor Dr. Michael E. Thomas. He has made a very personal commitment to my academic and professional progress. Dr. Thomas's knowledge, patience, confidence and encouragement were instrumental in my accomplishments.

I want to thank my research advisor Dr. Jacob B. Khurgin for his instruction, guidance, and for his efforts as reader. I want to thank Dr. James B. Spicer for several critical discussions, laboratory support, and participation on my dissertation committee. I want to thank Dr. Amy C. Foster for her participation on my dissertation committee.

I want to acknowledge Dr. Richard I. Joseph, Mr. Marc B. Airola, Dr. David M. Brown, Dr. Andrea M. Brown, Mr. Daniel V. Hahn of Johns Hopkins University, Applied Physics Laboratory for generously sharing their knowledge, time, and laboratory space.

I gratefully acknowledge the support and guidance of Dr. Frank Narducci, Dr.

ACKNOWLEDGMENTS

Linda Mullen, Mr. Brian Concannon, Dr. Jon Davis, Mr. Alan Laux, and Mr. Thomas Hamilton of the Naval Air Warfare Center Aircraft Division, Patuxent River, MD. Finally, I want to thank Dr. James B. Sheehy and Mr. Kevin Birney for their financial support through the Section 219 Naval Innovative Science and Engineering (NISE) Workforce Development program at the Naval Air Warfare Center Aircraft Division, Patuxent River, MD.

Dedication

This thesis is dedicated Dr. Pushap P. K. Sidhu for her love and support.

Contents

List of Tables

List of Figures

Chapter 1

Introduction

1.1 History of Nd:YAG Laser

The first continuous and pulsed lasing of Nd doped Yttrium Aluminum Garnet (YAG) was demonstrated by Geusic, et al. at Bell Labs in 1964.[1] The laser built at Bell Labs operated on the widely used $1.064\mu m$ Nd:YAG transition. Since 1964, the Nd:YAG laser has become a workhorse laser for many applications. The first laser based on the less common and lower gain $0.946\mu m$ transition in Nd doped YAG was demonstrated by Wallace and Harris.[2] Interest in this lasing line is because $0.946\mu m$ is very close to the peak responsivity for silicon detectors, almost an order of magnitude higher responsivity than at $1.064\mu m$. Furthermore, $0.946\mu m$ can be frequency doubled to $0.473\mu m$, an advantageous wavelength for maximum transmittance through open ocean waters.[3,4]

The greatest known energy per pulse using the $0.946\mu m$ transition was 150mJ per pulse, 1 Hz pulse repetition rate (PRF) at room temperature, accomplished by Axenson et al.[5] The highest known repetition rate using the $0.946\mu m$ transition was 60μJ/pulse, 50kHz PRF at room temperature demonstrated by Chen, et al.[6] The average power output reported by Axenson and Chen was 150mW and 2.25W, respectively. There are no known $0.946\mu m$ laser systems with output energy that exceeds 1mJ/pulse and PRF greater than 1kHz. To achieve these specifications the efficiency of the laser system must be improved. Significant characterization work on single crystal YAG material has been conducted.[7–13] A complete characterization of the optical properties of Nd:YAG is required for efficient laser design.

1.2 Nd:YAG Energy Level Diagram

An energy level diagram of common Nd:YAG lasing transitions is presented in Fig. 1.1.[14–16] The $0.946\mu m$ transition of interest is highlighted in red. The $0.946\mu m$ transition in Nd:YAG terminates in the upper stark split state ($852cm^{-1}$) of the ground state manifold, leading to reabsorption losses due to thermal population of the lower laser level. The stimulated emission cross section for the $0.946\mu m$ transition is roughly an order of magnitude smaller than at $1.064\mu m$.[17]

1.3 Characterization and Modeling

An analysis of the transmittance of commercially available polycrystalline and single crystal Nd:YAG gain media is conducted. Absorption coefficient and absorption cross section is calculated for all Nd transitions in the $0.19\mu m$ to $10\mu m$ spectral range. A classical oscillator model for the $0.808\mu m$ pump region is developed. Temperature dependant transmittance data is collected and the temperature dependant, $0.946\mu m$ transition stimulated emission cross section is derived. Deriving stimulated emission cross section data from transmittance data is a departure from the standard practice; generally the stimulated emission cross section is derived from fluorescence lifetime data. Advantages of transmittance technique to be described later. The measured stimulated emission cross section for the $0.946\mu m$ transition is a factor of eight less than the $1.064\mu m$

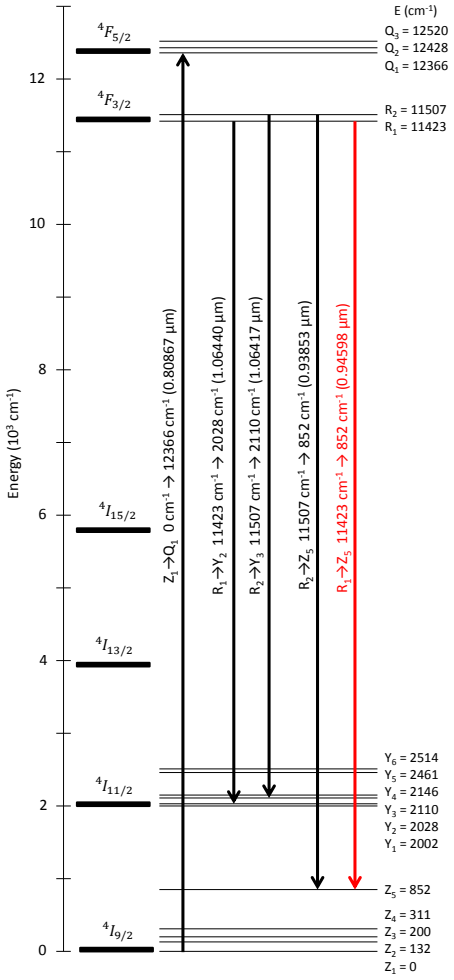

Figure 1.1: Energy level diagram of Nd:YAG showing the preferred $0.80867\mu m$ pump and $1.06440\mu m$, $1.06417\mu m$, $0.94598\mu m$, $0.93853\mu m$ lasing transitions. The $0.946\mu m$ transition of interest is highlighted in red.

transition.[18]

An analysis of the extrinsic scatterance of commercially available polycrystalline and single crystal Nd:YAG gain media is conducted. Interest in YAG scatter is high; of particular interest are the scatter losses at $0.946\mu m$ and $1.064\mu m$. Bidirectional scatter distribution function (BSDF) measurements are conducted on all samples at discrete wavelengths in the $0.405\mu m$ to $1.55\mu m$ spectral range and a total integrated scatter (TIS) is calculated. An Anomalous Diffraction Approximation (ADA) model is developed, using known methods of scatter in single crystal and polycrystalline YAG. Kubelka-Munk theory is used to fit ADA model to discrete TIS measurements, providing an estimate of TIS across the $0.405\mu m$ to $1.55\mu m$ spectral range.[19]

Room temperature fluorescence and absorption derived line width measurements on the 1% Nd doped YAG ${}^4I_{9/2} \rightarrow {}^4F_{3/2}$ and ${}^4I_{11/2} \rightarrow {}^4F_{3/2}$ transition manifolds were performed. Deriving an accurate line width measurement from fluorescence data can be difficult as the system noise floor may obscure a significant percentage of fluorescence signal. Improper selection of a fluorescence threshold will lead to an artificially narrow line width measurement. Determining the threshold for absorption derived line width measurements is straightforward. Absorption threshold is the lossless transmittance through the material derived from the single surface power reflection and Sellmeier refractive index model. Fluorescence line width measurements were compared with previously published fluorescence derived values and found consistent. Comparison of absorption and fluorescence line width measurements were

found to be broadly similar, validating the approach.

Absorption derived line width measurements are an objectively superior method. Temperature dependant, absorption derived line width measurements were conducted on 1% and 6% Nd doped YAG ${}^4I_{9/2} \rightarrow {}^4F_{3/2}$ and ${}^4I_{11/2} \rightarrow {}^4F_{3/2}$ transition manifolds. A Lorentz line shape model is fit to all absorption features. McCumber theory[20] and a model by Kushida[9] is applied to determine the temperature dependance of measured line widths. An increase in Nd:YAG ${}^4I_{9/2} \rightarrow {}^4F_{3/2}$ and ${}^4I_{11/2} \rightarrow {}^4F_{3/2}$ transition line width in polycrystalline versus single crystal material was measured. The minimum pulse length at $1.064\mu m$ should be roughly $3.6ps$ and $6.7ps$ for polycrystalline and single crystal respectively; the minimum pulse length at $0.946\mu m$ should be $2.8ps$ and $3.7ps$ for polycrystalline and single crystal respectively. This increased bandwidth indicates that mode locked laser systems based on polycrystalline Nd:YAG material are capable of shorter picosecond pulses than previously demonstrated.

This dissertation is a thorough analysis of the absorption, extrinsic scatterance, and fluorescence line width properties of available polycrystalline and single crystal, undoped and Nd doped YAG gain media, from visible to near infrared (NIR). A more complete understanding of the properties of YAG will lead to higher quality laser performance models and a more efficient $0.946\mu m$ laser design. Ideal thermal design will cool the gain media such that reabsorption losses are below scatter losses. Using the results from Refs.,[18,19] we now know at what temperature scatter losses will dominate.

Polycrystalline Nd:YAG gain media has improved substantially over the years. This work represents characterization of the highest quality polycrystalline material currently available. Selected relevant papers include early lasing of Polycrystalline Nd:YAG,[21] history and production methods,[22],[23] comparison between single crystal and polycrystalline Nd:YAG,[24] fluorescence,[25] thermal properties,[26] and power broadening.[27]

1.4 Nd:YAG Material

Single crystal YAG, undoped and Nd doped up to 1%, are available from multiple commercial manufacturers. Polycrystalline YAG, undoped and Nd doped up to 6%, are available from a limited number of manufacturers. The production process for polycrystalline material is challenging. A limited number of manufacturers are able to produce material of sufficient optical quality for use as laser gain media. Advantages of polycrystalline material include higher dopant levels and the ability to vary doping concentration with position.

The materials in this work include polycrystalline undoped and Nd doped YAG in percentages of 1, 1.5, 2, 4, 6, and 10% atomic (at.) from Konoshima Chemical Company Japan and single crystal undoped and Nd doped YAG at 1% at. from United Crystals Company. Atomic percentage is percent of Yittria atoms, from YAG lattice, replaced by Neodymium atoms. A picture of polycrystalline and single crystal

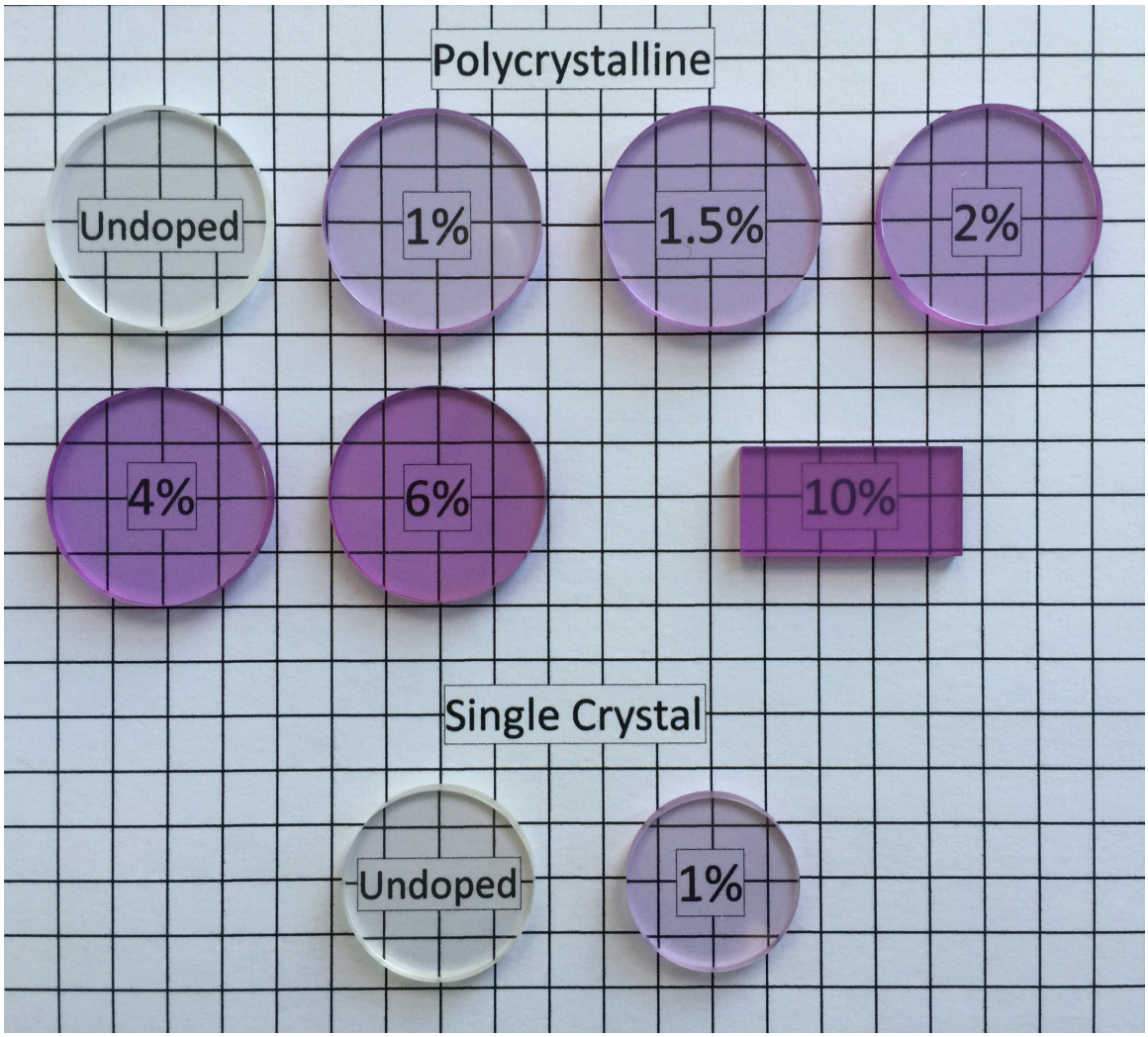

Figure 1.2: Samples under test include undoped and 1% to 10% Nd doped polycrystalline YAG and undoped and 1% Nd doped single crystal YAG. Background grid is 12.5mm spacing.

samples measured is shown in Fig. 1.2. Visual inspection of the undoped and 1% to 6% Nd doped polycrystalline YAG samples indicates a high optical quality without obvious scatter; the 10% Nd doped polycrystalline YAG sample has notable haze. The undoped and 1% Nd doped single crystal YAG samples are also of high optical quality without obvious scatter. All Nd doped samples have ruby coloring with intensity of coloring increasing with dopant concentration. Samples were polished to 10/5 scratch dig and uncoated. Scanning electron microscope imaging was performed on the samples to allow grain size measurement. The average grain size was determined using Heyn Linear Intercept Procedure, as specified in ASTM E112-10 Standard Test Methods for Determining Average Grain Size.[28] The average grain size of the undoped and 1% to 6% Nd doped polycrystalline YAG samples was about $1\mu m$. Our grain size compares favorably to the grain size measurement of about $2\mu m$ reported by H. Yagi, et. al.[29] Material dimensions are provided in Table 1.1.

Sample	*Dia*(mm)	*Thickness*(mm)
Konoshima undoped YAG	25.0	3.3
Konoshima 1.0% Nd:YAG	25.0	0.75, 3.3
Konoshima 1.5% Nd:YAG	25.0	0.75, 3.3
Konoshima 2.0% Nd:YAG	25.0	0.75, 3.3
Konoshima 4.0% Nd:YAG	25.0	0.75, 3.3
Konoshima 6.0% Nd:YAG	25.0	0.75, 3.0
Konoshima 10.0% Nd:YAG	12.7 x 25.4	2.5
United Crystals undoped YAG	22.0	3.0
United Crystals 1.0% Nd:YAG	20.0	3.0

Table 1.1: Dimensions of samples under test. All samples are round except the 10% doped sample is rectangular.

Gain media thermal effects are important for the high energy laser community.

The refractive index of YAG is temperature dependant. High intracavity power density in a YAG based laser resonator will lead to significant thermooptic and photoelastic effects. Strong optical pumping causes the thermooptic effect and will lead to thermal focusing. An excellent paper comparing the thermooptic effect in polycrystalline and single crystal YAG was published by Furuse.[30] The photoelastic effect will cause birefringence leading to depolarization. For ultra high power laser systems, we speculate the photoelastic effect may be stronger in polycrystalline YAG. A laser resonator design should attempt to compensate for these thermal mechanisms.[31–33] This manuscript is concentrated on extrinsic scatter processes and will not focus on thermal effects of high power laser design.

1.5 Synthesis of Polycrystalline YAG

Polycrystalline YAG material is synthesized from extremely high purity Al_2O_3, Y_20_3 and Nd_2O_3 nano-crystalline powders. These powders are combined at the appropriate stoichiometric ratio for YAl_30_{12} plus the desired Nd doping percentage. A sintering or flow agent is added and the resultant mixture is homogenized by ball milling for several hours. The homogeneous mixture is spray dried and pressed into simple shapes using a hot isostatic press. Material is then brought to full 100% theoretical density using a high temperature vacuum sintering technique[34].[35]

1.6 Motivation of $0.946\mu m$ Nd:YAG Laser

Interest in the $0.946\mu m$ transition of Nd:YAG is driven by LIDAR design, increased spectral response of silicon photodiodes at $0.946\mu m$ vs. $1.064\mu m$, and decreased optical attenuation in the open ocean at the $0.473\mu m$ vs. $0.532\mu m$, the frequency doubled wavelengths of $0.946\mu m$ and $1.064\mu m$ respectively.

The LIDAR equation is given in Eq. 1.1, where Φ_r is the received power, Φ_t the transmitted power, $\tau(R)$ the optical path transmittance, $\Delta\Omega$ the optical system solid angle, $\rho(0,\pi)$ the target back reflectance, ξ the optical system collection efficiency, $\Phi_{background}$ the background flux, and $\Phi_{detector}$ the detector noise equivalent power.[36]

$$\Phi_r(R) = \Phi_t \tau(R) \Delta\Omega \rho(0,\pi) \tau(R) \xi + \Phi_{background} + \Phi_{detector} \tag{1.1}$$

1.6.1 Atmospheric LIDAR - Increased Photodiode Sensitivity at $0.946\mu m$ vs $1.064\mu m$

The typical responsivity of a silicon photodiode is approximately $0.661 A/W$ at $0.946\mu m$ compared with $0.277 A/W$ at $1.064\mu m$. Figure 1.3 is the typical silicon photodiode responsivity as reported in the National Bureau of Standards Special Publication 250-17.[37] The quantum efficiency of IR enhanced silicon avalanche photodiodes (APD) is approximately 45% at $0.946\mu m$ compared with 5% at $1.064\mu m$.[38] An increase in Si photodiode responsivity or APD quantum efficiency, included in

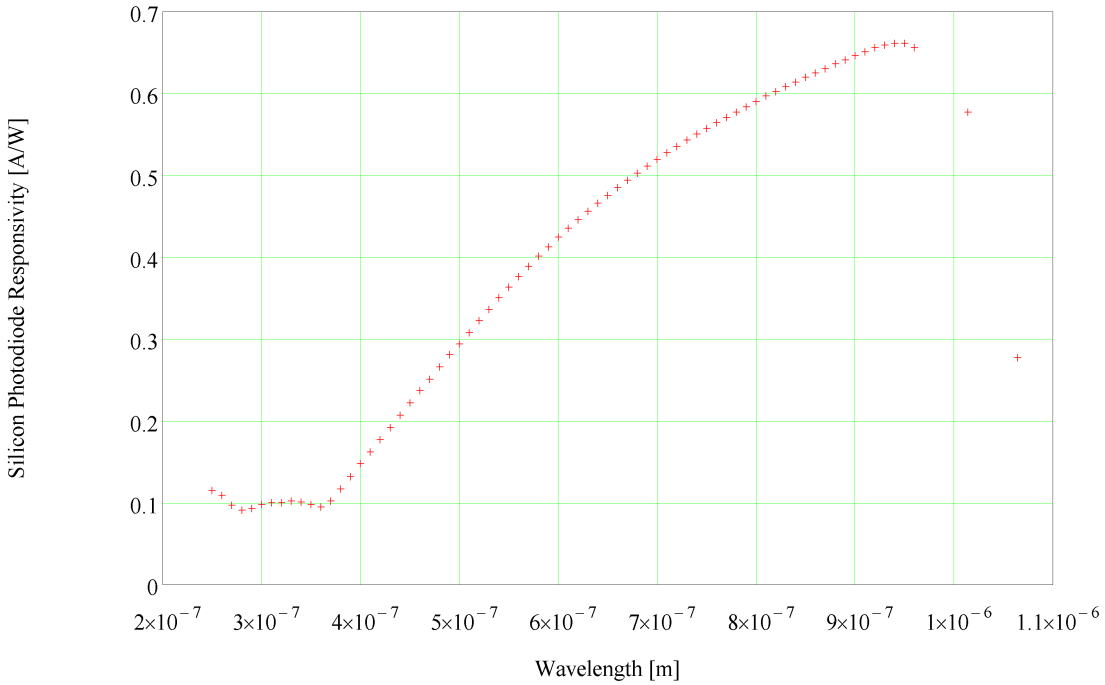

Figure 1.3: Typical silicon photodiode responsivity.

determination of ξ, will permit a decrease in transmitted power, Φ_t, with no change in the received power, Φ_r, assuming no change in optical path transmittance $\tau(R)$.

1.6.2 Oceanic LIDAR - Decreased Optical Attenuation at $0.473\mu m$ vs $0.532\mu m$

Laser emission at $0.946\mu m$ and $1.064nm\mu m$ can be frequency doubled to $0.473\mu m$ and $0.532\mu m$, respectively. Figure 1.4 is the optical path transmittance $\tau(R)$ through 100m of Jerlov water types I, IA, IB, II, and III.[4] For LIDAR operated in the underwater ocean environment, there is appreciably greater optical path transmittance

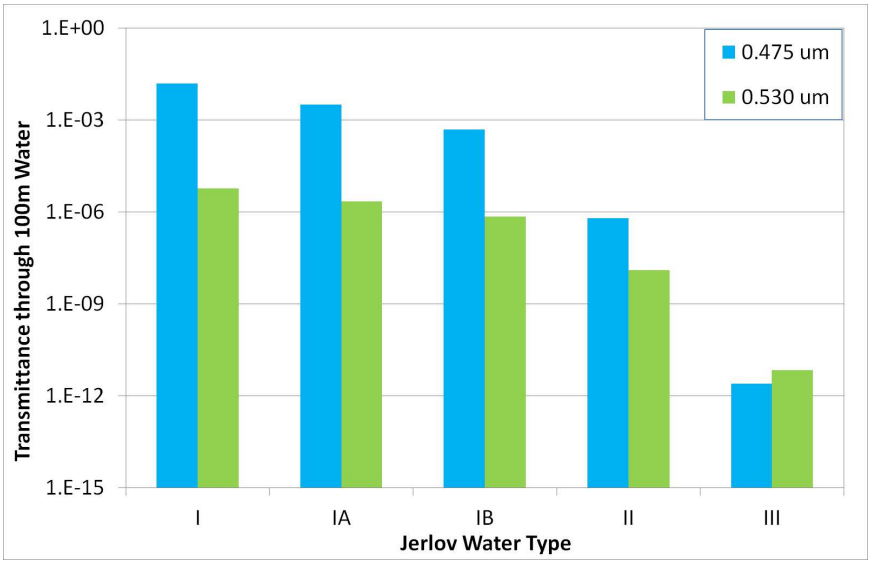

Figure 1.4: Transmittance of $0.475\mu m$ and $0.530\mu m$ photons through 100 meters of ocean by Jerlov water type.

at $0.473\mu m$ vs $0.532\mu m$ in Jerlov ocean water types I, IA, IB, and II.[4] The optical path transmittance term is present twice in the LIDAR equation, affecting the photons from transmitter to target and from target back to the receiver, therefore even a small increase in transmittance will lead to a substantial increase in lidar range.

Chapter 2

Experimental Setup

2.1 Transmittance

Transmittance data is important as it provides abundant information on material properties. For doped crystalline hosts, the absorption coefficient, absorption cross section, stimulated emission cross section, and transition line widths can be derived. Information on parasitic dopants can also be determined.

Transmittance data was collected over the $1000cm^{-1}$ to $52,500cm^{-1}$ ($10\mu m$ to $0.8\mu m$) spectral region using a combination of a fourier transform spectrometer and grating spectrometer. A variety of detectors and sources were used to cover this extended range. Data from each instrument and detector was individually calibrated. Overlapping spectral data was collected to permit alignment and cropping based on optimal responsivity of the detector.

2.1.1 Room Temperature Transmittance

Measurement data are collected using a BOMEM DA3.02 Fourier Transform Spectrometer in the $12,500cm^{-1}$ to $1,000cm^{-1}$ ($0.8\mu m$ to $10\mu m$) spectral region with a resolution of $2cm^{-1}$. A PerkinElmer Lambda 950 Grating Spectrometer is used in the to $0.19\mu m$ to $0.8\mu m$ ($52,500cm^{-1}$ to $12,500cm^{-1}$) spectral region with a resolution of 0.25nm ($2.5cm^{-1}$ at $10,000cm^{-1}$). Data from separate instruments are merged by aligning common spectral features. Data is further calibrated using optical transmission of stabilized laser sources. The absolute accuracy of room temperature transmittance measurements is estimated to be $\Delta\tau \approx 0.001$.

2.1.1.1 BOMEM Fourier Transform Spectrometer

A BOMEM DA3.02 Fourier Transform Spectrometer is based on a Michelson Interferemeter design, Fig 2.1. This instrument is used in the $12,500cm^{-1}$ to $1000cm^{-1}$ ($0.8\mu m$ to $10\mu m$) spectral region with a resolution of $2cm^{-1}$. A limited set of data was acquired with a higher resolution of $0.5cm^{-1}$ and found not to be necessary. The BOMEM spectrometer is configured with multiple sources, beam splitters, and detectors to allow this range of spectral coverage. A Globar source, KBr beam splitter and MCT detector are used from $4000cm^{-1}$ to $1000cm^{-1}$. A quartz-halogen lamp, quartz beam splitter, and InSb detector are used from $9000cm^{-1}$ to $4000cm^{-1}$. A quartz-halogen lamp, quartz beam splitter, and Si detector are used from $12,500cm^{-1}$ to $9000cm^{-1}$. Measurements in the $12,500cm^{-1}$ to $1000cm^{-1}$ spectral range are per-

formed under 0.5 - 2 torr vacuum to remove water vapor and carbon dioxide absorption bands.

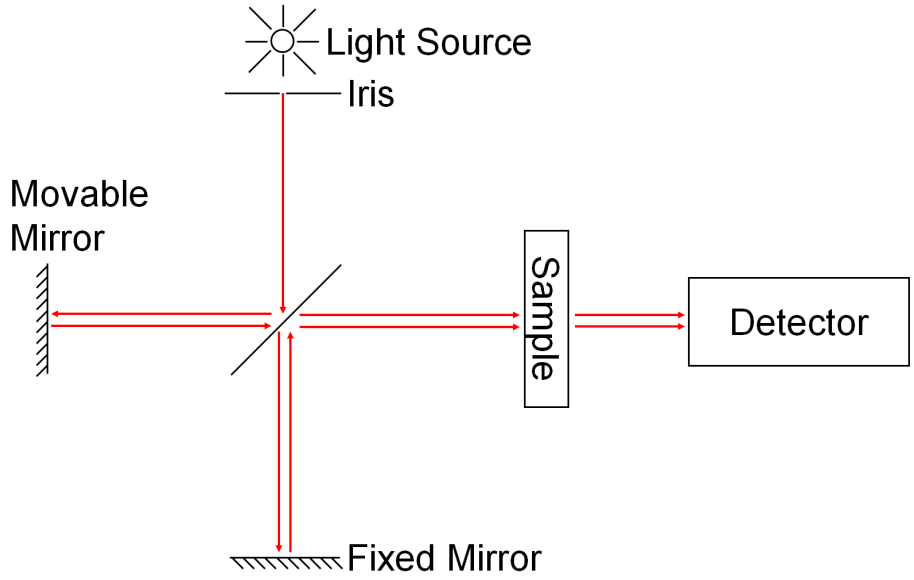

Figure 2.1: Optical design of Michelson Interferometer.

2.1.1.2 PerkinElmer Grating Spectrometer

A PerkinElmer Lambda 950 Grating Spectrometer is used in the $0.19\mu m$ to $0.8\mu m$ ($52,500cm^{-1}$ to $12,500cm^{-1}$) spectral region. All PerkinElmer transmittance data have been collected with a resolution of 0.25nm ($2.5cm^{-1}$ at $10,000cm^{-1}$). The Perkin Elmer spectrometer is configured with multiple sources, a tungsten-halogen lamp for $0.319\mu m$ to $0.8\mu m$ and a deuterium lamp for $0.19\mu m$ to $0.319\mu m$. A holographic grating with 1440 lines/mm and photomultiplier tube with multialkali cathode are used for the $0.19\mu m$ to $0.8\mu m$ spectral region. Measurements in the $52,500cm^{-1}$ to $12,500cm^{-1}$ spectral range are performed under nitrogen purge.

2.1.1.3 Calibration of Transmittance

Baselines are collected for detectors in all spectral regions and ratioed out of the data. Detector baselines are expected to be flat and at unity near peak responsivity of the detector. As the baseline approaches the edge of usable detector response, the baseline will depart from zero and display increased noise. An example baseline is shown in Fig 2.2.

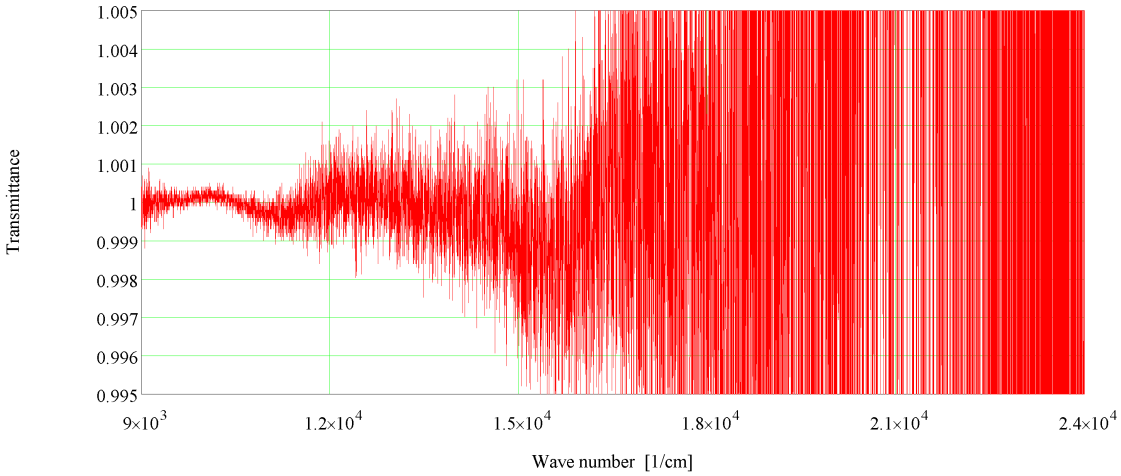

Figure 2.2: Example baseline for silicon detector from BOMEM DA3.02 Fourier Transform Spectrometer in the $24,000cm^{-1}$ to $9000cm^{-1}$ spectral region.

Detectors in adjacent spectral bands are aligned using common features from overlapping detector data. Transmittance data are further calibrated using transmittance measurements from coherently detected, stabilized laser sources at $0.405\mu m$, $0.633\mu m$ and $1.064\mu m$. We estimate the precision of our laser transmittance measurements to be $\Delta\tau \approx 0.001$. All measurements on the spectral width of absorption features were carried out on the BOMEM DA3.02 Fourier Transform Spectrometer with a resolu-

tion of $2cm^{-1}$. A subset of measurements were repeated at $0.5cm^{-1}$ with no change to the spectral features of interest, therefore we believe that $2cm^{-1}$ is a sufficient resolution.

2.1.2 Temperature Dependent Transmittance Experimental Setup

Samples characterized in the temperature dependent transmittance work include Nd doped polycrystalline YAG, with doping percentages of 1% and 6%. Data was collected in the $25,000cm^{-1}$ to $8,500cm^{-1}$, $0.5\mu m$ to $1.18\mu m$, spectral range with a resolution of $2cm^{-1}$. A calibrated quartz-halogen lamp source and Silicon photodetector are used. All measurements were performed under medium vacuum of less than 0.5 torr to limit convective heat transfer and remove parasitic gas absorption features.

Data was calibrated by collecting baseline data measurement using an empty BOMEM sample chamber and dividing this baseline out of all data files. The sample temperature was controlled by incorporating a hot cell into the sample chamber. The hot cell permitted cooling and heating of the samples under test in the temperature range of $278K$ to $473K$. Transmittance data baseline was confirmed by performing room temperature transmittance measurements in the apparatus shown in Ref.[19] and using laser sources at $1.064\mu m$ and $0.633\mu m$. The absolute accuracy of BOMEM

transmittance measurement is a function of the time between baseline measurement and sample data collection. The $278K$ transmittance data has best absolute accuracy estimated at $\Delta\tau \approx 0.001$ and the $473K$ transmittance data has lowest absolute accuracy estimated at $\Delta\tau \approx 0.002$.

2.2 Scatterance

Scatterance data also provides important information on a potential laser gain media loss mechanism. Determining the type of scatter can help identify the source and possible methods to mitigate scatter losses.

2.2.1 Scatterometer

The scatterometer experimental setup is detailed in Fig. 2.3. This setup directly measures both in-plane and out-of-plane angular dependant scatter in both the transmitted and reflected hemispheres. The system is equipped with multiple laser sources including those at $0.405\mu m$, $0.532\mu m$, $0.633\mu m$, $1.064\mu m$ and $1.55\mu m$. The source is mechanically chopped to allow for coherent detection and the lasers are monitored for power fluctuations and drift using an auxiliary detector. The chopped laser source is fed into an optical system to permit beam expansion and focusing through the the sample under test. The laser source is horizontally polarized when incident upon the sample. Multiple signal detectors are available depending on desired wavelength,

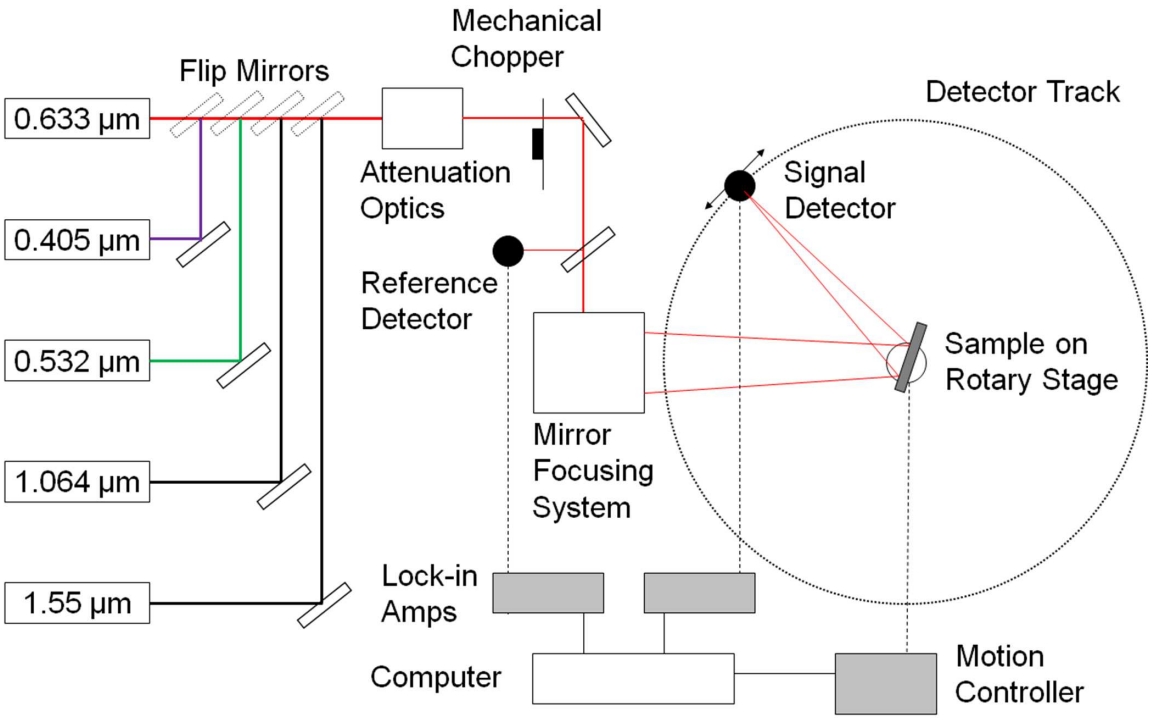

Figure 2.3: Experimental Setup for BSDF Measurements.

angular resolution, and sensitivity. Measurements in this study were collected using either a silicon or germanium signal detector mounted on a rotary stage revolving horizontally in the plane of incidence. Multiple sample source incident angles are collected with the aid of a sample rotary stage rotating in the horizontal plane of incidence. Data is typically collected at a 5 degree incident angle. Collecting data at oblique angles will allow better distinction between bulk and surface reflection terms, however this requires samples larger than available in this study. The signal and auxiliary detector signals are coherently measured using lock-in-amplifiers to suppress background noise and allow for expanded dynamic range.

2.3 Fluorescence

Fluorescence data can provide data on laser gain media line width and upper level lifetimes. Information on branching ratios can be derived from fluorescence data.

2.3.1 Room Temperature Fluorescence

Nd doped polycrystalline YAG, with a doping percentage of 1%, was characterized using fluorescence measurements. The sample was polished to 10/5 scratch dig and coated with an anti-reflective coating designed for the $0.9\mu m$ to 1.1μ range. The sample was water-cooled to $293K$.

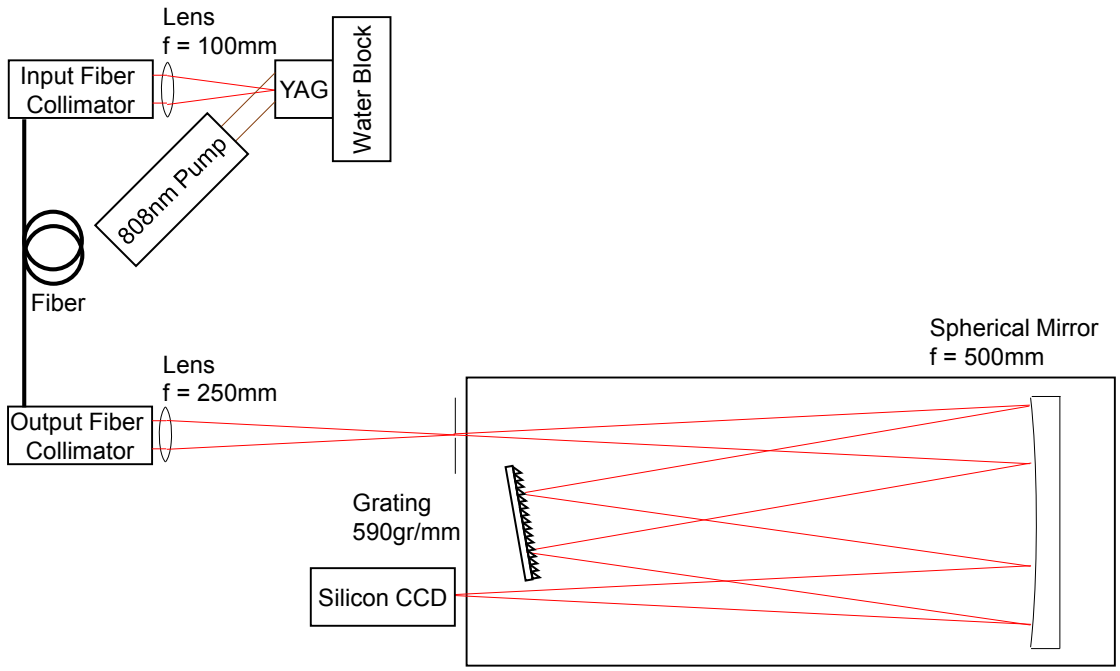

Figure 2.4: Samples under test include undoped and 1% to 6% Nd doped polycrystalline YAG and undoped and 1% Nd doped single crystal YAG.

The fluorescence optical measurement system is shown in Fig. 2.4. The sample was pumped with laser diodes emitting at $0.808\mu m$ and bandwidth of $0.3nm$. Fluorescence was coupled into a fiber protected with a $0.808\mu m$ band stop filter. Light from the fiber was coupled into a Jarrell Ash Model 82, $0.5meter$ Fastie-Ebert monochromater with a grating grooved at $590lines/mm$ and entrance slit of $10\mu m$. The output of the monochromater was imaged onto a silicon CCD, with a pixel size of $4.4\mu m$ and array size of $1600x1200$.

Wavelength calibration of the optical setup was performed using emission from fiber coupled Argon and Krypton atomic lamp sources. Intensity calibration of the optical system (fiber collimators, notch filter, fiber, monochromater and CCD) was performed by coupling the output of a high temperature cavity black body emitting at $1050K$ into the fiber collimator. System resolution was measured at $0.58cm^{-1}FWHM$ $[0.054nm]$ at $10,354.34cm^{-1}$ $[0.9657786\mu m]$, limited by the entrance slit width.[39]

Chapter 3

Models

3.1 Transmittance

3.1.1 Extinction Coefficient

The extinction coefficient is calculated from the calibrated transmittance using Eq. 3.1, where d is the material thickness, $R(\lambda)$ is the wavelength dependant Fresnel power reflection, and τ is the transmittance[5,6] Based on the transmittance from Section 2.1.1, the absolute accuracy of the room temperature extinction coefficient is estimated to be $\Delta\beta_{ext} \approx 0.0035$.

$$\beta_{ext} = \frac{1}{d} ln \left[\frac{2R^2\tau}{\sqrt{(1-R)^4 + 4R^2\tau^2} - (1-R)^2} \right] \tag{3.1}$$

3.1.2 Modified Lorentzian Line Shape

A model for the Nd:YAG diode pump band absorption coefficient is required for precise laser pump design. All measured absorption features were found to be a modified Lorentzian line shape, Eq. 3.12, where v is the absorption transition in wavenumbers, v_0 lower energy level line center frequency $[cm^{-1}]$, and γ_0 is the feature width $[cm^{-1}HWHM]$.

$$\jmath(v) = \frac{1}{\pi} \cdot \frac{v}{v_0} \cdot \frac{\gamma_0}{(v - v_0)^2 + (\gamma_0)^2} \tag{3.2}$$

3.1.3 Classical Oscillator Model

The classical oscillator model is presented in Eq. 3.3; where the summation is over the different electronic bands, pump and lasing, ν is in wave numbers $[cm^{-1}]$, ν_0 is in oscillator location in wave numbers $[cm^{-1}]$, n is the index of refraction, c is the speed of light $[cm/s]$, $\Delta\varepsilon$ is the oscillator strength, and Γ is the oscillator width $[cm^{-1}FWHM]$.[36] Please note this model is not valid in the wings of the spectral line.

$$\beta_{abs}(v) = \frac{v^2}{nc} \sum_i \frac{v_{0i}^2 \Delta\epsilon_i \Gamma_i}{\left(v_{0i}^2 - v^2\right)^2 + \left(v\Gamma_i\right)^2} \tag{3.3}$$

3.1.4 Temperature Dependant Line Width

McCumber theory provides the theoretical basis for line width in solid state materials. The line width of transition in YAG has two components, the temperature independent line width due to inhomogeneous crystal field strain and temperature dependent line width due to Brillouin scattering processes as determined by the characteristic Debye temperature.[20] Kushida used McCumber theory to produce a model that provides an accurate fit for solid state material line width discrete measurements, Eq. 3.4, where Γ_i is the FWHM line width of the ith line, T is the material temperature in Kelvin, $\Gamma_i(0)$ is the intrinsic line width of the ith line, α_i is the strength term for temperature dependent line width of the ith line, and Θ_D is the Debye temperature. The Debye temperature for YAG is $\Theta_D = 500K$[40].[9]

$$\Gamma_i(T) = \Gamma_i(0) + \alpha_i \left(\frac{T}{\Theta_D}\right)^7 \xi_6\left(T\right) \tag{3.4}$$

and

$$\xi_6(T) = \int_0^{\frac{\Theta_D}{T}} \frac{x^6 e^x}{\left(e^x - 1\right)^2} dx \tag{3.5}$$

3.1.5 Extinction Cross Section Model

Operation of a Nd:YAG laser on the quasi three level ${}^4F_{3/2} \rightarrow {}^4I_{9/2}$ transition produces emission at $0.946\mu m$, with the lower laser lever terminating at $852cm^{-1}$ above the ground state. This proximity to the ground state leads to significant room

temperature thermal population in the lower laser level resulting in absorption. The ${}^4F_{3/2} \rightarrow {}^4I_{9/2}$ transition is of lower gain than the ${}^4F_{3/2} \rightarrow {}^4I_{11/2}$ transition used for $1.064\mu m$ emission. If efficient emission at $0.946\mu m$ is desired, the resonator must be carefully designed to suppress amplified spontaneous emission (ASE) at $1.064\mu m$ and the gain media cooled to minimize lower lasing level thermal population.[18,41]

Thermal population of the lower laser level ${}^4I_{9/2}$ is given by a Maxwell-Boltzmann distribution, described by Eq. 3.6. N_l is the lower laser level population, g_l is the degeneracy of the lower laser level, N_0 is the total dopant population, $Q(T)$ is the partition function, E_l is the energy of the lower laser level, k_B is Boltzmann's constant, and T is the temperature.[41]

$$N_l(T) = \frac{g_l N_0}{Q(T)} exp\left(\frac{-E_l}{k_B T}\right), where\ E_l = hcv_l \tag{3.6}$$

The partition function is shown in Eq. 3.7, where g_i is the degeneracy of the ith stark sublevel in the ${}^4I_{9/2}$ and ${}^4I_{11/2}$ manifolds, and E_i is the energy of ith stark sublevel of the ${}^4I_{9/2}$ and ${}^4I_{11/2}$ manifolds. In Nd:YAG, all relevant energy manifolds split into $(2J+1)/2$ doubly degenerate energy levels, therefore all degeneracies are $g = 2$ and cancel out in all equations involving ratios of degeneracies.[14] The partition function is presented in Eq. 3.7.

$$Q(T) = \sum_i g_i exp\left(\frac{-E_i}{k_B T}\right) \tag{3.7}$$

The temperature and wavelength dependant absorption coefficient $\beta_{abs}(v,T)$ is derived by multiplying the temperature and wavelength dependent absorption cross section $\sigma_{abs}(v,T)$ by the difference of the lower level population $N_l(T)$ and the upper level population $N_u(T)$, Eq. 3.8[18]

$$\beta_{abs}(v,T) = \sigma_{abs}(v,T) \cdot [N_l(T) - N_u(T)] \tag{3.8}$$

The wavelength and temperature dependent absorption cross section is a product of the integrated temperature dependent absorption cross section $\sigma^I_{abs}(T)$ and the line shape function $\jmath(v,T)$, Eq 3.9. Substituting Eq. 3.8 results in Eq. 3.10.

$$\sigma_{abs}(v,T) = \sigma^I_{abs}(T) \cdot \jmath(v,T) \tag{3.9}$$

$$\beta_{abs}(v,T) = \sigma^I_{abs} \cdot \jmath(v,T) \cdot [N_l(T) - N_u(T)] \tag{3.10}$$

The absorption feature line strength at 946 nm also follows the Maxwell-Boltzmann distribution, given by Eq. 3.6. The absorption features around 946 nm were found to be a modified Lorentzian line shape, given by Eq. 3.12; v is the absorption transition, v_0 is the lower absorption energy level, and γ_0 is the line width. The line width was found to be temperature dependant. The near line center (nlc) line shape function integrates to one, Eq. 3.13. $S(T)$ is the line strength or integrated temperature dependent absorption coefficient, Eq. 3.14.

$$\beta_{abs}(v,T) = \sigma^I_{abs} \cdot \jmath(v,T) \cdot \frac{N_0 g_l}{Q(T)} exp\left(\frac{-E_l}{k_B T}\right), E_l = hcv_l \tag{3.11}$$

$$\jmath(v) = \frac{1}{\pi} \cdot \frac{v}{v_0} \cdot \frac{\gamma_0}{(v-v_0)^2 \cdot (\gamma_0)^2} \tag{3.12}$$

$$\int_{nlc} \jmath(v)dv = 1 \tag{3.13}$$

$$S(T) = \int \beta_{abs}(v,T)dv \tag{3.14}$$

Integrating Eq. 3.10 over wavelength results in the temperature dependant line strength, Eq. 3.15. The upper level population can be neglected because it is small; giving the absorption cross section, Eq. 3.16.

$$\beta^I_{abs}(T) = \sigma^I_{abs} \cdot [N_l(T) - N_u(T)] \tag{3.15}$$

$$\sigma^I_{abs} = \frac{\beta^I_{abs}(T)}{N_l(T)}; N_u(T) \approx 0 \tag{3.16}$$

The integrated absorption coefficient, also called line strength, is converted to a peak absorption coefficient $\beta_{abs}(T)$, Eq 3.17. The integrated absorption cross section can be converted to the peak absorption cross section $\sigma_{abs}(T)$, Eq 3.18.

$$\beta_{abs}(v_0,T) = \frac{\beta^I_{abs}(T)}{\pi \cdot \gamma_0(T)} \tag{3.17}$$

$$\sigma_{abs}(v_0,T) = \frac{\sigma^I_{abs}}{\pi \cdot \gamma_0(T)} \tag{3.18}$$

The extinction coefficient $\beta_{ext}(T)$ is the sum of the absorption coefficient and scatter coefficient β_{sca}, Eq. 3.19. The scatter coefficient is assumed to be temperature independent over the temperature range of interest.

$$\beta_{ext}(T) = \beta_{abs}(T) + \beta_{sca} \tag{3.19}$$

A $0.946\mu m$ Nd:YAG laser operates on the ${}^4F_{3/2} \rightarrow {}^4I_{9/2}$ transition. Due to stark splitting there are two levels in the ${}^4I_{9/2}$ manifold, located at $11507cm^{-1}$ and $11423cm^{-1}$. To lase at $0.946\mu m$, you must operate on the $11423cm^{-1}$ to $852cm^{-1}$, transition.[16]

Since the degeneracies of the upper and lower levels are equal, the peak stimulated emission cross section is equal to the peak absorption cross section, Eq. 3.20.

$$\sigma_{em}(T) = \sigma_{abs}(T) \tag{3.20}$$

3.2 Scatter

3.2.1 Bidirectional Scatter Distribution Model

The scatterance of all polycrystalline and single crystal samples was measured directly. All measurements were conducted in the horizontal plane with vertical and out of plane scatterance assumed to be well behaved random features with no

grating effects. All raw data were fit to a model to remove artifacts inherent to the measurement apparatus. Observed artifacts include detector apparatus blocking laser source in the near specular direction and diffraction effects due to sample edges and holder. A modified version of the specular scatterance model from Ref.[42,43] was used to account for the convolution of detector and laser beam profile. Details on the scatterance model for near specular, diffuse, and Lambertian can be found in Ref.[42,43]

3.2.1.1 Specular Phase Function

The specular phase function is represented by the component P_{in}. In the interest of increased scatterance signal, a $8mm$ diameter detector was selected to sample an approximately $4mm$ diameter Gaussian incident laser source. To compensate for the loss of specular phase function precision, the data was oversampled in the specular region to allow a more accurate model fit. The specular phase function is a convolution of the Gaussian profile of the laser source and the cylindrical function response of a finite detector, shown in Eq. 3.21, where θ_r is the reflection angle, θ_i is the incidence angle, N_{in} is a normalization coefficient,[42] w is proportional to the angular extent of the detector diameter, and c is proportional to the angular extent of the laser diameter. A representative phase function and fit is shown in Fig. 3.1,

$$P_{in}(\theta_r, \theta_i) = N_{in}(\theta_i, w)\left[erf\left(\frac{\frac{(\sin\theta_r+\sin\theta_i)}{\cos\theta_i}+\frac{w}{2}}{c}\right)+erf\left(\frac{\frac{-(\sin\theta_r+\sin\theta_i)}{\cos\theta_i}+\frac{w}{2}}{c}\right)\right] \quad (3.21)$$

where

$$N_{in}(\theta_i, w, c) = \frac{1}{\pi\left(\frac{1}{2}w^2 + c^2\right)}. \tag{3.22}$$

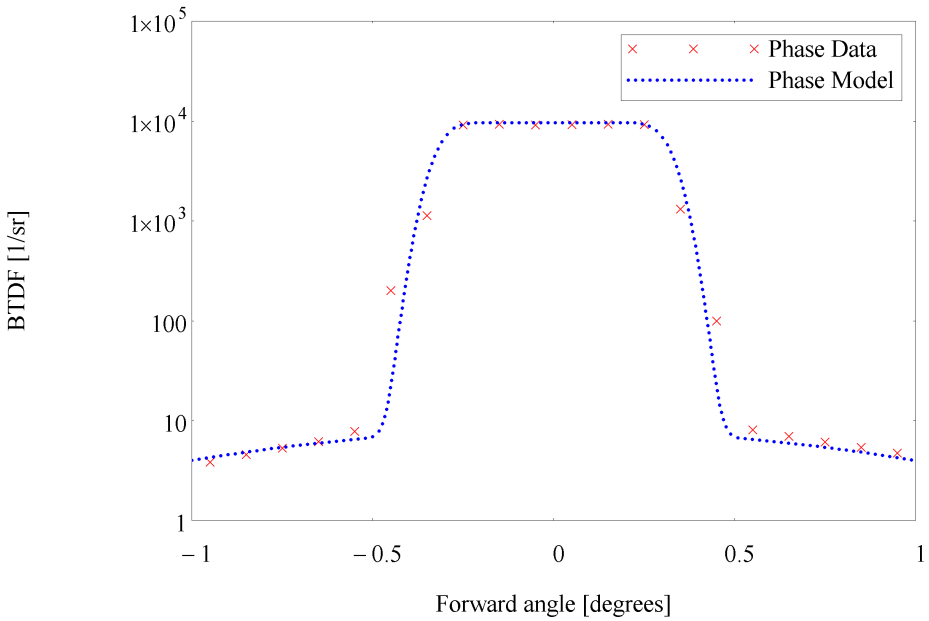

Figure 3.1: Phase function for Undoped Polycrystalline YAG from 1.064 um Nd:YAG laser.

3.2.1.2 Near Specular Phase Function

The near-specular component P_{ns} is derived from the Van Cittert-Zernike theorem, Eq. 3.23[44].[45] The terms, N_{ns} is a normalization coefficient, r_0 is the correlation length, and σ_h is the surface roughness. Further details on the derivation are contained in Ref.[42,43]

$$P_{ns}(\theta_r, \theta_i) = N_{ns}(\theta_i, C)\mathrm{e}^{-\frac{(\sin\theta_r + \sin\theta_i)^2}{(C\cos\theta_i)^2}}\cos\theta_r \tag{3.23}$$

where

$$C \approx r_0/4\sigma_h \tag{3.24}$$

and

$$N_{ns}(\theta_i, C) = \pi \left[\cos(\theta_i) I1_{ns}(\theta_i, C) + \sin(\theta_i) I2_{ns}(\theta_i, C)\right] \tag{3.25}$$

and

$$\begin{aligned} I1_{ns}(\theta_i, C) =& \frac{C^2}{2}\left[2 - \mathrm{e}^{\frac{-\left(\sin(\theta_i)-1\right)^2}{C^2}} - \mathrm{e}^{-\left(\frac{1+\sin(\theta_i)}{C}\right)^2}\right] - \\ & C\frac{\sqrt{\pi}}{2}\sin(\theta_i)\left[erf\left(\frac{1+\sin(\theta_i)}{C}\right) + erf\left(\frac{\sin(\theta_i)-1}{C}\right)\right] \end{aligned} \tag{3.26}$$

and

$$\begin{aligned} I2_{ns}(\theta_i, C) =& \int_{-\sin(\theta_i)}^{1} \sqrt{1-w^2}\mathrm{e}^{-\left(\frac{w+\sin(\theta_i)}{C}\right)^2} dw - \\ & \int_{\sin(\theta_i)}^{1} \sqrt{1-w^2}\mathrm{e}^{-\left(\frac{\sin(\theta_i)-w}{C}\right)^2} dw \end{aligned} \tag{3.27}$$

In practice, C is empirically chosen based on the reflectance measurement.

3.2.1.3 Diffuse Phase Function

The diffuse component P_d is defined by Eq. 3.28. In this equation, m is a phase function coefficient chosen by a data fit (e.g. m = 2 for Lorentz type), α is the

reflected beam half angle, and N_d is a normalization coefficient.[42,43]

$$P_d(\theta_r, \theta_i, m, \alpha) = N_d(\theta_i, \alpha) \frac{(\alpha \cos\theta_i)^{m-1}}{(|\sin\theta_r + \sin\theta_i|)^m + (\alpha\cos\theta_i)^m} \cos\theta_r \tag{3.28}$$

where

$$N_d(\theta_i, \alpha) = \pi\alpha \left[\cos(\theta_i) A_2(\theta_i, \alpha) + \sin(\theta_i) B_2(\theta_i, \alpha)\right] \tag{3.29}$$

and

$$\begin{aligned} A_2(\theta_i, \alpha) =& \frac{1}{2}\left[ln\left(1 + \left(\frac{1+\sin(\theta_i)}{\alpha}\right)^2\right)\right] - \frac{\sin(\theta_i)}{\alpha} arctan\left(\frac{1+\sin(\theta_i)}{\alpha}\right) + \\ & \frac{1}{2}\left[ln\left(1 + \left(\frac{\sin(\theta_i)-1}{\alpha}\right)^2\right)\right] - \frac{\sin(\theta_i)}{\alpha} arctan\left(\frac{\sin(\theta_i)-1}{\alpha}\right) \end{aligned} \tag{3.30}$$

and

$$B_2(\theta_i, \alpha) = \int_0^{1+\sin(\theta_i)} \frac{\sqrt{1-(t-\sin(\theta_i))^2}}{t^2+\alpha^2} dt + \int_0^{\sin(\theta_i)-1} \frac{\sqrt{1-(t-\sin(\theta_i))^2}}{t^2+\alpha^2} dt \tag{3.31}$$

3.2.1.4 Lambertian Phase Function

The Lambertian component P_l is defined as follows:[42]

$$P_l(\theta_r) = \frac{1}{\pi}\cos(\theta_r). \tag{3.32}$$

3.2.1.5 Probability Distribution Functions

Strictly speaking the above phase functions are probabilities which fit the data but do not satisfy reciprocity. Using these functions the angular dependant scatter model can be completely characterized over all angles, resulting in the bidirectional scatterance probability distribution function (BSPDF). The BSPDF is often separated into the rear hemisphere, bidirectional reflectance probability distribution function (BRPDF) shown in Eq. 3.33 and forward hemisphere, bidirectional transmitted probability distribution function (BTPDF) shown in Eq. 3.34.[42] Each BRPDF component is proceeded by a ρ strength term, each BTPDF component is proceeded by a τ strength term. The in, ns, d, and l subscripts refer to the specular, near-specular, diffuse, and Lambertian components of scatter, respectively.

$$BRPDF(\theta_r, \theta_i) = \rho_{in} P_{in}(\theta_r, \theta_i) + \rho_{ns} P_{ns}(\theta_r, \theta_i) + \rho_d P_d(\theta_r, \theta_i, m, \alpha) + \rho_l P_l(\theta_r) \quad (3.33)$$

$$BTPDF(\theta_t, \theta_i) = \tau_{in} P_{in}(\theta_t, \theta_i) + \tau_{ns} P_{ns}(\theta_t, \theta_i) + \tau_d P_d(\theta_t, \theta_i, m, \alpha) + \tau_l P_l(\theta_t) \quad (3.34)$$

Scatterance can be roughly segregated into two categories: surface roughness and bulk material defects. Surface roughness will contribute most of the near specular scatter component and will not scale with path length. The near specular component can be reduced by improved surface polishing. Bulk material defects will contribute most of the diffuse and Lambertian components and can be reduced by advances in material production technique. We have defined the total integrated scatter diffuse(TIS_D) as

the forward plus reverse integrated diffuse and Lambertian scatter components. For small scatter loss, dividing the TIS_D by path length results in the scatter coefficient (β_{sca}).

The total power law is shown in Eq. 3.35, where ρ is the total integrated reflectance, α_{abs} is the absorptance for the path length of the media, and τ is the total integrated transmittance. The sum of these coefficients must equal one, satisfying the total power law.[46]

$$\rho + \alpha_{sca} + \alpha_{abs} + \tau = 1 \tag{3.35}$$

where

$$\alpha_{sca} = \tau_l + \rho_l + \tau_d + \rho_d + \tau_{ns} + \rho_{ns} \tag{3.36}$$

and

$$TIS_D = \tau_l + \rho_l + \tau_d + \rho_d \tag{3.37}$$

3.2.2 Diffuse Scatter Model

3.2.2.1 Anomalous Diffraction Approximation

The goal of the multi-wavelength scatter study was to develop a scatter model to cover the entire visible to NIR region. The SEM measurements from Table 4.7 indicate the grain size is on the order of the wavelength in the range of interest, and therefore within the Mie scatter regime. To extend the discrete TIS measurements

presented in Table 4.6, a visible to NIR model fit to test data was developed. For the polycrystalline material, we hypothesize the scatter is dominated by an index mismatch between YAG and a sintering agent, and index variations due to grain to grain dopant percentage inconsistency. For single crystal material scatter is dominated by lattice strain due to the crystal growth technique. Porosity was also considered for both material types but not found to be important.

3.2.2.1.1 Spherical ADA

For index mismatch and grain to grain index variation, the feature sizes are of the order of the wavelengths of interest. This is within the Mie regime and an Anomalous Diffraction Approximation (ADA) was used. The ADA equation, shown in Eq. 3.38, was developed by H. C. Van De Hulst as a closed form, computationally efficient approximation to Mie Theory where Q_{ext} is the extinction efficiency and ρ is the phase lag of the wave passing through the scatterer.[47]

$$Q_{ext} = 2 - \frac{4}{\rho} sin(\rho) + \frac{4}{\rho^2} (1 - cos(\rho)) \tag{3.38}$$

Van De Hulst's original equation for a spherical particle geometry, Eq. 3.39, here ρ is the phase lag of the wave passing through the scatterer, ka is the size parameter, m is the modified index of refraction, and n_{back} is the index of refraction for the background medium,

$$\rho = 2ka\,(m - 1) \tag{3.39}$$

where

$$k = \frac{2\pi}{\lambda} n_{back}. \tag{3.40}$$

The above ADA equations hold for values of $|m-1| \ll 1$ and $x = 2\pi a/\lambda$.

3.2.2.1.2 Coated Sphere ADA

For scatter due to index mismatch between YAG and residual sintering agents, a more complicated model is required. Residual porosity in polycrystalline materials is a major potential contributor to scatter and is the result of less than full theoretical density for the material. A sintering or flow agent is used improve the densification rate and final densification. Details on the effects of silica sintering aid can be found in Ref.[48–50] After casting and vacuum sintering of the material, some residual sintering agent remains in the polycrystalline material.[35] An index mismatch between the residual sintering agent and YAG grains can lead to material scatter. This material is collected as a thin film at the grain boundary with the geometry approximated by a coated sphere, as shown in Fig. 3.2. For this case Van De Hulst's ADA original equation must be modified for the coated sphere geometry. The coated sphere problem is setup in reference,[51] from which an approximate solution can be derived. For the special case where the index inside and outside the spherical coating are equal, an exact solution was derived by Dr. Richard Joseph.[19]

Eq. 3.41 is the phase delay through material a ρ_a and Eq. 3.42 is the phase delay through both material a and b ρ_{ab}, where m_a and m_b are the relative indices of

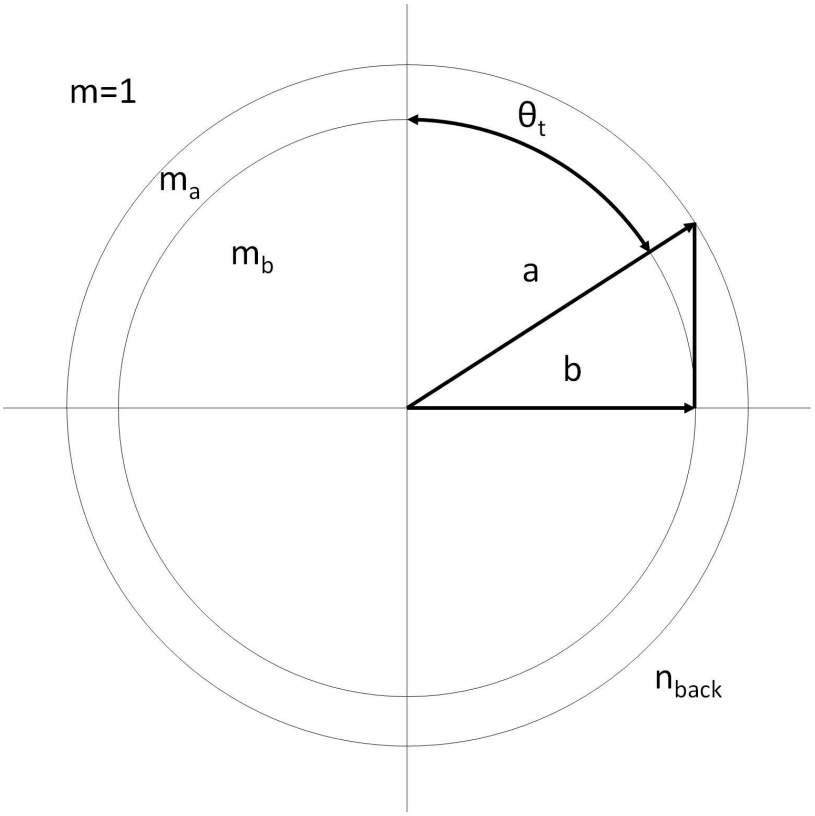

Figure 3.2: Geometry for the coated sphere ADA model.

material a and b respectively. For this case, the relative index of the sphere interior m_b and outside the spherical coating are the same YAG material. Here

$$\rho_a = 2ka(m_a - 1) \tag{3.41}$$

and

$$\rho_{ab} = 2ka(m_b - m_a). \tag{3.42}$$

Eq. 3.43 is the transition angle θ_t

$$sin(\theta_t) = b/a \tag{3.43}$$

The extinction cross section σ_{ext} is derived from the optical theorem, Eq. 3.44

$$\sigma_{ext} = 2 \int_P [1 - cos(\psi)]\, dP = 4\pi a^2 J \tag{3.44}$$

where

$$\psi = \begin{cases} \rho_a cos(\theta) & \theta_t \leq \theta \leq \pi/2 \\ \rho_a cos(\theta) + \rho_{ab} \sqrt{cos^2(\theta) - cos^2(\theta_t)} & 0 \leq \theta \leq \theta_t \end{cases} \tag{3.45}$$

J is divided into two parts where J_1 and J_2 correspond to $\theta \geq \theta_t$ and $\theta \leq \theta_t$, respectively,

$$J = J_1 + J_2 \tag{3.46}$$

The evaluation of J_1 is straight forward and results in Eq. 3.47.

$$J_1 = cos^2(\theta_t) \left[\frac{1}{2} - \frac{1}{A^2} \left(Asin(A) + cos(A) - 1 \right) \right] \tag{3.47}$$

where

$$A = \rho_a cos(\theta_t) \tag{3.48}$$

In general J_2 must be evaluated numerically. However for the special case [$m_b = 1, \rho_{ab} = -\rho_a$], J_2 may be solved exactly.

$$\begin{aligned} J_2 =& \int_0^{\theta_t} d\theta sin(\theta)cos(\theta) \\ & \left[1 - cos\left\langle \rho_a \left(cos(\theta) - \sqrt{cos^2(\theta) - cos^2(\theta_t)}\right) \right\rangle\right] \\ \equiv& \frac{1}{2}sin^2(\theta_t) - \hat{J}_2 \end{aligned} \tag{3.49}$$

To evaluate $\hat{J}_2$ let $cos(\theta) = xcos(\theta_t)$ then

$$\hat{J}_2 = cos^2(\theta_t) \int_1^{1/cos(\theta_t)} dx\ x\ cos\left[A\left(x - \sqrt{x^2 - 1}\right)\right] \tag{3.50}$$

where A is given in Eq. 3.48.

After a transformation of variables, $W = x - \sqrt{x^2 - 1}$ and $AW = t$,

$$\begin{aligned} \hat{J}_2 =& \frac{1}{4}cos^2(\theta_t) \int_A^{AW_t} dt\ cos(t) \left[\frac{t}{A^2} - \frac{A^2}{t^3}\right] \\ \equiv& \frac{1}{4}cos^2(\theta_t) \left[\frac{P}{A^2} - A^2 Q\right] \end{aligned} \tag{3.51}$$

where

$$W_t = \frac{1 - sin(\theta_t)}{cos(\theta_t)} \tag{3.52}$$

The evaluation of P is given in Eq. 3.53,

$$P = cos(AW_t) - cos(A) + AW_t sin(AW_t) - Asin(A) \tag{3.53}$$

and

$$\begin{aligned} Q &= \int_A^{AW_t} \frac{\mathrm{d}t}{t^3} cos(t) \\ &\equiv -\frac{1}{2}\left[\left(\frac{cos(AW_t)}{A^2W_t^2} - \frac{cos(A)}{A^2}\right) - \left(\frac{sin(AW_t)}{AW_t} - \frac{sin(A)}{A}\right) + Ci(AW_t) - Ci(A)\right] \end{aligned} \tag{3.54}$$

where Ci denotes the the cosine-integral. A similar result holds if $m_a = 1/2\,(m_b + 1)$ with $W_t = (1 + sin(\theta_t))\,/\,(cos(\theta_t))$.

Combining Eqs. 3.44, 3.46, 3.47, 3.48, 3.49, 3.51, 3.52, and 3.54 gives σ_{ext}.

3.2.2.2 Kubelka-Munk Theory

Assume a diffuse wave is incident upon a window, thin in the direction of propagation and infinite in the transverse direction. Flux incident upon the surface must either be absorbed or scattered out the incident or rear surface of the window. Two first order coupled Helmholtz equations are derived from the proceeding explanation. The Kubelka Munk theory is an exact solution to these Helmholtz equations. The Kubelka Munk equations for random diffuse light propagation is defined in Eq. 3.55 and 3.56, where ρ_L is the random diffuse reflectance, τ_L is the random diffuse

transmittance, a_L is the Lambertian albedo, β_{sca} is the single scatter coefficient, d is propagation length, and ρ_{Lsub} is the Lambertian total integrated reflection of a substrate. If the material has no substrate, then $\rho_{Lsub} = 0$.[52]

$$\rho_L(a_L, \beta_{sca}, d) = \frac{b_- - b_+ \frac{b_- - \rho_{Lsub}}{b_+ - \rho_{Lsub}} \mathrm{e}^{-2\sqrt{\frac{1}{a_L^2}-1}\beta_{sca}d}}{1 - \frac{b_- - \rho_{Lsub}}{b_+ - \rho_{Lsub}} \mathrm{e}^{-2\sqrt{\frac{1}{a_L^2}-1}\beta_{sca}d}} \tag{3.55}$$

and

$$\tau_L(a_L, \beta_{sca}, d) = \frac{1 - \frac{b_- - \rho_{Lsub}}{b_+ - \rho_{Lsub}} \mathrm{e}^{-\sqrt{\frac{1}{a_L^2}-1}\beta_{sca}d}}{1 - \frac{b_- - \rho_{Lsub}}{b_+ - \rho_{Lsub}} \mathrm{e}^{-2\sqrt{\frac{1}{a_L^2}-1}\beta_{sca}d}} \tag{3.56}$$

where

$$b\pm = \frac{1}{a_L} \pm \sqrt{\frac{1}{a_L^2} - 1} \tag{3.57}$$

The Lambertian albedo a_L is defined in Eq. 3.58, where β_{sca} is the single scatter coefficient and β_{abs} is the absorption coefficient.[52,53]

$$a_L = \frac{0.5\beta_{sca}}{\beta_{abs} + 0.5\beta_{sca}} \tag{3.58}$$

The extinction coefficient may be derived from the extinction efficiency using Eq. 3.59, where β_{ext} is the extinction coefficient, Q_{ext} is the extinction efficiency, p is the projected area of particle and ρ is number density of scatterers.[36]

$$\beta_{ext} = Q_{ext} p \rho \tag{3.59}$$

Chapter 4

Results and Discussion

4.1 Transmittance

4.1.1 Room Temperature Transmittance

4.1.1.1 Calibrated Transmittance Data

Figure 4.1 is the calibrated transmittance of available doping percentages of polycrystalline Nd:YAG for the region of transparency. Please note thinner 0.75 mm samples doped polycrystalline samples were used for the $11,020cm^{-1}$ to $12,500cm^{-1}$ region to prevent saturation of absorption features. All samples are uncoated. Sellmeier's Equation and YAG Sellmeier parameters were used to derive the wavelength dependant index of refraction.[36] Wavelength dependant Fresnel power reflection losses are calculated from the index of refraction and plotted as theoretical lossless trans-

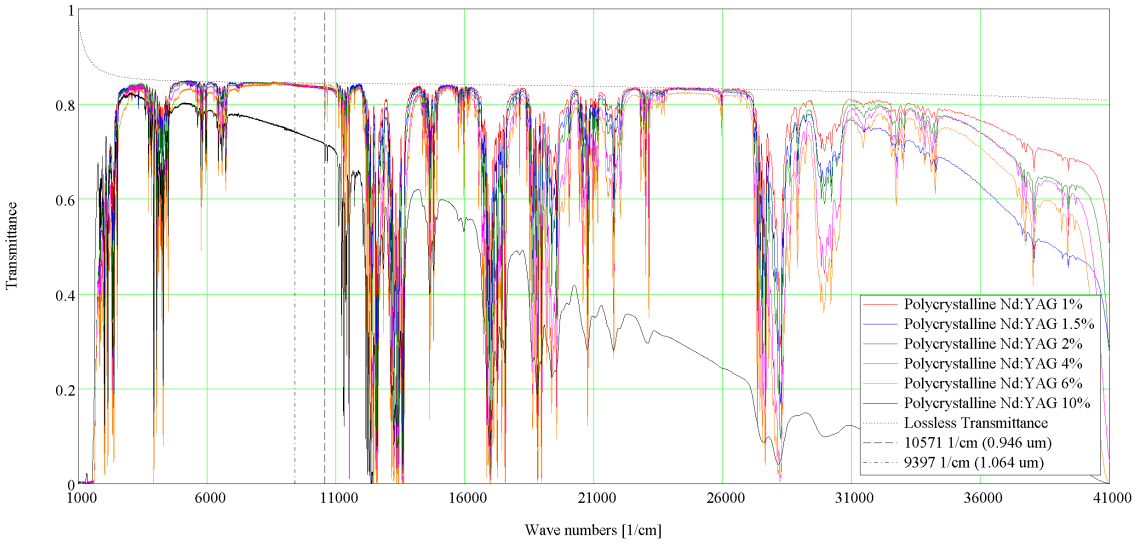

Figure 4.1: Konoshima polycrystalline Nd doped YAG transmittance compared to theoretical lossless transmittance measured at room temperature. The $9397cm^{-1}$ ($1.064\mu m$) and $10,571cm^{-1}$ ($0.946\mu m$) transition are highlighted. ©2013 IEEE.

mittance. As mentioned in Section 2.1.1, the absolute accuracy of room temperature transmittance measurements is estimated to be $\Delta\tau \approx 0.001$. The material under test is very close to the theoretical lossless transmittance regions of interest near $1.064\mu m$ ($9397cm^{-1}$), and $0.532\mu m$ ($18,794cm^{-1}$). Figures for each doping percentage, depicting detector spectral ranges, are included in the Appendix, Section 7.1.

A subset of Fig. 4.1, the $9,000cm^{-1}$ to $12,500cm^{-1}$ region of interest, is shown in Fig. 4.2. Thinner 0.75 mm samples were used for the $11,020cm^{-1}$ to $12,500cm^{-1}$ region. This material is very close to the YAG theoretical lossless transmittance in window regions of interest including near $1.064\mu m$ ($9395cm^{-1}$), and $0.532\mu m$ ($18,797cm^{-1}$); this indicates that parasitic absorption has been eliminated near fundamental transitions of interest.

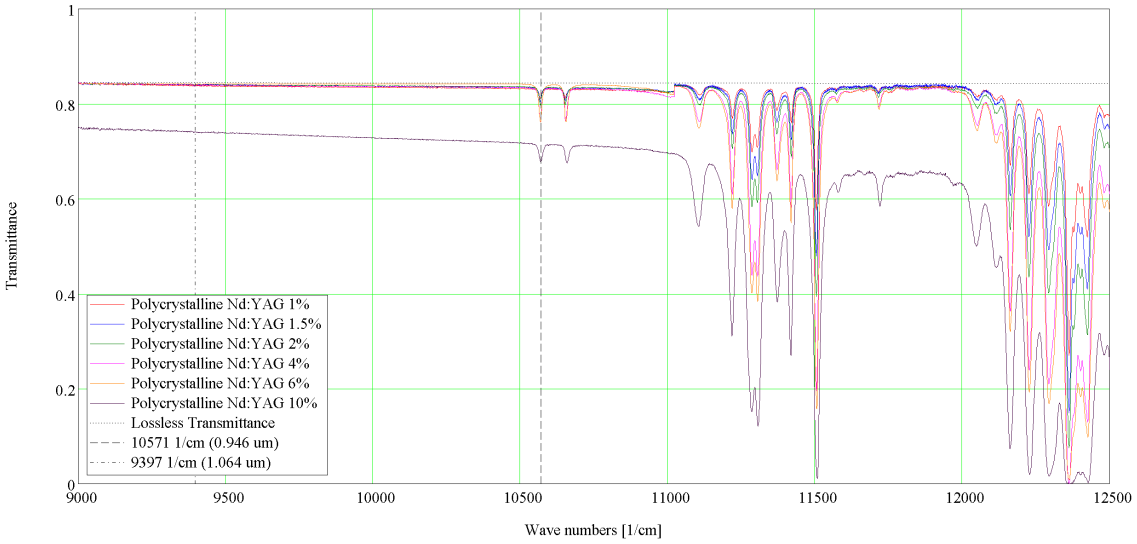

Figure 4.2: Konoshima polycrystalline YAG transmittance, pump and lasing regions, compared to theoretical lossless transmittance at room temperature. The $9397cm^{-1}$ ($1.064\mu m$) and $10,571cm^{-1}$ ($0.946\mu m$) transition are highlighted. Thinner 0.75 mm samples were used for the $11,020cm^{-1}$ to $12,500cm^{-1}$ region.

4.1.1.2 Extinction Coefficient

The extinction coefficient of Konoshima polycrystalline YAG and United Crystals single crystal YAG is presented in Figure 4.3. The absolute accuracy of the room temperature extinction coefficient is estimated to be $\Delta\beta_{ext} \approx 0.0035cm^{-1}$, based on the estimated transmittance error from Section 2.1.1. The extinction coefficient for polycrystalline and single crystal material is similar across much of the spectra of interest. Significant deviations between the polycrystalline and single crystal material occur in the infrared and ultraviolet. We hypothesize that increased polycrystalline extinction at wave numbers lower than $11,000cm^{-1}$ is attributed to an impurity band, increased polycrystalline extinction between $27,000cm^{-1}$ and $33,000cm^{-1}$ is scatter,

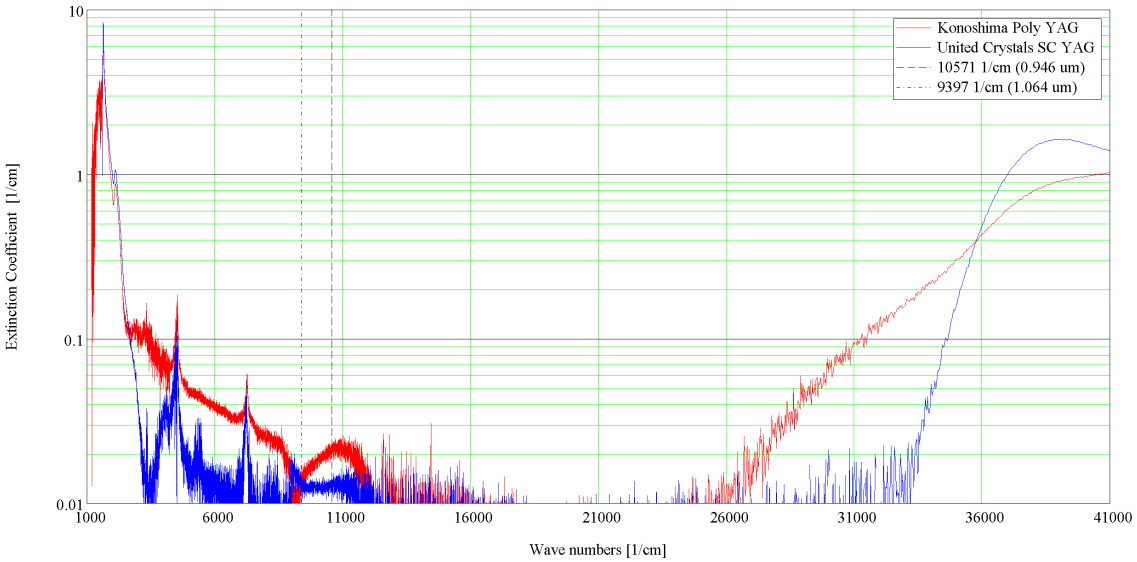

Figure 4.3: Extinction coefficient as a function of wavelength for Konoshima polycrystalline YAG and United Crystals single crystal YAG derived from transmittance measured at room temperature. The $9397cm^{-1}$ ($1.064\mu m$) and $10,571cm^{-1}$ ($0.946\mu m$) transition are highlighted.

and increased extinction in both the polycrystalline and single crystal material at higher than $33,000cm^{-1}$ is attributed to an impurity band.

4.1.1.3 Extinction Cross Section

For regions with doping absorption bands, dividing the extinction coefficient by the Nd doping concentration provides the room temperature extinction cross section. Note that values for the extinction cross section in regions without dopant absorption are not valid and should be disregarded. The extinction cross sections for Konoshima polycrystalline YAG, 1%, 1.5%, 2%, 4%, and 6% Nd doped is presented in Figure 4.4. The Konoshima 10% doped material was removed from Fig. 4.4 due to unacceptably

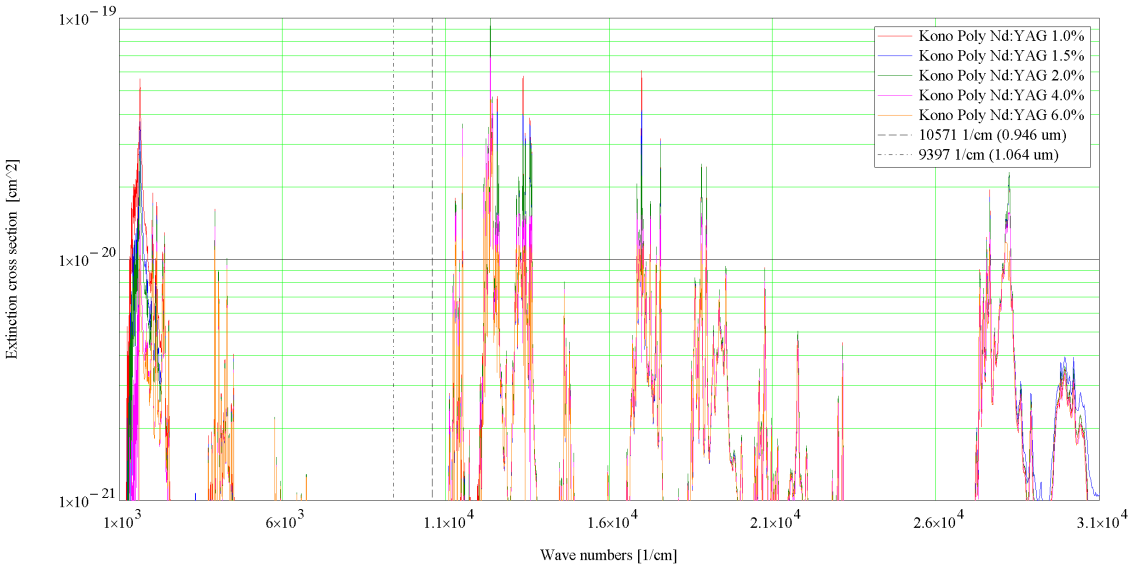

Figure 4.4: Extinction cross section as a function of wavelength for Konoshima polycrystalline Nd:YAG derived from transmittance measured at room temperature. The $9397cm^{-1}$ ($1.064\mu m$) and $10,571cm^{-1}$ ($0.946\mu m$) transition are highlighted. ©2013 IEEE.

high levels of scatter.

The Fig. 4.4 $11,000cm^{-1}$ to $12,500cm^{-1}$ region of interest is shown in Fig. 4.5. The extinction cross section absorption bands fall roughly on top of each other. This indicates the measured absorption bands have line width and band intensity that increases approximately linearly with doping percentage. The cross sections shown in Fig. 4.5 are again only valid in areas of Nd absorption; any cross section shown in a region without Nd absorption should be ignored.

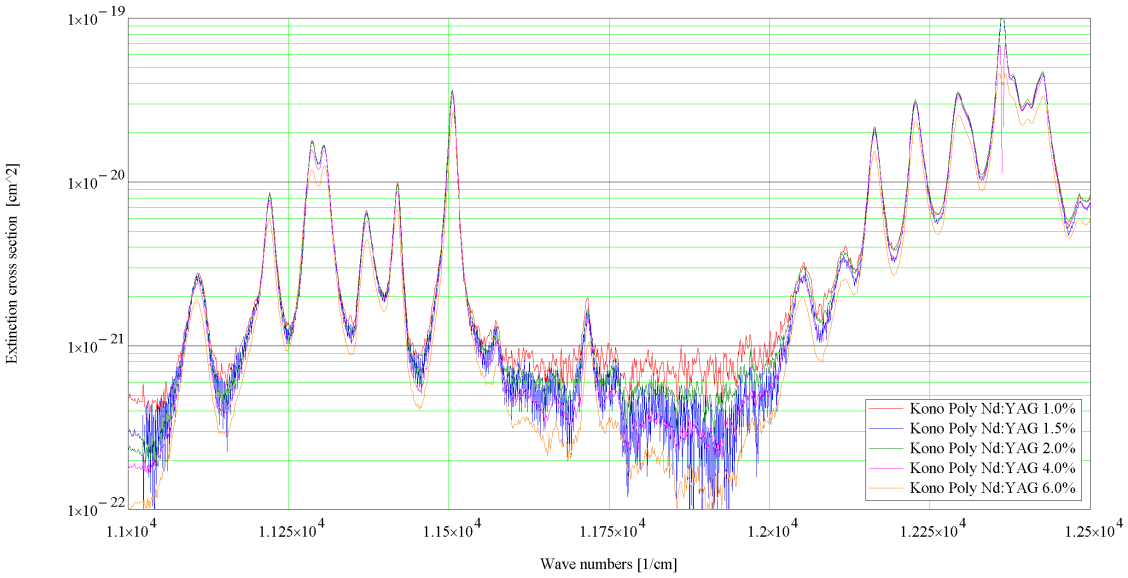

Figure 4.5: Extinction cross section, pump and lasing regions, as a function of wavelength for Konoshima polycrystalline Nd:YAG at room temperature.

4.1.1.4 Comparison of Polycrystalline vs Single Crystal Material Quality

A comparison of the calibrated transmittance of Konoshima Polycrystalline YAG, 1% Nd doping (also shown in Fig. 4.1) and United Crystals Single Crystal YAG, 1% Nd doping is presented in Fig. 4.6.

Figure 4.7 is the calibrated transmittance of undoped Konoshima Polycrystalline YAG compared with undoped United Crystals Single Crystal YAG. Both the polycrystalline and single crystal material closely follow the YAG theoretical lossless transmittance near fundamental and doubled Nd doped YAG transitions of interest.

An extinction cross section comparison of Konoshima polycrystalline Nd:YAG,

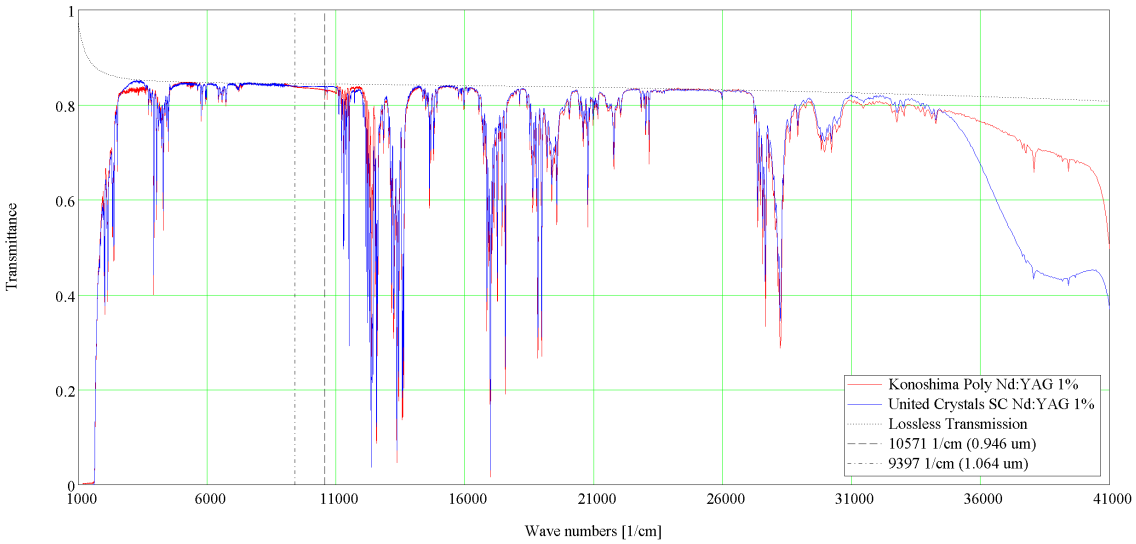

Figure 4.6: Transmittance of Konoshima polycrystalline Nd:YAG, 1% doping and United Crystals Single Crystal Nd:YAG, 1% doping compared to theoretical lossless transmittance measured at room temperature. ©2013 IEEE.

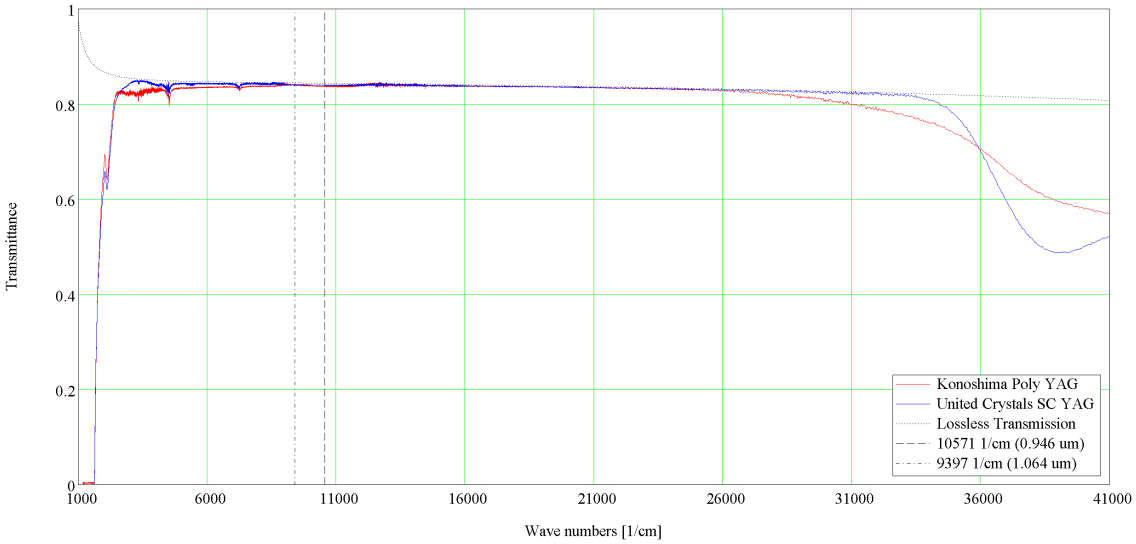

Figure 4.7: Transmittance as a function of wavelength for Konoshima polycrystalline YAG and United Crystals Single Crystal YAG compared to theoretical lossless transmittance at room temperature.

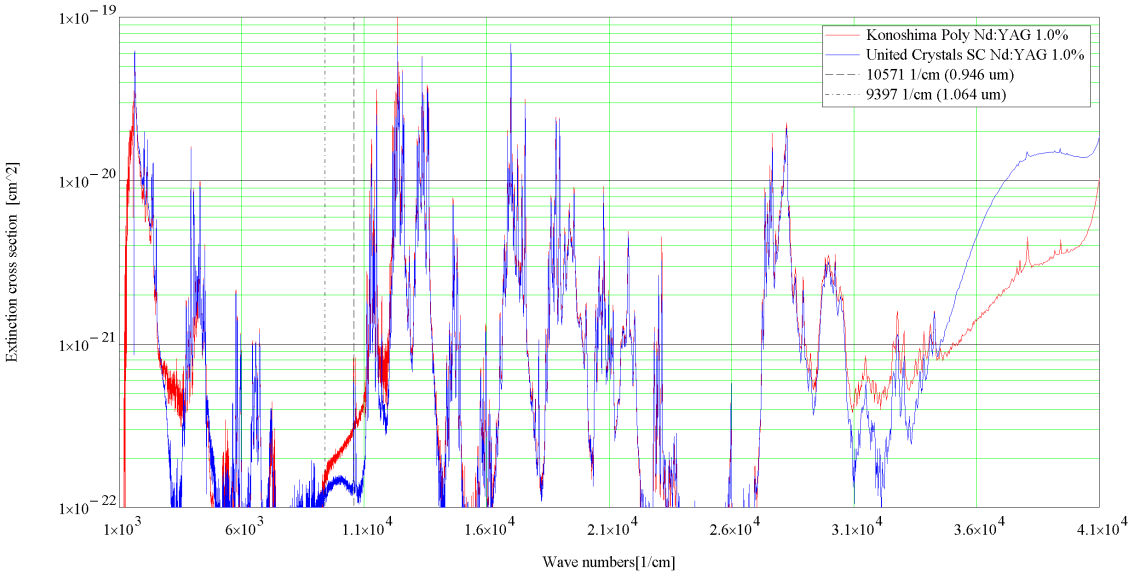

Figure 4.8: Extinction cross section as a function of wavelength for Konoshima polycrystalline Nd:YAG 1% and United Crystals single crystal Nd:YAG 1% at room temperature. ©2013 IEEE.

1% Nd doped and United Crystals single crystal Nd:YAG, 1% Nd doped is presented in Fig. 4.8. This shows that scatter and absorption in the polycrystalline material has been minimized across much of the measured spectra. The $9,000cm^{-1}$ to $13,000cm^{-1}$ region is notable as the polycrystalline material has a significantly greater extinction cross section compared to the single crystal material. As in Fig. 4.4, the cross sections shown in Fig. 4.8 are only valid in areas of Nd absorption and any cross section shown in a region without Nd absorption should be ignored.

4.1.1.5 Room Temperature Line Width

Concerning transmittance derived line width measurements, the minimum value of the feature is derived directly from the theoretical lossless transmittance and scatter-

ance. In fluorescence derived line width measurements, determining the feature zero value is difficult and potentially a significant source of error. An incorrect minimum feature value will lead to a smaller than actual line width measurement.

4.1.1.5.1 Calibration of Transmittance Line Width Data

Careful calibration is required for accurate transmittance or fluorescence data. Frequency calibration of transmittance is maintained by the use of a stabilized Helium Neon Laser. Intensity calibration of transmittance derived line width is relatively straight forward. Initial calibration of the instrument is performed by collecting a spectrum with an empty sample chamber providing a system baseline. Transmittance data should be aligned with the expected Fresnel reflection losses as predicted by the Sellmeier model for the material.[36] Transmittance departures from Fresnel losses are attributed to absorption and scatterance, given by the total power law shown in Eq. 3.35. The maximum value for transmittance is provided by Fresnel losses. The absorptance zero baseline is derived from the theoretical lossless transmittance minus scatterance losses.

4.1.1.5.2 Comparison Between Room Temperature Transmittance and Fluorescence Derived Line Width

A summary of transmittance and fluorescence derived line widths are shown in Table. 4.1. Only strong transitions with lower energy levels in the $^4I_{9/2}$ ground

Line Position $[1/cm]$	Trans line width $[1/cm]$ FWHM	Fluor line width $[1/cm]$ FWHM
11507	11.8	12.4
11423	11.6	11.6
11375	17.0	16.8
11307	16.2	14.4
11291	15.4	14.4
11223	15.0	14.8
11196	*	29.0
11112	*	27.0
10655	8.8	9.4
10571	9.0	9.2
9505	*	4.6
9479	*	6.4
9421	*	3.8
9397	*	4.2
9395	*	4.0
9361	*	10.4
9313	*	4.4
9277	*	9.2

Table 4.1: Summary of transmittance and fluorescence derived line widths at $293K$ for polycrystalline 1% Nd doped YAG. An asterisk indicates insufficient line strength for room temperature measurement.

state provide absorption features sufficiently above the noise floor to be measured in transmittance at room temperature. Measurement of the transitions with lower energy levels above the $^4I_{9/2}$ ground state manifold and weaker ground transitions require elevated temperatures or higher doping percentages for accurate transmittance measurement.

4.1.2 Doping Concentration Dependant Transmittance

A thermal dependence on line width in single crystal YAG has been applied by Kushida[9] and in polycrystalline YAG in section 4.1.3.5. An interest was shown in determining the doping concentration dependant line width in polycrystalline YAG. Using the generated absorption coefficient data, a classical oscillator model is fit to the transitions in the $0.808\mu m$ diode pump and $0.946\mu m$ regions, $12,618cm^{-1}$ to $10,571cm^{-1}$ for 1%, 1.5%, 2%, 4%, and 6% Nd doped polycrystalline YAG. A subset of the absorption coefficient data presented in Fig. 4.1 is shown in Figure 4.9 for Konoshima 1% Nd:YAG absorption coefficient and the classical oscillator model fit.

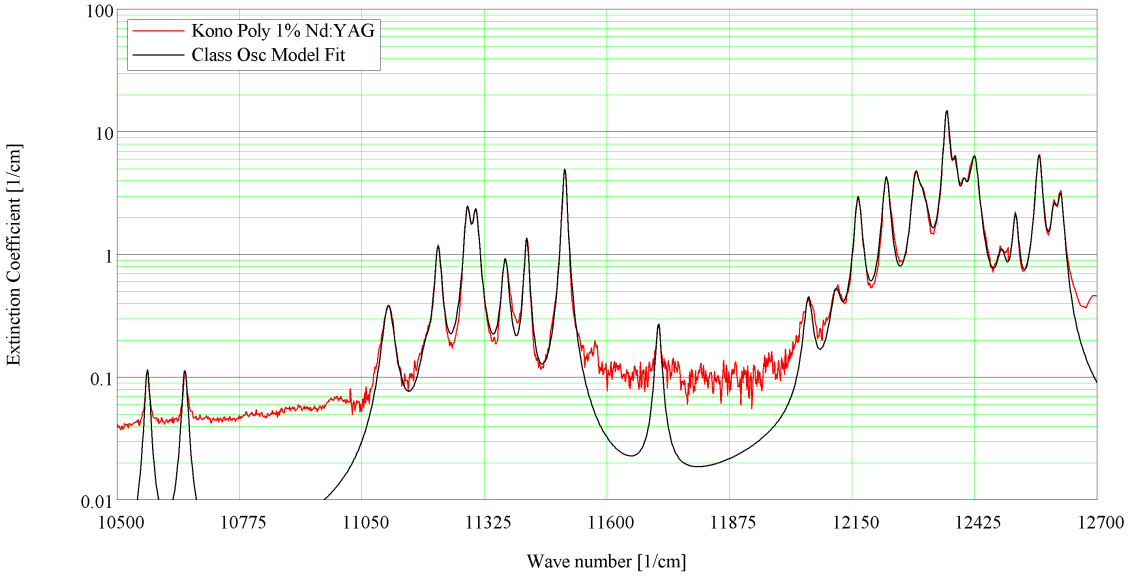

Figure 4.9: Extinction coefficient for Konoshima polycrystalline Nd:YAG 1% and classical oscillator model as a function of wave number.

A summary of the classical oscillator model parameters used for all doping dependent model fit are given in Tables 4.2, 4.3, and 4.4. In the case of strong absorption, the scatter component from the extinction cross section is negligible. Doping dependence on line width is confirmed in the tables below, however doping dependence on line width is found to be much weaker than thermal dependence. Absorption feature strength scales with doping percentage, provided the feature is integrated, up to 6% Nd doped YAG. Linear scaling is also predicted by the absorption coefficient Eq. 3.11 and integrated line shape Eq. 3.13.

This data from Tables 4.2, 4.3, and 4.4 indicates a line shift with doping percentage. This has not been modeled and will be addressed in a future effort.

4.1.3 Temperature Dependant Transmittance

4.1.3.1 Temperature Dependent Transmittance

Temperature dependent transmittance data was collected and a Lorentz line shape classical oscillator model was fit to select absorption features from the Nd:YAG ${}^4I_{9/2} \rightarrow {}^4F_{3/2}$ and ${}^4I_{11/2} \rightarrow {}^4F_{3/2}$ transitions. The representative sample of temperature dependent transmittance data is shown in Fig. 4.10.

Absorption feature strength, line width, and line position are all functions of temperature. Integrated line strength has been shown to follow the Maxwell-Boltzmann distribution.[18] Line width and line position are functions of the local crystalline

Poly 1% Nd:YAG			Poly 1.5% Nd:YAG		
Position ν_i $[cm^{-1}]$	Strength $\Delta\varepsilon_i$	Width Γ $[cm^{-1}]$ FWHM	Position ν_i $[cm^{-1}]$	Strength $\Delta\varepsilon_i$	Width Γ $[cm^{-1}]$ FWHM
11503.6	0.000780	5.8	11503.4	0.001120	5.8
11419.7	0.000225	6.0	11419.5	0.000340	6.0
11371.5	0.000207	8.5	11371.8	0.000310	8.5
11305.2	0.000460	8.3	11305.0	0.000660	8.3
11286.2	0.000490	7.5	11285.8	0.000780	7.7
11220.8	0.000270	8.0	11220.5	0.000405	8.0
11193.0	0.000035	15.0	11193.0	0.000055	15.0
11109.1	0.000157	14.0	11108.7	0.000225	14.0
10652.3	0.000022	6.5	10652.5	0.000027	6.5
10568.2	0.000021	6.1	10568.3	0.000025	6.1
12516.5	0.000300	7.5	12516.3	0.000440	7.5
12422.5	0.000910	10.5	12422.0	0.001000	11.5
12380.2	0.000500	6.5	12379.7	0.000650	8.0
12359.1	0.002100	7.2	12357.3	0.002950	8.8
12317.0	0.000160	6.0	12317.0	0.000250	10.0
12292.2	0.001200	9.8	12292.0	0.001800	9.8
12226.3	0.001050	9.0	12225.8	0.001550	9.0
12163.1	0.000730	8.6	12162.7	0.001100	8.8
12114.0	0.000155	13.0	12114.0	0.000200	13.0
12052.0	0.000110	10.0	12052.0	0.000170	12.0
11668.0	0.000000	0.0	11668.0	0.000000	0.0
11573.0	0.000000	0.0	11573.0	0.000040	10.0
12617.5	0.000390	8.0	12617.1	0.000470	8.0
12602.5	0.000300	8.0	12602.5	0.000410	8.0
12567.8	0.001070	8.0	12566.6	0.001400	9.0
12486.0	0.000220	12.0	12487.0	0.000280	12.0
12400.2	0.000480	9.0	12400.5	0.000600	9.0
12307.0	0.000310	7.0	12307.0	0.000380	7.0
11715.4	0.000050	7.0	11716.0	0.000061	7.0

Table 4.2: Summary of transmittance derived, doping dependent line strengths and widths at $293K$ for polycrystalline 1% and 1.5% Nd doped YAG. Transitions with insufficient strength for accurate fit were omitted from the table

Poly 2% Nd:YAG			Poly 4% Nd:YAG		
Position ν_i $[cm^{-1}]$	Strength $\Delta\varepsilon_i$	Width Γ $[cm^{-1}]$ FWHM	Position ν_i $[cm^{-1}]$	Strength $\Delta\varepsilon_i$	Width Γ $[cm^{-1}]$ FWHM
11502.8	0.001400	5.8	11501.8	0.002180	6.9
11419.2	0.000440	6.0	11418.5	0.000730	6.0
11371.4	0.000400	8.5	11371.0	0.000830	10.5
11304.7	0.000870	8.3	11303.8	0.001240	8.6
11285.5	0.001080	7.9	11284.1	0.002100	8.9
11220.2	0.000560	8.0	11219.3	0.001070	8.5
11193.0	0.000080	15.0	11193.0	0.000140	15.0
11108.3	0.000325	14.5	11107.0	0.000630	15.5
10652.8	0.000033	6.5	10654.4	0.000060	6.5
10568.6	0.000031	6.1	10568.8	0.000057	6.1
12516.0	0.000560	7.5	12513.8	0.001000	9.6
12421.0	0.001270	13.5	12420.0	0.001380	17.5
12378.7	0.000650	9.5	12377.0	0.000720	11.5
12354.2	0.003950	12.0	12351.3	0.004250	15.6
12316.0	0.000300	10.0	12317.0	0.000650	10.0
12291.3	0.002500	9.8	12288.5	0.004000	10.5
12225.2	0.002100	9.0	12222.8	0.003500	9.2
12162.3	0.001600	8.8	12160.5	0.002720	9.0
12114.5	0.000320	14.0	12114.1	0.000630	14.0
12050.5	0.000320	15.0	12050.4	0.000680	17.0
11668.0	0.000000	0.0	11668.0	0.000055	10.0
11573.5	0.000071	10.0	11575.4	0.000090	8.5
12616.4	0.000480	8.5	12618.5	0.000350	9.0
12602.0	0.000530	8.0	12603.5	0.000740	9.0
12566.0	0.001600	8.5	12564.4	0.001300	9.5
12483.0	0.000400	12.0	12481.0	0.000600	12.0
12399.5	0.000680	9.5	12398.0	0.000800	11.0
12307.0	0.000480	7.0	12307.0	0.000450	7.0
11716.7	0.000086	7.0	11716.7	0.000140	7.0

Table 4.3: Summary of transmittance derived, doping dependent line strengths and widths at $293K$ for polycrystalline 2% and 4% Nd doped YAG. Transitions with insufficient strength for accurate fit were omitted from the table

Poly 6% Nd:YAG		
Position ν_i $[cm^{-1}]$	Strength $\Delta\varepsilon_i$	Width Γ $[cm^{-1}]$ FWHM
11501.4	0.002300	7.2
11417.9	0.000980	6.6
11370.8	0.001050	11.0
11303.5	0.001350	8.6
11283.8	0.003000	10.5
11218.4	0.001380	8.8
11193.0	0.000150	15.0
11106.1	0.000830	16.0
10655.6	0.000068	6.5
10569.0	0.000064	6.1
12510.0	0.001080	11.0
12419.5	0.001600	21.5
12376.5	0.000700	13.5
12348.5	0.004550	19.0
12315.0	0.000800	10.0
12287.3	0.004650	11.8
12222.0	0.003700	9.3
12159.6	0.003450	9.5
12114.1	0.000780	14.0
12049.6	0.000790	17.0
11668.0	0.000055	10.0
11576.2	0.000106	8.5
12618.5	0.000320	10.0
12603.5	0.000780	10.0
12563.5	0.001200	10.5
12483.0	0.000650	12.0
12396.5	0.000750	13.0
12307.0	0.000300	7.0
11718.2	0.000160	7.0

Table 4.4: Summary of transmittance derived, doping dependent line strengths and widths at $293K$ for polycrystalline 6% Nd doped YAG. Transitions with insufficient strength for accurate fit were omitted from the table

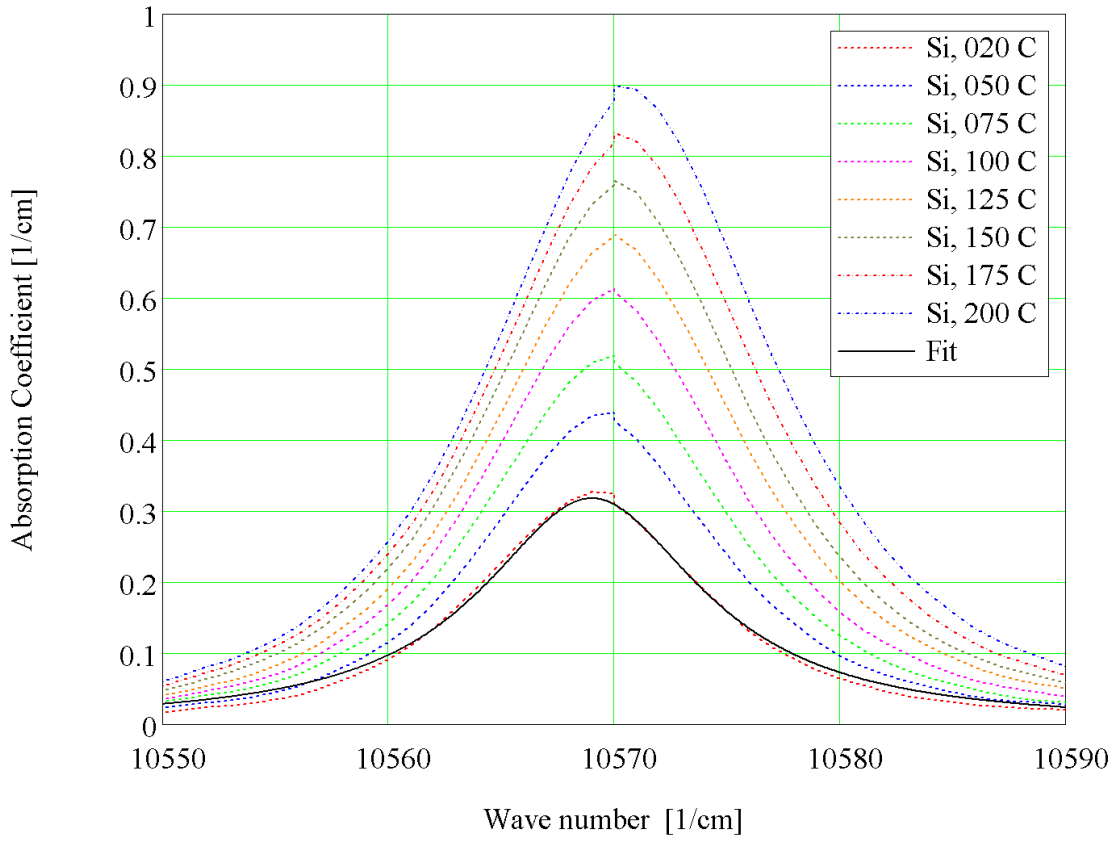

Figure 4.10: Temperature dependent line width model for 6% Nd doped polycrystalline YAG collected near $0.946\mu m$.

field non-uniformity. Flaws in the crystalline lattice and doping impurities give rise to temperature dependent, inhomogeneous line broadening and stress induced line shifts.[20]

4.1.3.2 Temperature Dependent Absorption Coefficient

Figure 4.11 is a plot of experimental data and Eq. 3.10 for the peak absorption coefficient for the ${}^4F_{3/2} \rightarrow {}^4I_{9/2}$ $(11423-852cm^{-1})$ transition in Konoshima polycrystalline 1% and 6% Nd doped YAG. The $0.946\mu m$ absorption feature is temperature

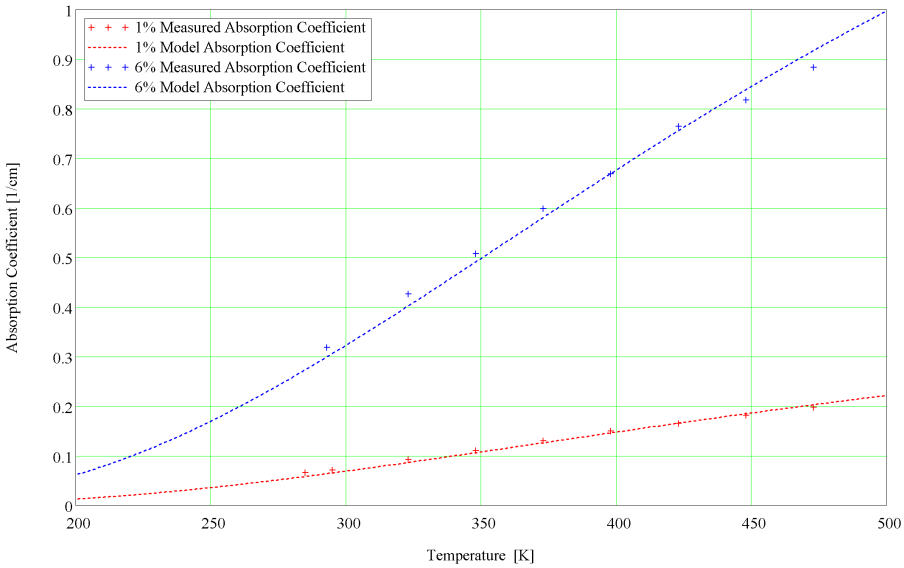

Figure 4.11: Peak absorption coefficient at $0.946\mu m$ for Konoshima polycrystalline 1% and 6% Nd doped YAG as a function of temperature.

broadened. To compensate, the area of the absorption feature is integrated. The area is derived by fitting the $0.946\mu m$ absorption feature to a modified Lorentz line shape, Eq. 3.12. The integrated absorption is converted to a peak value by dividing by the measured line width, Eq. 3.17. The lower energy level $v_l = 852cm^{-1}$ that is used, compares favorably with the values used by Wallace and Harris, Fan and Byer, Kaminskii,.[2,16,41] An scatter coefficient model value of $\beta_{sca} = 0.009cm^{-1}$ and $\beta_{sca} = 0.011cm^{-1}$ is used for the Konoshima polycrystalline 1% and 6% Nd doped YAG, respectively, given in Table 4.6.

Model and experimental data fit is excellent. The model indicates the extinction coefficient in Konoshima polycrystalline 1% Nd doped YAG is scatter dominated below $\sim 150K$. Efficiency improvements, by cooling the gain media to decrease the

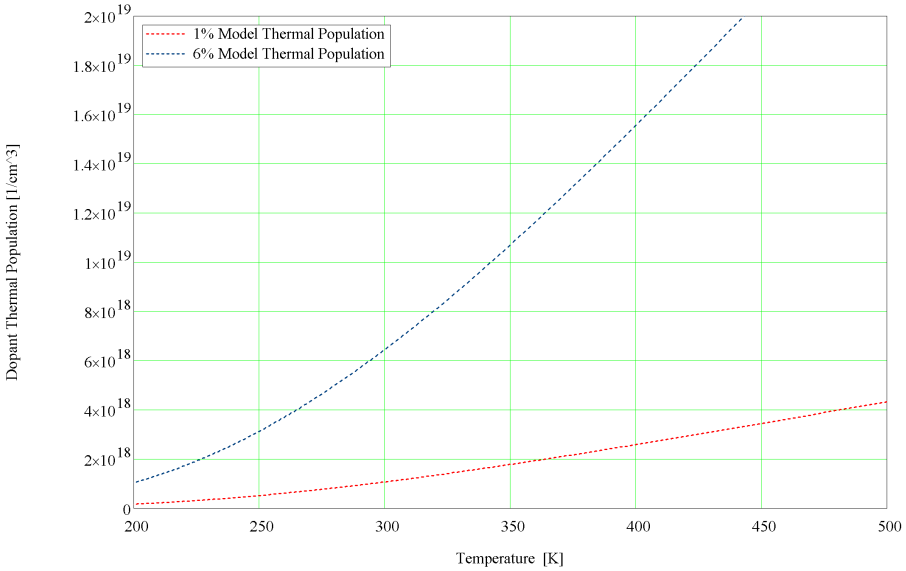

Figure 4.12: Model temperature dependant population at $852(cm^{-1})$ for 1% and 6% Nd doped YAG.

lower level thermal population of the $^4F_{3/2} \rightarrow {}^4I_{9/2}$ transition, are limited by this scatter floor.

4.1.3.3 Thermal Population

Using Eq. 3.6, we derived the temperature dependant population at $852cm^{-1}$, shown in Fig. 4.12. A total dopant level model value of $N_0 = 1.38x10^{20}1/cm^3$ and $N_0 = 8.28x10^{20}1/cm^3$ is used for the 1% and 6% doped material, respectively.

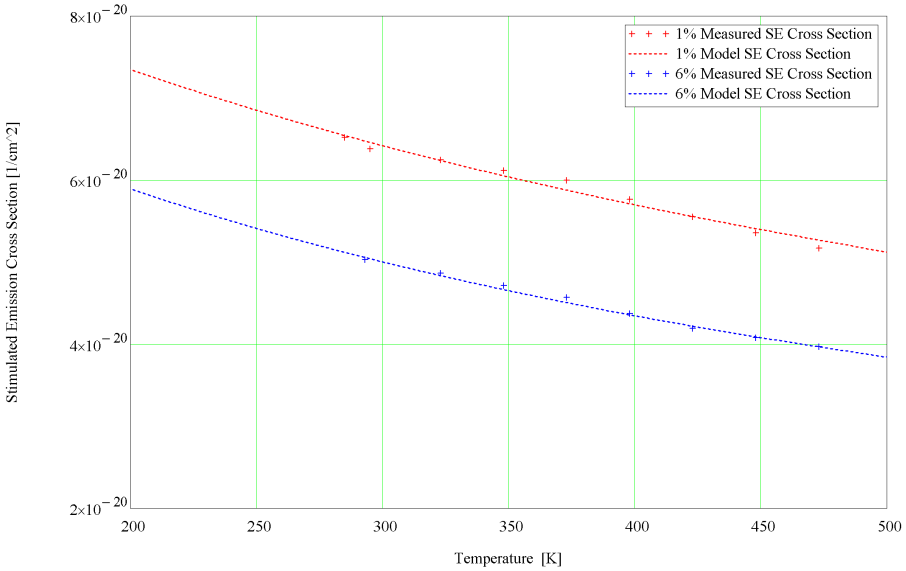

Figure 4.13: Peak stimulated emission cross section at $0.946\mu m$ for Konoshima polycrystalline 1% and 6% Nd doped YAG; experimental data (+) and model extinction coefficient (dotted line) as a function of temperature.

4.1.3.4 Temperature Dependant Stimulated Emission Cross Section

The line center stimulated emission cross section has a minor temperature dependence over the range measured, shown in Fig. 4.13, due to line broadening at higher temperatures. The measurement derived $0.946\mu m$, $300K$ line center stimulated emission cross section $\sigma_{em} = 6.4x10^{-20}cm^2$, and $\sigma_{em} = 5.0x10^{-20}cm^2$ was used for the 1% and 6% doped material, respectively. The $0.946\mu m$, 1% Nd:YAG value and compares favorably with the emission cross section used by Wallace and Harris, Fan and Byer,.[2,41] The line center stimulated emission cross section has a minor doping percentage dependance due to line broadening, the integrated stimulated emission cross

section is doping percentage independent.

The absorption features around $0.946\mu m$ were found to be a modified Lorentzian line shape, given by Eq. 3.12. The line width was found to be temperature dependant.

4.1.3.5 Temperature Dependent Line Width

YAG is often operated at temperatures above and below room temperature. Kushida has modeled the temperature dependent line broadening in single crystal YAG and confirmed McCumber theory provides a good fit to experimental data[20].[9] A series of temperature dependent measurements, in the $283K$ to $473K$ range were performed on 1% and 6% Nd doped polycrystalline YAG. From these measurements a temperature dependent line width model for multiple transitions of interest in polycrystalline was developed. Of particular interest to the authors are the ${}^4I_{9/2} \rightarrow {}^4F_{3/2}$ transitions. Unfortunately, the ${}^4I_{11/2} \rightarrow {}^4F_{3/2}$ YAG transitions are not measurable in transmittance at 1% Nd doping and at room temperature. Measurements at elevated temperatures and doping levels were used to establish line width models for the ${}^4I_{11/2} \rightarrow {}^4F_{3/2}$ transitions. A summary of all coefficients is provided in Table 4.5.

4.1.3.5.1 Temp Dependent Transmittance ${}^4I_{9/2}$ Manifold Band

The ${}^4I_{9/2}$ manifold comprises the ground state energy level in Neodymium. Absorption features from this level are generally strong. Using our temperature de-

Sample	$\Gamma_i(0)$	α_i
Poly 1% $0.938\mu m$	8.4	33
Poly 1% $0.946\mu m$	9.4	26
Kushida 1% $0.946\mu m$	6.0	50
Poly 6% $0.938\mu m$	11.4	30
Poly 6% $0.946\mu m$	10.4	28
Poly 6% $1.061\mu m$	2.2	49
Poly 6% $1.064\mu m$	7.8	22
Kushida 1% $1.061\mu m$	0.64	53

Table 4.5: Summary of coefficient used in modified Kushida line width model, Eq. 3.4. Note that coefficients from Kushida are for single crystal YAG.[9]

pendent 1% Nd doped polycrystalline YAG data, we fit the Kushida model with modified intrinsic and temperature dependent coefficients, Fig. 4.14.[9] Kushida has provided line width model fits for a limited number of transitions, direct comparison between single crystal and polycrystalline model fit is possible for $0.946\mu m$ transition. Based on the coefficients derived, two general trends are apparent. The $\Gamma_i(0)$ temperature insensitive coefficient is greater for polycrystalline vs single crystal material. The temperature insensitive component is driven localized random crystal strain, which is expected to be locally higher at the polycrystalline grain boundaries. The α_i temperature dependent coefficient is weaker for polycrystalline versus single crystal material. This coefficient is driven by the Debye temperature and interaction of phonon-impurity interactions. The temperature dependent phonon-impurity interactions appear to be reduced in the polycrystalline material.

Temperature dependent 6% Nd doped polycrystalline YAG is fit to a modified Kushida model, Fig. 4.15.[9] When the polycrystalline YAG dopant is increased to

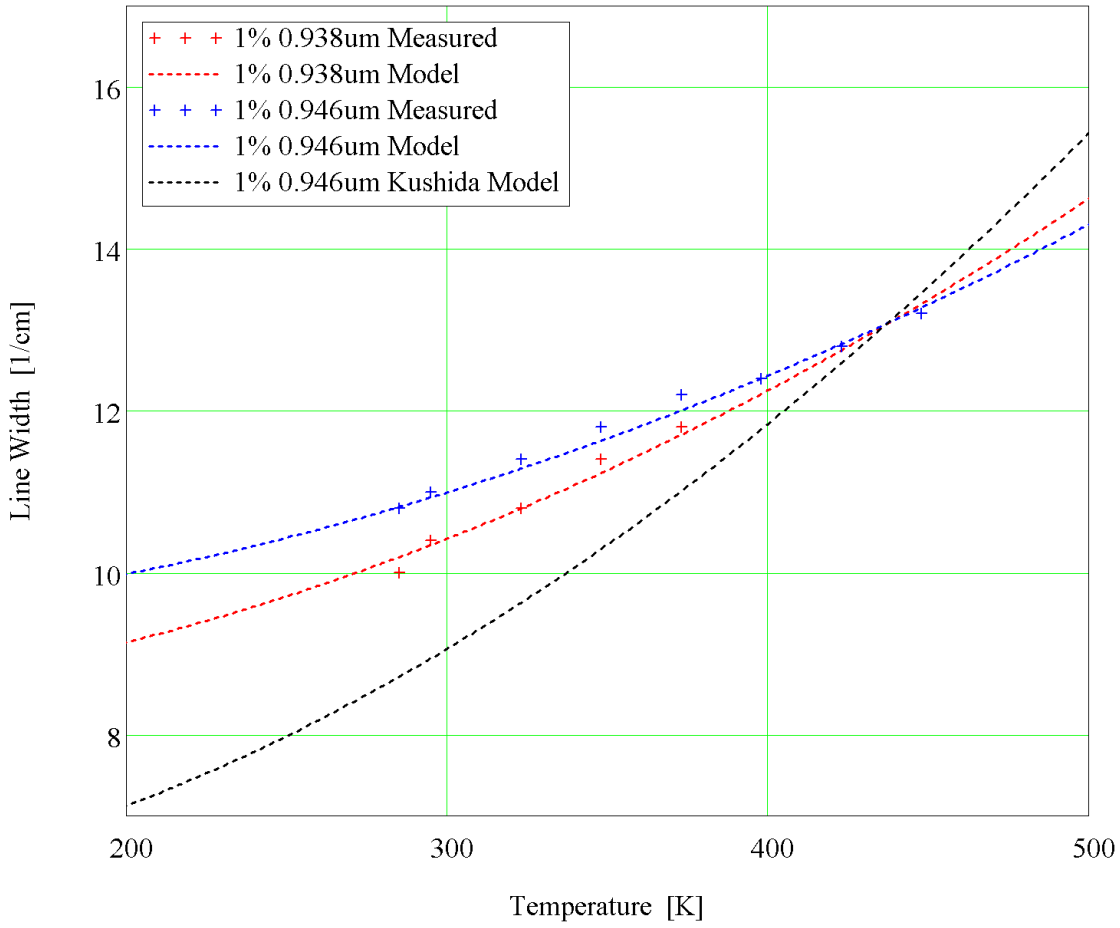

Figure 4.14: Line width measurements and model for ${}^4I_{9/2} \rightarrow {}^4F_{3/2}$ transitions in polycrystalline 1 % Nd doped YAG. The Kushida model for $0.946\mu m$ transition in single crystal 1% Nd doped YAG shown for comparison purposes.

6% Nd, the $\Gamma_i(0)$ temperature insensitive coefficient increases. This increase is to be expected as increase in the percentage of Yittria substitutions and the size difference between Yittria and Neodymium will lead to increase lattice strain relative to the 1% Nd doped polycrystalline. The α_i temperature dependent coefficient line width trends present in the 1% doped material also persist in the 6% doped material.

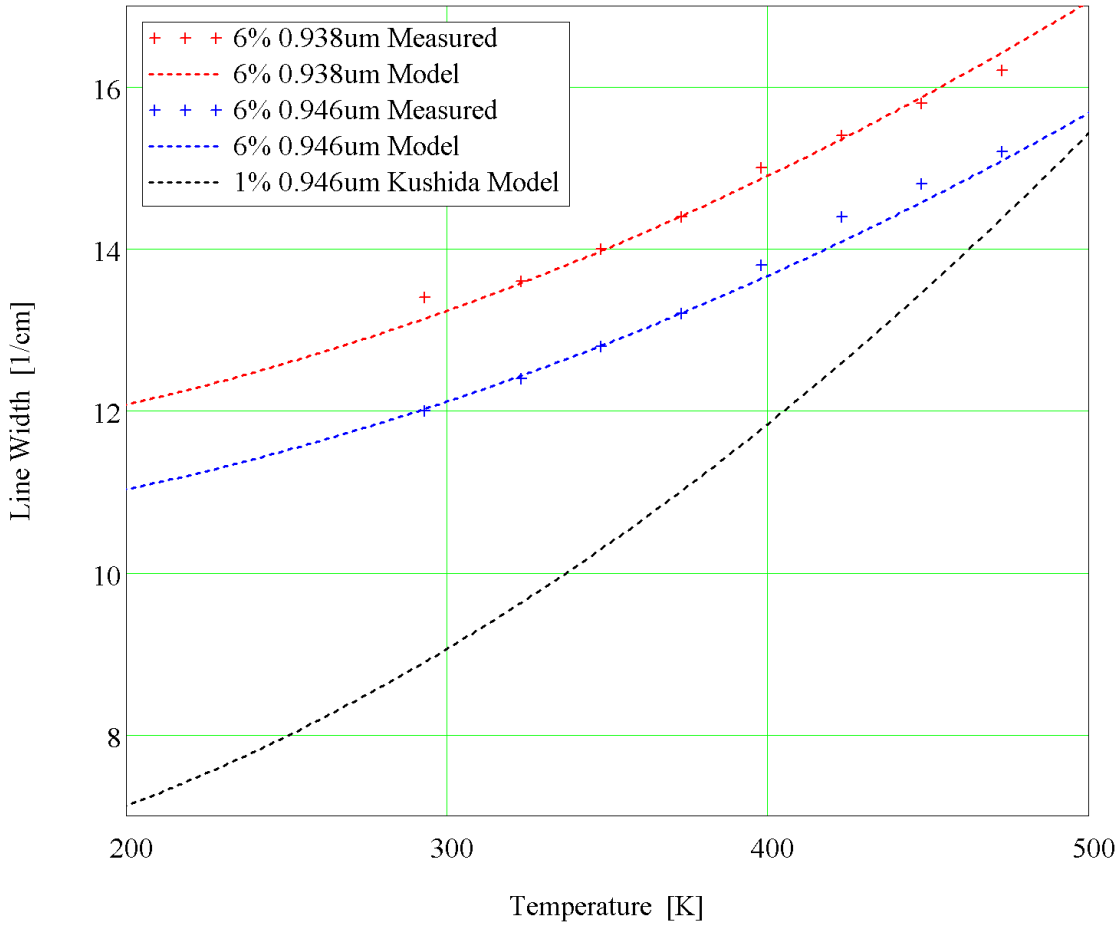

Figure 4.15: Line width measurements and model for ${}^4I_{9/2} \rightarrow {}^4F_{3/2}$ transitions in polycrystalline 6 % Nd doped YAG. The Kushida model for $0.946\mu m$ transition in single crystal 1% Nd doped YAG shown for comparison purposes.

4.1.3.5.2 Temp Dependent Transmittance ${}^4I_{11/2}$ Manifold Band

The ${}^4I_{11/2}$ energy manifold is located roughly $2002cm^{-1}$ above ground state. There is limited thermal population to levels within this manifold leading to much weaker absorption features. This can be partially compensated by increasing the sample temperature and increased dopant levels. Direct comparison to transmittance 1% Nd doped polycrystalline YAG is not possible with the sample temperatures avail-

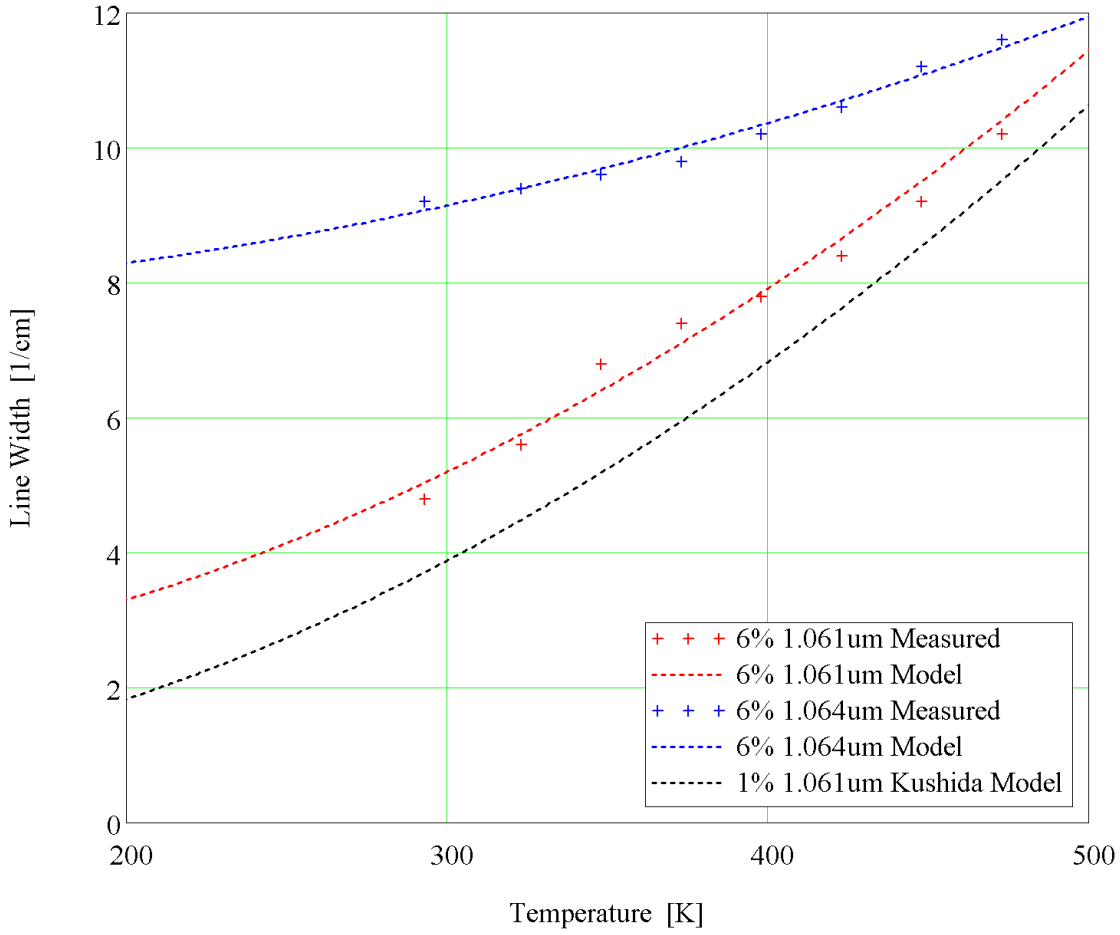

Figure 4.16: Line width measurements and model for ${}^4I_{11/2} \rightarrow {}^4F_{3/2}$ transitions in polycrystalline 6% Nd doped YAG. The Kushida model for $1.061\mu m$ transition in single crystal 1 % Nd doped YAG shown for comparison purposes.

able. Temperature dependent 6% Nd doped polycrystalline YAG is fit to a modified Kushida model, Fig. 4.16.[9] Kushida has provided a line width model fit for the $1.061\mu m$ transition. Again $\Gamma_i(0)$ temperature insensitive coefficient is greater for polycrystalline vs single crystal material. At the $1061\mu m$ transition, the polycrystalline and single crystal α_i temperature dependent coefficient is comparable.

4.2 Scatter

4.2.1 Total Integrated Scatter

Data were collected at two laser incident powers to accurately measure specular/near specular scatterance and oblique angle Lambertian scatterance. The composite signal-to-noise of detector/lock-in-amplifier and multiple laser incident powers achieved a dynamic range of roughly eight orders of magnitude. A representative sample of polycrystalline BTPDF and BRPDF experimental data and model fit are shown in Fig. 4.17. Inspection of the BRPDF plot will reveal a dropout in the data near 0 degrees due to instrument blockage. Data collected within the instrument blockage range provides information on the system noise floor. The minimum BSPDF measurement is more than an order above the noise floor. Note that data near ±90 degrees is not valid due to the sample ground edge.

A comparison between polycrystalline and single crystal material BRPDF is presented in Fig. 4.18. Comparison of these plots suggests both materials are of high optical quality. The shape and magnitude of Lambertian and diffuse components of scatterance are nearly identical indicating the bulk scatter properties of the materials are similar. Slight differences in the near-specular scatterance indicate differences in surface polish quality and may be reduced by improved polishing. The TIS_D reveals the polycrystalline material has a slightly lower scatter coefficient than the single crystal material.

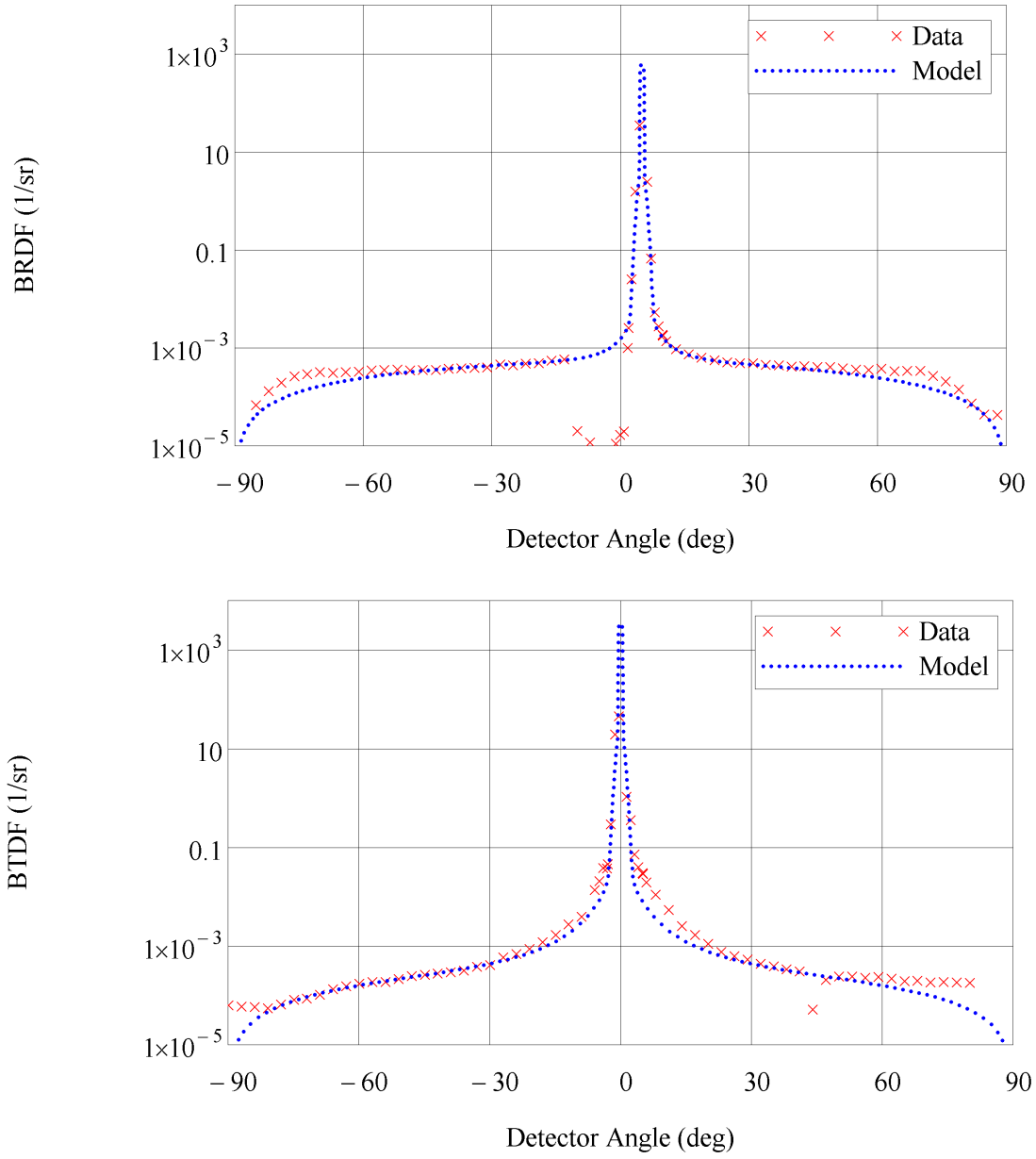

Figure 4.17: Scatterance data undoped polycrystalline YAG, BRDF (top) and BTDF (bottom), 5 degree incidence angle, from 1.064 um Nd:YAG laser.

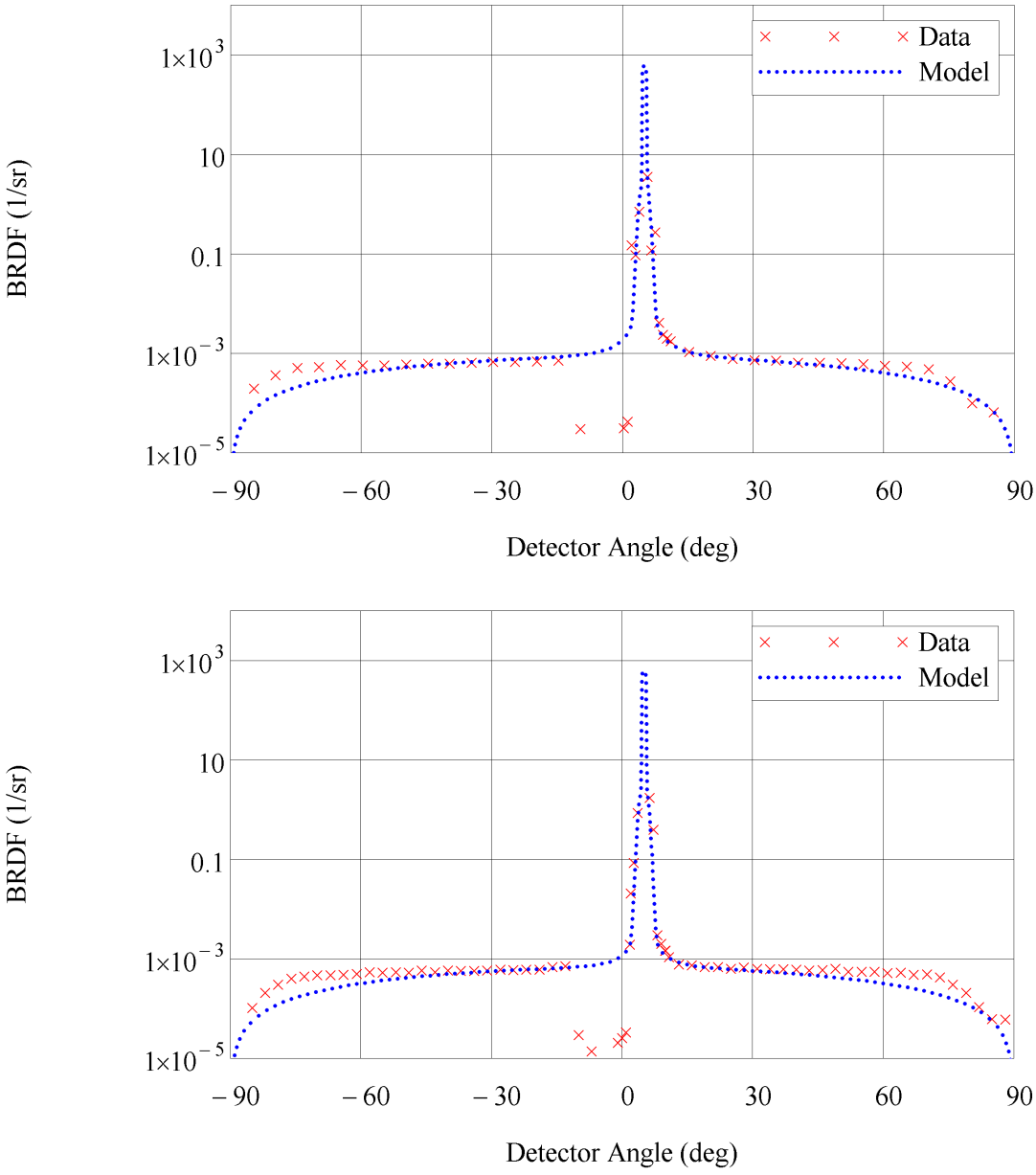

Figure 4.18: Scatterance data 1% Nd doped polycrystalline YAG (top) and single crystal YAG (bottom), BRDF, 5 degree incidence angle, from 1.064 um Nd:YAG laser.

$0.405\mu m$	$\tau_l + \rho_l$	$\tau_d + \rho_d$	$\tau_{ns} + \rho_{ns}$	$\tau_{in} + \rho_{in}$	TIS_D	β_{sca}**[1/cm]**
Poly undoped YAG	0.0060	0.0027	0.0026	0.99	0.009	**0.027**
Poly Nd:YAG, 1.0%	0.0070	0.0032	0.0030	0.98	0.010	**0.030**
Poly Nd:YAG, 1.5%	0.0055	0.0036	0.0028	0.98	0.009	**0.027**
Poly Nd:YAG, 2.0%	0.0060	0.0031	0.0027	0.98	0.009	**0.027**
Poly Nd:YAG, 4.0%	0.0060	0.0030	0.0031	0.98	0.009	**0.027**
Poly Nd:YAG, 6.0%	0.0087	0.0165	0.0045	0.98	0.025	**0.075**
SC YAG	0.0037	0.0076	0.0032	0.99	0.011	**0.037**
SC Nd:YAG, 1.0%	0.0040	0.0043	0.0032	0.99	0.008	**0.028**
$0.532\mu m$	$\tau_l + \rho_l$	$\tau_d + \rho_d$	$\tau_{ns} + \rho_{ns}$	$\tau_{in} + \rho_{in}$	TIS_D	β_{sca}**[1/cm]**
Poly undoped YAG	0.0020	0.0057	0.0024	0.99	0.008	**0.023**
SC YAG	0.0030	0.0045	0.0025	0.99	0.008	**0.024**
$1.064\mu m$	$\tau_l + \rho_l$	$\tau_d + \rho_d$	$\tau_{ns} + \rho_{ns}$	$\tau_{in} + \rho_{in}$	TIS_D	β_{sca}**[1/cm]**
Poly undoped YAG	0.0018	0.0007	0.0024	0.99	0.003	**0.007**
Poly Nd:YAG, 1.0%	0.0024	0.0007	0.0024	0.99	0.003	**0.009**
Poly Nd:YAG, 1.5%	0.0019	0.0005	0.0024	0.99	0.002	**0.007**
Poly Nd:YAG, 2.0%	0.0022	0.0006	0.0023	0.99	0.003	**0.008**
Poly Nd:YAG, 4.0%	0.0014	0.0004	0.0024	0.99	0.002	**0.005**
Poly Nd:YAG, 6.0%	0.0025	0.0013	0.0025	0.99	0.004	**0.011**
SC YAG	0.0025	0.0018	0.0027	0.99	0.004	**0.012**
SC Nd:YAG, 1.0%	0.0026	0.0005	0.0029	0.99	0.003	**0.010**
$1.55\mu m$	$\tau_l + \rho_l$	$\tau_d + \rho_d$	$\tau_{ns} + \rho_{ns}$	$\tau_{in} + \rho_{in}$	TIS_D	β_{sca}**[1/cm]**
Poly undoped YAG	0.0010	0.0003	0.0019	0.99	0.001	**0.004**
Poly Nd:YAG, 1.0%	0.0009	0.0004	0.0019	0.97	0.001	**0.004**
Poly Nd:YAG, 1.5%	0.0010	0.0003	0.0019	0.95	0.001	**0.004**
Poly Nd:YAG, 2.0%	0.0010	0.0004	0.0016	0.93	0.001	**0.004**
Poly Nd:YAG, 4.0%	0.0009	0.0004	0.0011	0.89	0.001	**0.004**
Poly Nd:YAG, 6.0%	0.0010	0.0005	0.0011	0.82	0.001	**0.004**
SC YAG	0.0009	0.0006	0.0013	0.98	0.002	**0.005**
SC Nd:YAG, 1.0%	0.0011	0.0004	0.0016	0.97	0.002	**0.005**

Table 4.6: TIS summary of Konoshima polycrystalline and United Crystals single crystal, multiple doping levels, 5 degree incidence angle. β_{sca} is derived by dividing the TIS by the sample path length L.

A summary of the component integrated scatter, based on model fit, for all samples and wavelengths is presented in Table 4.6. Also presented is a total integrated scatter diffuse and scatter coefficient. Analysis of this summary reveals the polycrystalline material has less or equivalent scatter than the single crystal material at all measured wavelengths. At $1.064\mu m$, the polycrystalline material has a roughly 25% lower scatter coefficient than single crystal. When selecting material, absorptance and scatterance must be considered together. Absorptance measurements may be derived from laser calorimetry measurements, which are outside the scope of the present work. From this scatter analysis, polycrystalline materials are to be preferred over a single crystal material.

4.2.2 Polycrystalline YAG Grain Size

The grain structure of the polycrystalline material was imaged using a scanning electron microscope (SEM), a representative image is provided in Fig. 4.19. Figures for each doping percentage are included in the Appendix, Section 7.2. The Heyn Linear Intercept Procedure was used to determine mean grain size. Additional details on the measurement procedure are detailed in ASTM E112-10 Standard Test Methods for Determining Average Grain Size.[28] We report the mean grain size of the undoped and 1% to 6% Nd doped polycrystalline YAG in Table 4.7. The average of all measured grain sizes was $1.27\mu m$; this average compares favorably to the measurement of about $2\mu m$ reported by H. Yagi, et al.[29]

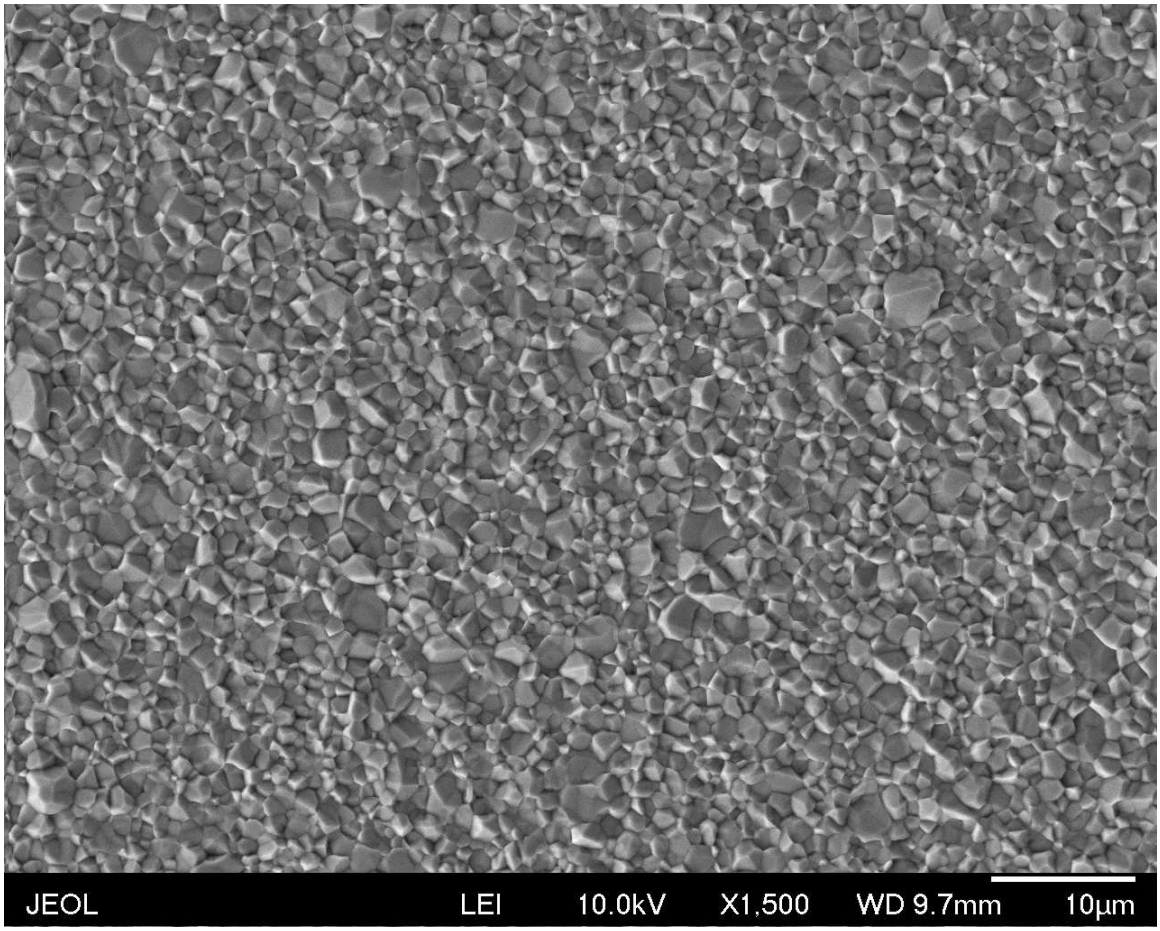

Figure 4.19: Representative SEM image, 1% Nd doped polycrystalline YAG.

4.2.3 Polycrystalline YAG Sintering Agent

Polycrystalline YAG material requires a sintering or flow agent to achieve full theoretical density. Achieving density as close to 100% as possible is important as any residual voids will lead to scatter, discussed in Section 4.2.4. The exact sintering agents and quantity used in Konoshima polycrystalline YAG is proprietary information and has not been confirmed by the company. There are several interesting papers that discuss sintering agents and include authors affiliated with Konoshima.[35345450]

	$GrainSize$ $[\mu m]$
Konoshima undoped poly YAG	1.12
Konoshima poly Nd:YAG, 1.0% Nd	1.23
Konoshima poly Nd:YAG, 1.5% Nd	1.69
Konoshima poly Nd:YAG, 2.0% Nd	1.11
Konoshima poly Nd:YAG, 4.0% Nd	0.90
Konoshima poly Nd:YAG, 6.0% Nd	1.54

Table 4.7: Summary of SEM mean grain size data for 1% to 6% Nd doped polycrystalline YAG.

From these publications, we hypothesized the sintering agent may be a compound containing silicon, specifically Tetraethyl Orthosilicate (TEOS)with the chemical formula $Si(OC_2H_5)_4$ in concentration of 0.5 $mass\%$. TEOS takes the form of four hydrocarbon chains bound to a central Si atom. During hot isostatic press and high temperature vacuum sintering, the hydrocarbon chains in TEOS would burn off and Si would remain. This Si would collect at the polycrystalline grain boundaries, pacifying any un-bonded atoms present at the boundaries of polycrystalline grains. Many of these periphery atoms are oxygen, resulting in silica SiO_2.

To confirm the presence of Si in the polycrystalline YAG samples, Inductively coupled plasma mass spectrometry (ICP-MS) measurements were conducted on 1% and 6% Nd doped polycrystalline YAG by Evans Analytical Group. ICP-MS measurements are conducted by dissolving the sample into a known acid, ionizing the acid mixture with an inductively coupled plasma, and using a mass spectrometer to measure the atomic percentage of each atom. The ICP-MS was calibrated to measuring quantities in the $1 - 1000ppm$. The test report confirmed the presence of

Si at $24ppm\ mass\%$ and $25ppm\ mass\%$ for 1% and 6% Nd doped polycrystalline YAG by Konoshima, respectively. A $25ppm\ mass\%$ of Si is a nearly identical to the expected residual Si concentration given TEOS sintering agent concentration of $0.5\ mass\%$. Silica SiO_2 has an index of roughly $n = 1.45$ and is the value used for the coated sphere model in Section 4.2.4. This excellent model index fit provides further confirmation of the presence of a silicon based sintering agent.

4.2.4 Sources of Scatter

4.2.4.1 0% to 4% Nd Doped YAG

Using the data from Table 4.7 a Kubelka-Munk model was applied. The coated sphere ADA was used for the component of scatter due to residual sintering material agent. We hypothesize that a residual sintering agent of index near 1.45 is present in all polycrystalline samples. This index would be consistent with known sintering agents used for polycrystalline YAG production.[34,35,50,54]

The data fit indicated common model coefficients for Konoshima undoped YAG and 1-4% Nd doped YAG. Particle sizes were obtained from Table 4.7, a Sellmeier model for YAG was obtained from Ref.,[36] and coating thickness was obtained from Ref.[34] A representative sample of the Kubelka-Munk model fit for undoped polycrystalline YAG is presented in Fig. 4.20.

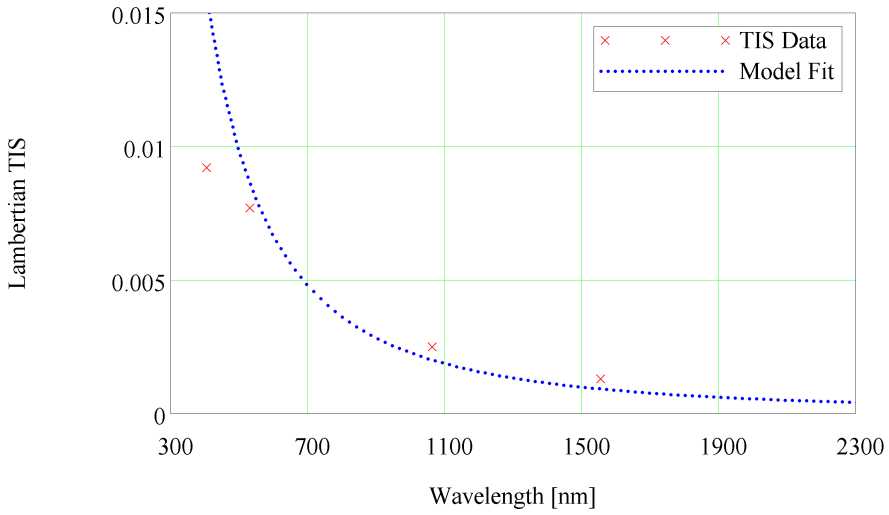

Figure 4.20: Kubelka-Munk model using coated sphere ADA for undoped polycrystalline YAG.

4.2.4.2 6% Nd Doped YAG

For Konoshima 6% Nd doped polycrystalline YAG, grain to grain index variations are present. The mechanism for this index variation is unknown. A combination of the residual sintering agent coated sphere ADA and a grain to grain index variation spherical ADA model was used. The Kubelka-Munk model fit for 6% Nd doped polycrystalline YAG is presented in Fig. 4.21.

4.2.4.3 Single Crystal YAG

When Single crystal YAG is grown by the Czochralski technique, a small amount of rotation is used when pulling the crystal from the crucible. This technique reduces but does not eliminate strain in the crystalline lattice.[15] This strained lattice results in scatter and is modeled using a spherical ADA to approximate index variation in

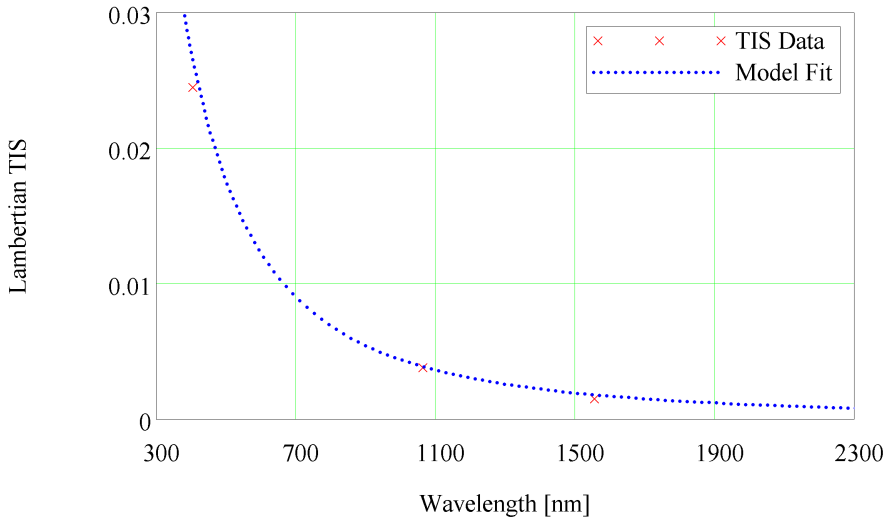

Figure 4.21: Kubelka-Munk model using spherical ADA and coated sphere ADA for 6% Nd doped polycrystalline YAG.

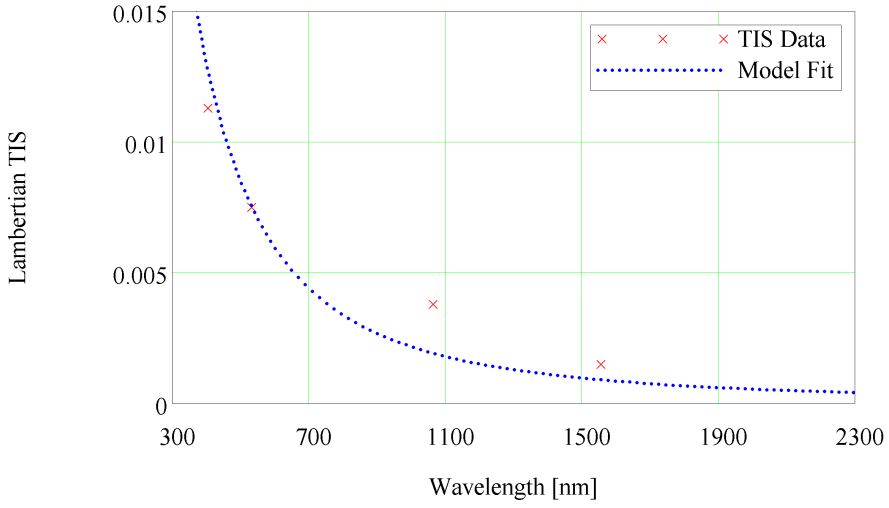

Figure 4.22: Kubelka-Munk model using spherrical ADA for undoped single crystal YAG.

single crystal YAG. The Kubelka-Munk model fit for undoped single crystal YAG is presented in Fig. 4.22.

4.2.4.4 Summary of Kubelka-Munk Model Terms

A summary of Kubelka-Munk model terms is presented in Table 4.8.

	$ADA\ Mdl$	$p(r)$	ρ
Kono poly 0% to 4% Nd:YAG	Coated Sp	$0.6\mu m$	$1.7x10^8$
Kono poly 6% Nd:YAG	Spherical	$0.6\mu m$	$2.0x10^9$
	Coated Sp	$0.6\mu m$	$1.7x10^8$
United SC 0% and 1% Nd:YAG	Spherical	$1.0\mu m$	$9.5x10^7$

Table 4.8: Summary of ADA coefficients used in Kubelka-Munk Model.

4.3 Fluorescence

4.3.1 Calibration of Fluorescence Line Width Results

Frequency calibration of fluorescence optical setup is maintained using Argon and Krypton wavelength calibration sources. Corrections must be made for changes in grating dispersion as a function of wavelength. Intensity calibration of fluorescence derived line width is relatively complicated. Calibration is performed by coupling a known source, such as a blackbody, and normalizing the optical system response. This calibration cannot provide a fluorescence zero baseline.

4.3.2 Fluorescence Line width Results

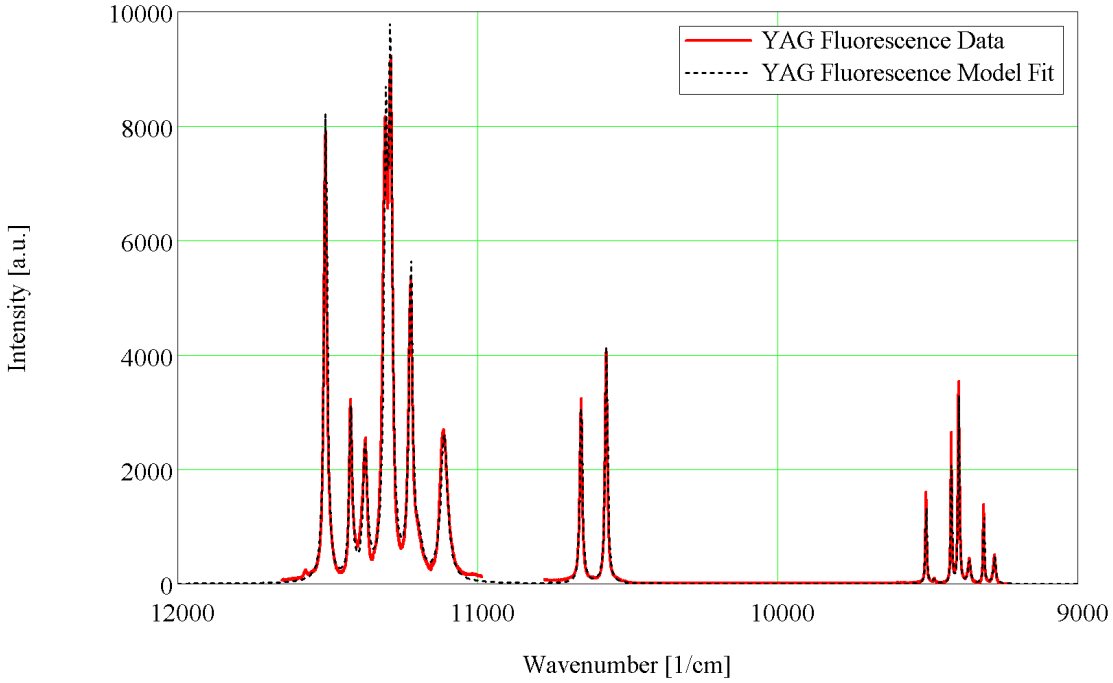

Figure 4.23: Fluorescence model for 1% Nd doped polycrystalline YAG collected at $293K$.

Fluorescence data was collected from 1% Nd doped polycrystalline YAG and a Lorentz line shape classical oscillator model was fit to all fluorescence features from the Nd:YAG ${}^4I_{9/2} \rightarrow {}^4F_{3/2}$, and ${}^4I_{11/2} \rightarrow {}^4F_{3/2}$ transitions. The fluorescence model is shown in Fig. 4.23. A summary of fluorescence model parameters is shown in Table 4.9.

Line Position $[1/cm]$	Line Strength $[a.u.]$	Line Width $[1/cm]$ FWHM
11507	163000	6.2
11423	55000	5.8
11375	60000	8.4
11307	162000	7.2
11291	192000	7.2
11223	124000	7.4
11196	24000	14.5
11112	108000	13.5
10655	47000	4.7
10571	62500	4.6
9505	11300	2.3
9479	800	3.2
9421	15600	1.9
9397	18500	2.1
9395	7700	2
9361	6600	5.2
9313	9600	2.2
9277	6900	4.6
9046	*	*
8993	*	*
8962	*	*
8909	*	*

Table 4.9: Summary of fluorescence derived strengths and line widths at $293K$ for polycrystalline 1% Nd doped YAG. An astrict indicates insufficient line strength for room temperature measurement.

Chapter 5

Implications

5.1 Transmittance

5.1.1 Parasitic Absorbers in Polycrystalline YAG

Polycrystalline YAG material has several properties that make it superior to single crystal YAG. Advantages of polycrystalline material include larger physical dimensions, higher Nd doping percentages including tailored doping profiles[18] and recently reduced scatter at the $1.064\mu m$ lasing wavelength.[19] The production process of polycrystalline YAG also presents several challenges. Polycrystalline material requires extremely pure precursor powders and processing environment. The precursor powder has an very large surface area and is susceptible to contamination. Any impurities in the precursor material, or added from production equipment, will be present in the

final polycrystalline material. Impurities in the final material may lead to parasitic absorption features, as was shown in the extinction coefficient from Section 3.1.1. Konoshima has done an excellent job in reducing parasitic absorbers in polycrystalline material near the $1.064\mu m$ transition. Parasitic absorbers near the $0.946\mu m$ transition may result in degraded performance when lasing at this transition. Reduction of parasitic absorbers will mitigate a power loss mechanism. This is particularly important as intra cavity losses are magnified by the multiple passes of a resonator.

5.1.2 Improved Performance of $0.946\mu m$ Nd:YAG at Cryogenic Temperatures

Lasing on the $0.946\mu m$ transition is inherently less efficient than the $1.064\mu m$ transition in Nd doped YAG. Part of this reduced efficiency is due to the quasi four level nature of the $0.946\mu m$ transition. The lower lasing level is $852cm^{-1}$ above ground state for the $0.946\mu m$ transition. At $852cm^{-1}$ the thermal population is 0.7% at room temperature, population that must be overcome to permit lasing. The lower lasing level is $2110cm^{1}$ above ground state for the $1.064\mu m$ and contains negligible thermal population at room temperature. Operating a $0.946\mu m$ Nd:YAG laser gain media at cryogenic temperatures will reduce the lower lasing level thermal population. Sustaining cryogenic temperatures requires overcoming significant laser thermal engineering challenges, therefore operating at excessively cold temperatures should be avoided.

The suggested operating temperature is near where the temperature independent scatter coefficient dominates over the temperature dependent absorption coefficient. Operating at colder temperatures will provide negligible additional benefit.

5.1.3 Simplified Laser Pumping at Wavelengths of Greater Absorption

The first Nd:YAG laser resonator designs were rod configuration to permit efficient flashlamp pump coupling.[1] Flashlamp pumping schemes have been replaced with diode pumped designs in most new solid state lasers. The use of diode pumping has permitted a wider range of resonator configurations based around shorter rod, slab, and disk shaped gain media. These modified resonators often provide increased efficiency but result in shorter gain media length than traditional rod laser designs. To maintain the same pump level, a shorter gain media length will require a multi pass pumping configuration or greater absorptance of the pump wavelength. Diode pumping has the ability to tailor the pump wavelength to use pump features of higher absorptance. Using wavelengths of maximum pump absorptance will reduce the gain media path length required for the same pump power while simplifying the resonator pump configuration.

5.2 Scatterance

5.2.1 Polycrystalline Preferred Over Single Crystal YAG Material

Single crystal Nd doped YAG has been available since the 1960s. Since that time, the material properties have been optimized significantly and YAG material has become integral to a widely used laser. Polycrystalline Nd doped YAG is a relatively new material. The polycrystalline YAG manufacturing process has been updated to improve the final material quality.[35] The analysis of scatterance measurements from Section 4.2 reveals that the scatter coefficient is lower for polycrystalline YAG than single crystal YAG at the $1.064\mu m$ transition. This low level of scatter indicates that polycrystalline YAG material is mature and should be preferered over single crystal material.

5.2.2 Reduced Scatter by Index Matching Sintering Agent

Addition of a sintering agent to the polycrystalline YAG production process has substantially reduced the residual porosity of polycrystalline YAG material.[3534] The sintering agent was confirmed to be silicon based using inductively coupled plasma

mass spectrometry (ICP-MS) measurements. The residual sintering agent forms silica along the grain boundaries during the hot isostatic press and high temperature vacuum sintering production phases. The index of silica is $n = 1.45$ at $1.064\mu m$, the index of YAG is $n = 1.815$ at $1.064\mu m$. This index difference is a significant source of scatter in Konoshima polycrystalline YAG material. A replacement sintering agent with similar densification success and the resultant compound with a resultant index closer to YAG would be ideal. Better index matching between the YAG grains and residual sintering agent would reduce this source of scatter.

5.3 Fluorescence

5.3.1 Gain Bandwidth and Picosecond Pulses

For passive mode locked laser operation the minimum pulse length is driven by the bandwidth of the transition, Eq 5.1, where Δt_p is the pulse width in time and $\Delta\nu$ is the bandwidth in frequency.

$$\Delta t_p \approx \frac{1}{\Delta\nu} \tag{5.1}$$

The minimum known pulse length from a Nd:YAG laser resonator operating on the $1.064\mu m$ Nd:YAG transition is $8.3ps$.[55] Examining the data provided in section 4.1.3.5, it is apparent the room temperature line width of the $1.061\mu m$ transition is

broader for polycrystalline versus single crystal YAG. The single crystal 1% Nd doped YAG line width was reported at $5.0 cm^{-1} FWHM$.[14] The minimum pulse length at $1.064 \mu m$, based on Eq. 5.1, should be roughly $3.6 ps$ and $6.7 ps$ for polycrystalline and single crystal respectively. The bandwidth of the $0.946 \mu m$ transition is greater than at $1.064 \mu m$. The minimum pulse length should be $2.8 ps$ and $3.7 ps$ respectively. If minimum pulse length is a significant laser design concern, polycrystalline Nd:YAG material should be preferred over single crystal. Further temporal pulse narrowing benefits should be possible when switching from the $1.064 \mu m$ to $0.964 \mu m$ Nd:YAG transition.

Chapter 6

Conclusions and Summary

6.1 Trasmittance

The optical properties of Konoshima polycrystalline YAG are suitable for laser applications. Notable differences between polycrystalline and single crystal include a greater extinction coefficient for undoped and 1% Nd doped Konoshima polycrystalline YAG at $1.064\mu m$. This increased extinction coefficient is most likely due to residual parasitic absorbers.

A temperature dependent polycrystalline Nd doped YAG line width model is applied. Temperature dependent line width model fits are presented for several transitions of interest. Increased bandwidth of polycrystalline versus single crystal material is revealed. Model locked lasers based on polycrystalline Nd:YAG are capable of shorter picosecond pulses that single crystal Nd:YAG material.

The temperature dependant extinction coefficient data and model at 946nm indicates the Konoshima polycrystalline YAG extinction coefficient is scatter dominant below 230 K. Cooling the gain media for efficiency improvements will be limited below this scatter floor. A classical oscillator model providing the location, strength, and width of the diode pump bands in Nd:YAG is developed.

6.2 Scatter

We find that the extrinsic scatter properties of polycrystalline Nd:YAG is equivalent or superior to the single crystal Nd:YAG investigated here. The scatter coefficient at $1.064\mu m$ is roughly 25% less in polycrystalline vs. a single crystal material. Scatter could be further reduced by better matching the index of the sintering agent with the polycrystalline material. A Kubelka Munk wavelength dependant scatter coefficient model for polycrystalline and single crystal YAG is presented. Scatter coefficient data collected at discrete wavelengths is fit to the Kubelka Munk wavelength dependant model with excellent result. The scatter coefficient for undoped polycrystalline YAG at $1.064\mu m$ was measured at $\beta_{sca} = 0.007\ [1/cm]$. From modeling we calculate the scatter coefficient for undoped polycrystalline YAG at $0.946\mu m$ at $\beta_{sca} = 0.008\ [1/cm]$.

6.3 Fluorescence

Absorption and fluorescence derived line width measurements of 1% Nd doped YAG were performed. Results from two different technique provide comparable results. Calibration of absorption derived line width measurements is much less prone to error than fluorescence derived measurements.

6.4 Future Work

Future work will include laser calorimetry measurements and modeling to directly verify absorption at 1064nm. Further line shift measurements and modeling of the temperature dependent line shift are planned.

All characterization work above will be incorporated into complete laser design model. A laser based on the $0.946\mu m$ transition in Nd:YAG will be constructed.

Chapter 7

Appendix

7.1 Additional Transmittance Figures

Transmittance data was collected in the $1,000cm^{-1}$ to $51,000cm^{-1}$ spectral range using two seperate instruments. A BOMEM DA3.02 Fourier Transform Spectrometer is used in the $12,500cm^{-1}$ to $1000cm^{-1}$ ($0.8\mu m$ to $10\mu m$) spectral region. In the $1,000cm^{-1}$ to $51,000cm^{-1}$ spectral range. A Globar source, KBr beam splitter and MCT detector are used from $4000cm^{-1}$ to $1000cm^{-1}$. A quartz-halogen lamp, quartz beam splitter, and InSb detector are used from $9000cm^{-1}$ to $4000cm^{-1}$. A quartz-halogen lamp, quartz beam splitter, and Si detector are used from $12,500cm^{-1}$ to $9000cm^{-1}$. Please note thinner 0.75 mm samples doped polycrystalline samples were used for the $11,020cm^{-1}$ to $12,500cm^{-1}$ region to prevent saturation of absorption features. Measurements in the $12,500cm^{-1}$ to $1000cm^{-1}$ spectral range are performed

under 0.5 - 2 torr vacuum to remove water vapor and carbon dioxide absorption bands. A PerkinElmer Lambda 950 Grating Spectrometer is used in the $0.19\mu m$ to $0.8\mu m$ ($52,500cm^{-1}$ to $12,500cm^{-1}$) spectral region. Figures 7.1, 7.2, 7.3, 7.4, 7.5, 7.6, and 7.7 show the complete visible to near infrared window of transmittance and the spectral range of each detector used in undoped, 1%, 1.5%, 2%, 4%, 6%, and 10% doped polycrystalline YAG, respectively.

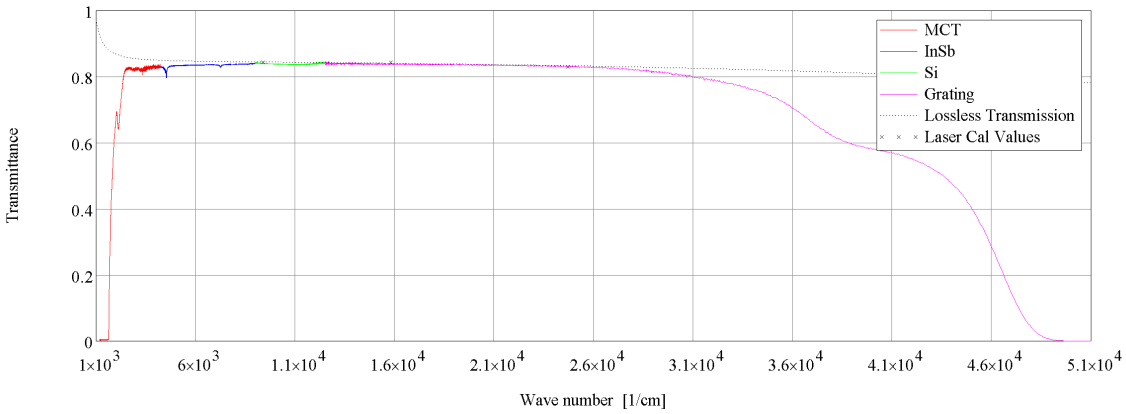

Figure 7.1: Konoshima polycrystalline undoped YAG transmittance, multiple detectors, at room temperature.

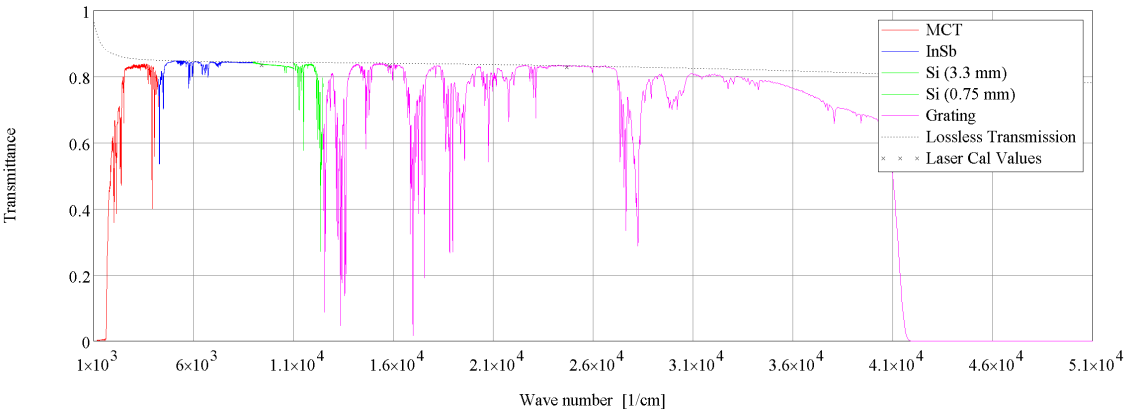

Figure 7.2: Konoshima polycrystalline 1% Nd doped YAG transmittance, multiple detectors, at room temperature.

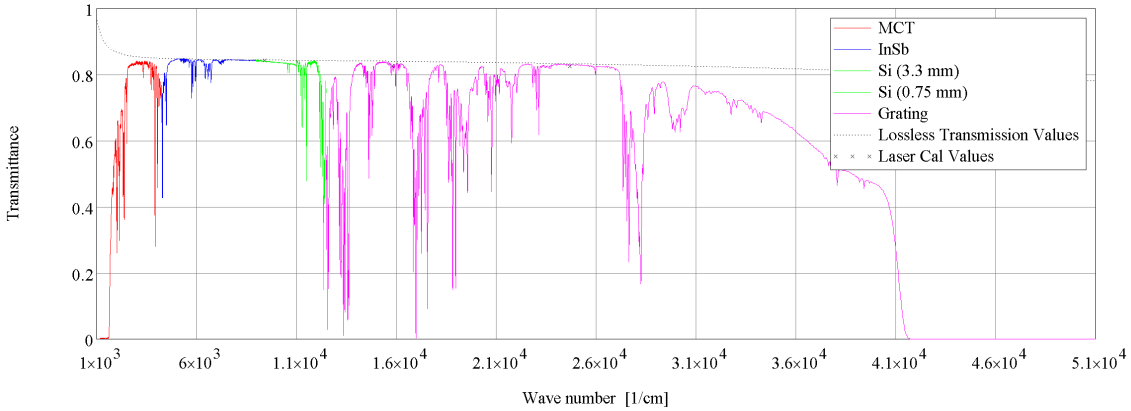

Figure 7.3: Konoshima polycrystalline 1.5% Nd doped YAG transmittance, multiple detectors, at room temperature.

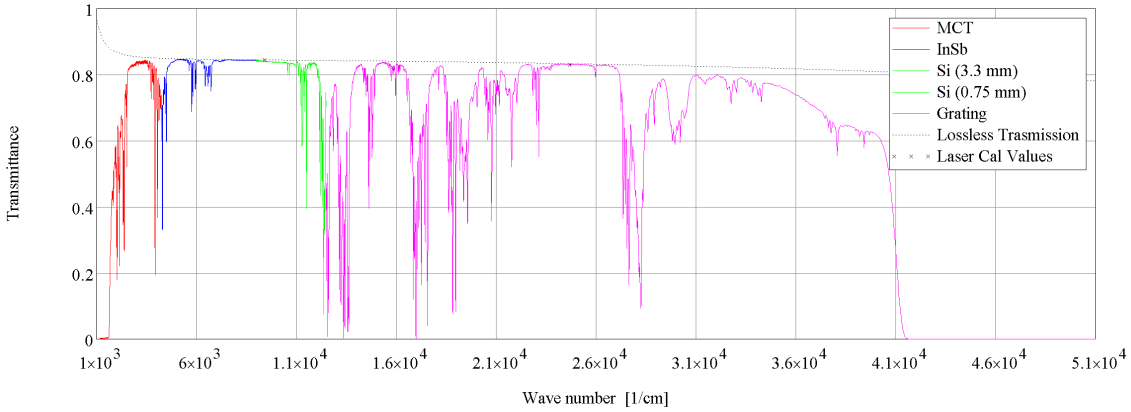

Figure 7.4: Konoshima polycrystalline 2% Nd doped YAG transmittance, multiple detectors, at room temperature.

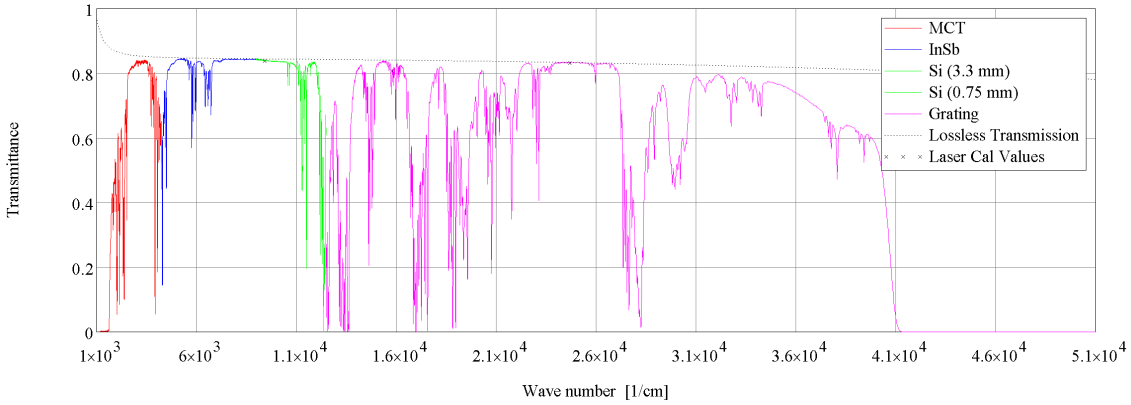

Figure 7.5: Konoshima polycrystalline 4% Nd doped YAG transmittance, multiple detectors, at room temperature.

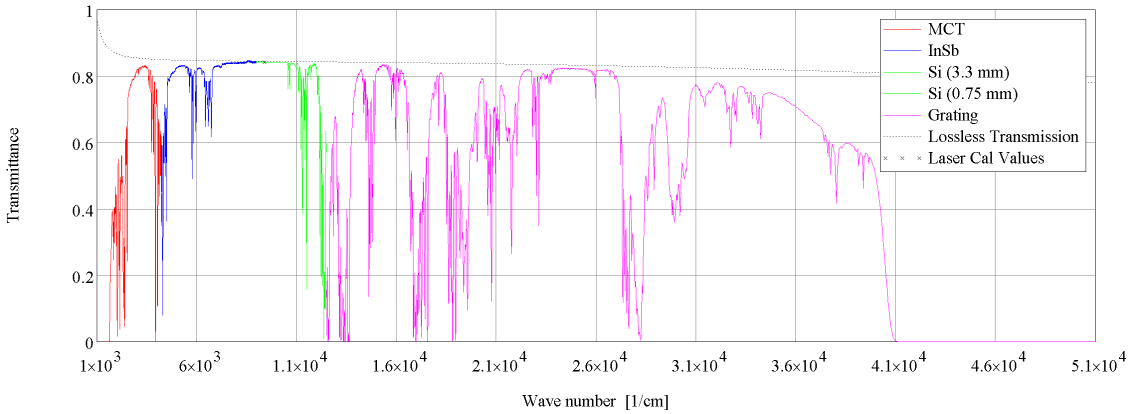

Figure 7.6: Konoshima polycrystalline 6% Nd doped YAG transmittance, multiple detectors, at room temperature.

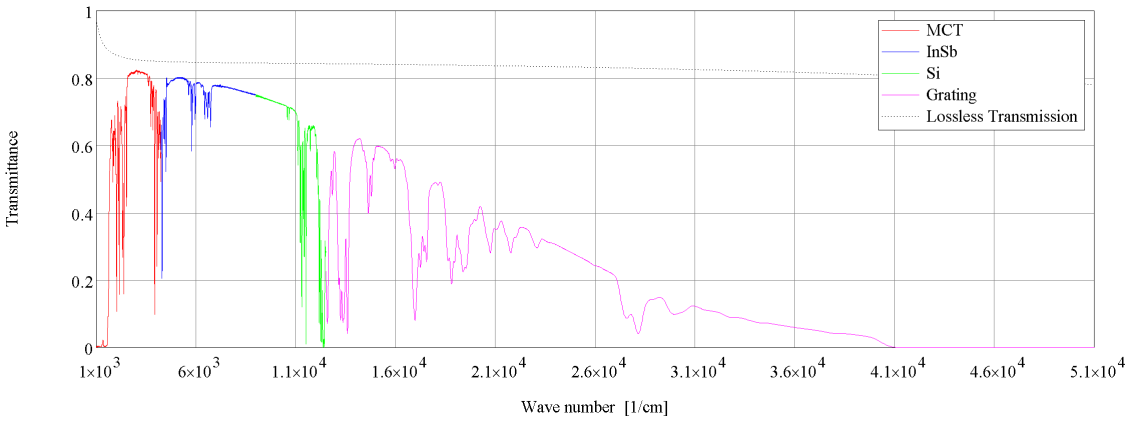

Figure 7.7: Konoshima polycrystalline 10% Nd doped YAG transmittance, multiple detectors, at room temperature.

Figures 7.8 and 7.9 show the complete visible to near infrared window of transmittance and the spectral range of each detector used in undoped and 1% doped single crystal YAG, respectively.

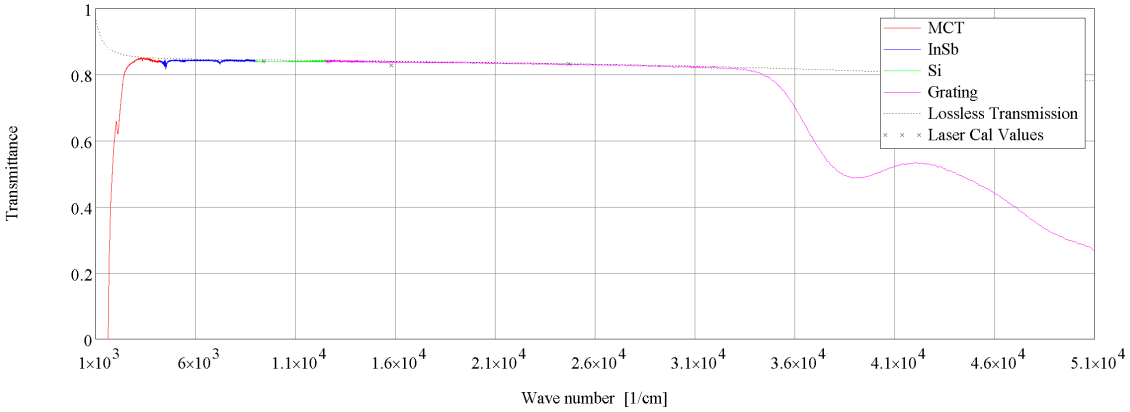

Figure 7.8: United Crystals single crystal undoped YAG transmittance, multiple detectors, at room temperature.

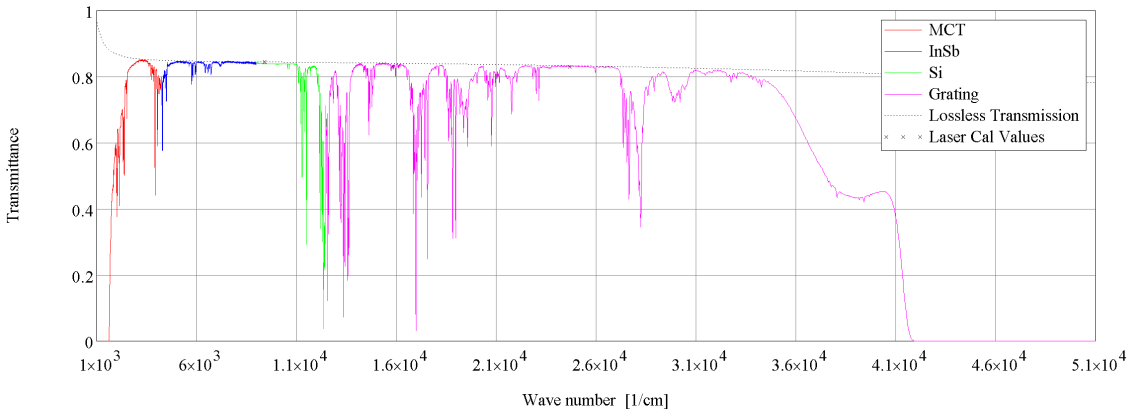

Figure 7.9: United Crystals single crystal 1% Nd doped YAG transmittance, multiple detectors, at room temperature.

7.2 Additional SEM Figures

The grain structure of the polycrystalline material was imaged using a scanning electron microscope (SEM). Images for each polycrystalline YAG sample are provided in Figures 7.10, 7.11, 7.12, 7.13, 7.14, and 7.15. The Heyn Linear Intercept Procedure was used to determine mean grain size. Additional details on the measurement procedure are detailed in ASTM E112-10 Standard Test Methods for Determining Average Grain Size.[28] A summary of grain size is included in Table 4.7.

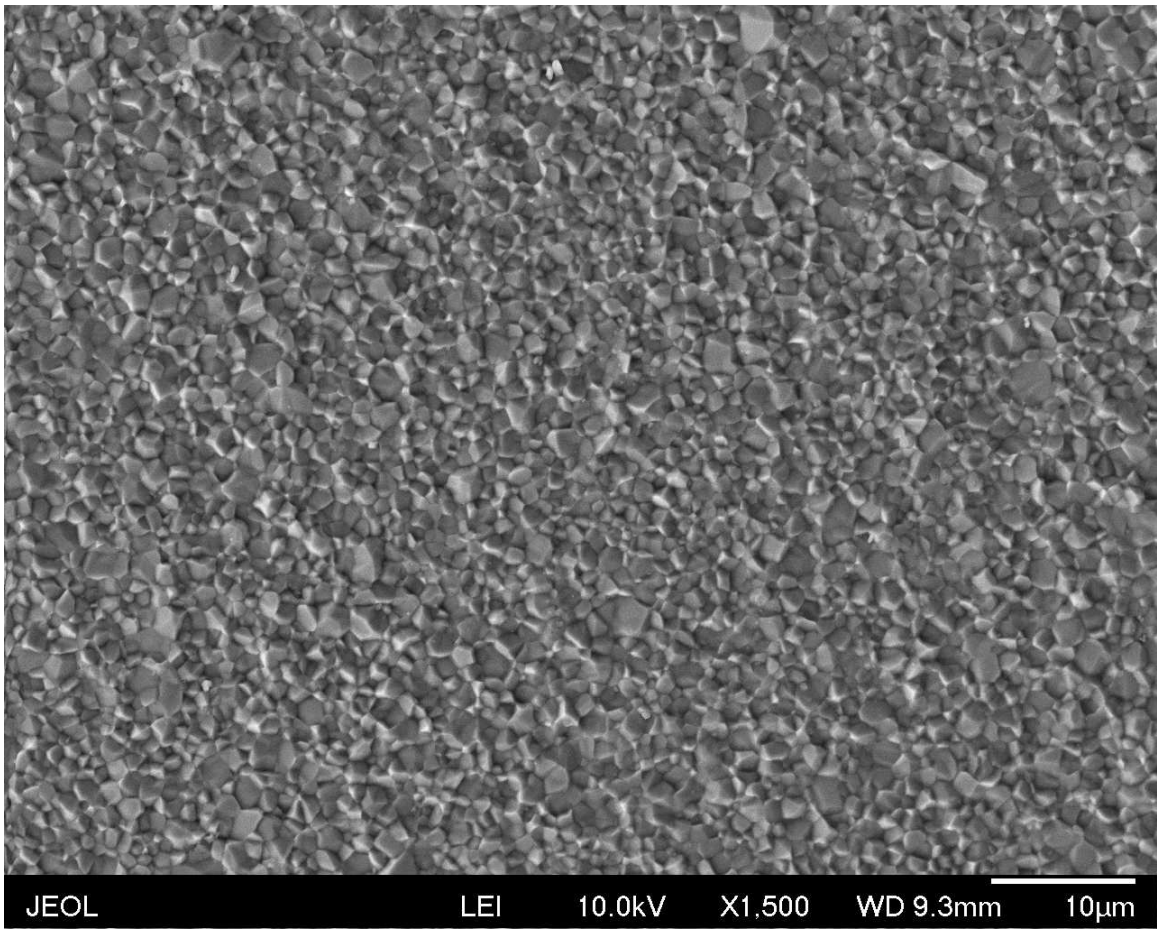

Figure 7.10: SEM image of undoped polycrystalline YAG.

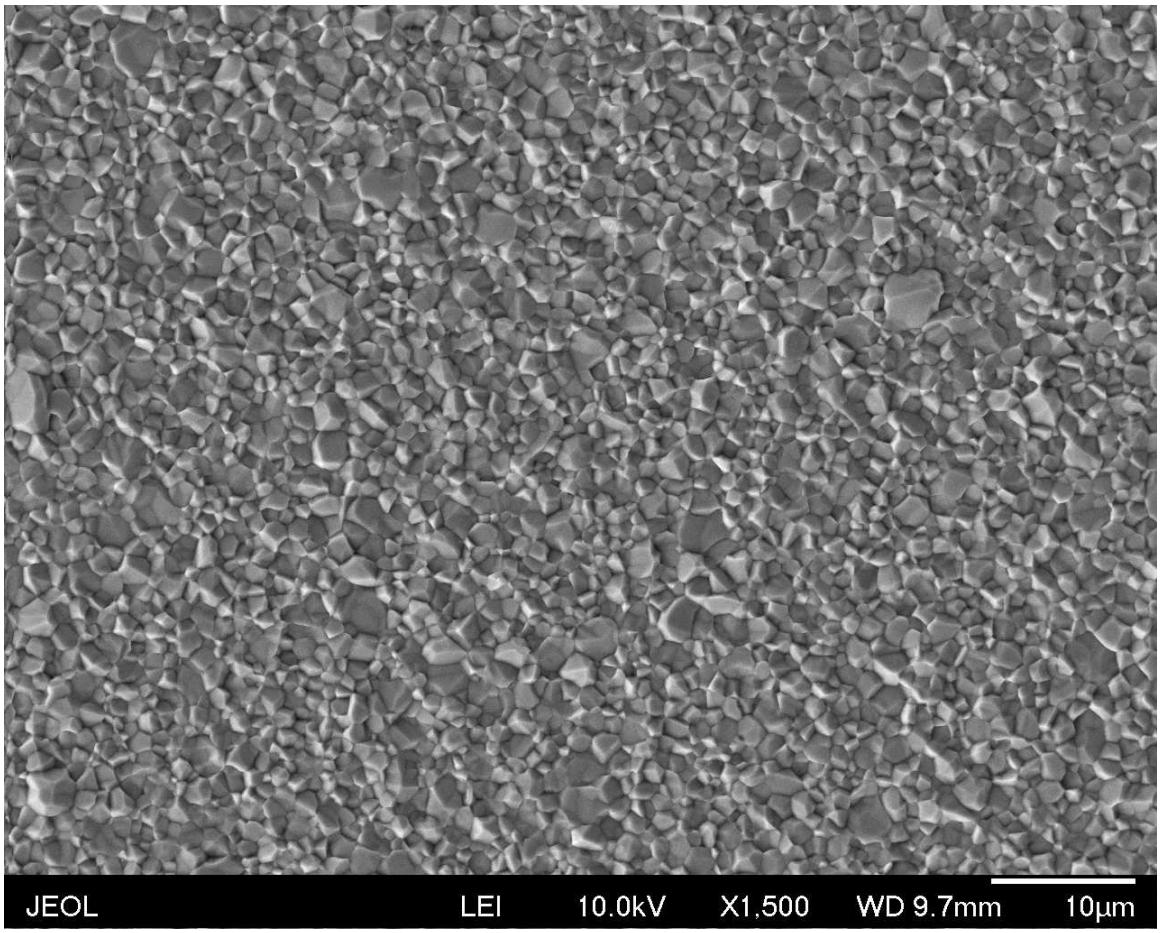

Figure 7.11: SEM image of 1% Nd doped polycrystalline YAG.

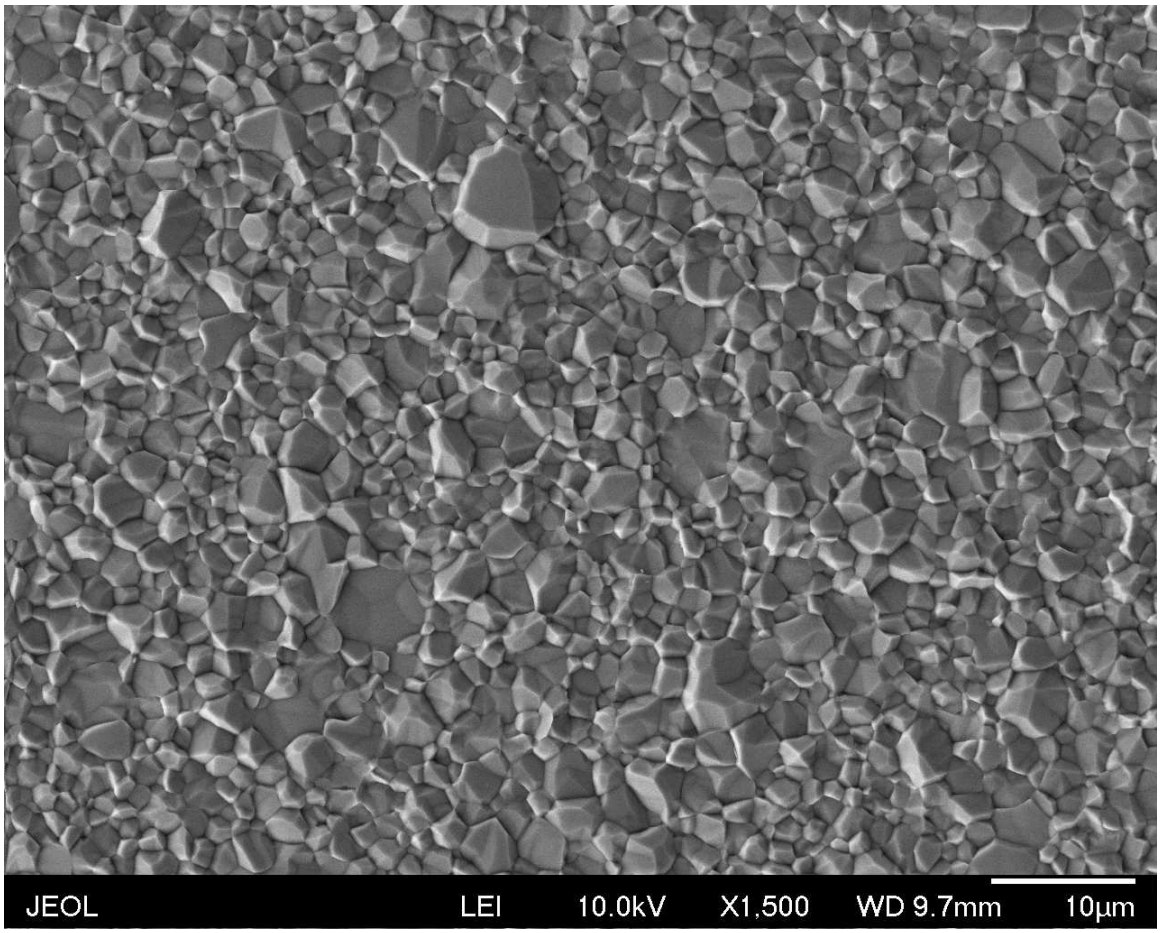

Figure 7.12: SEM image of 1.5% Nd doped polycrystalline YAG.

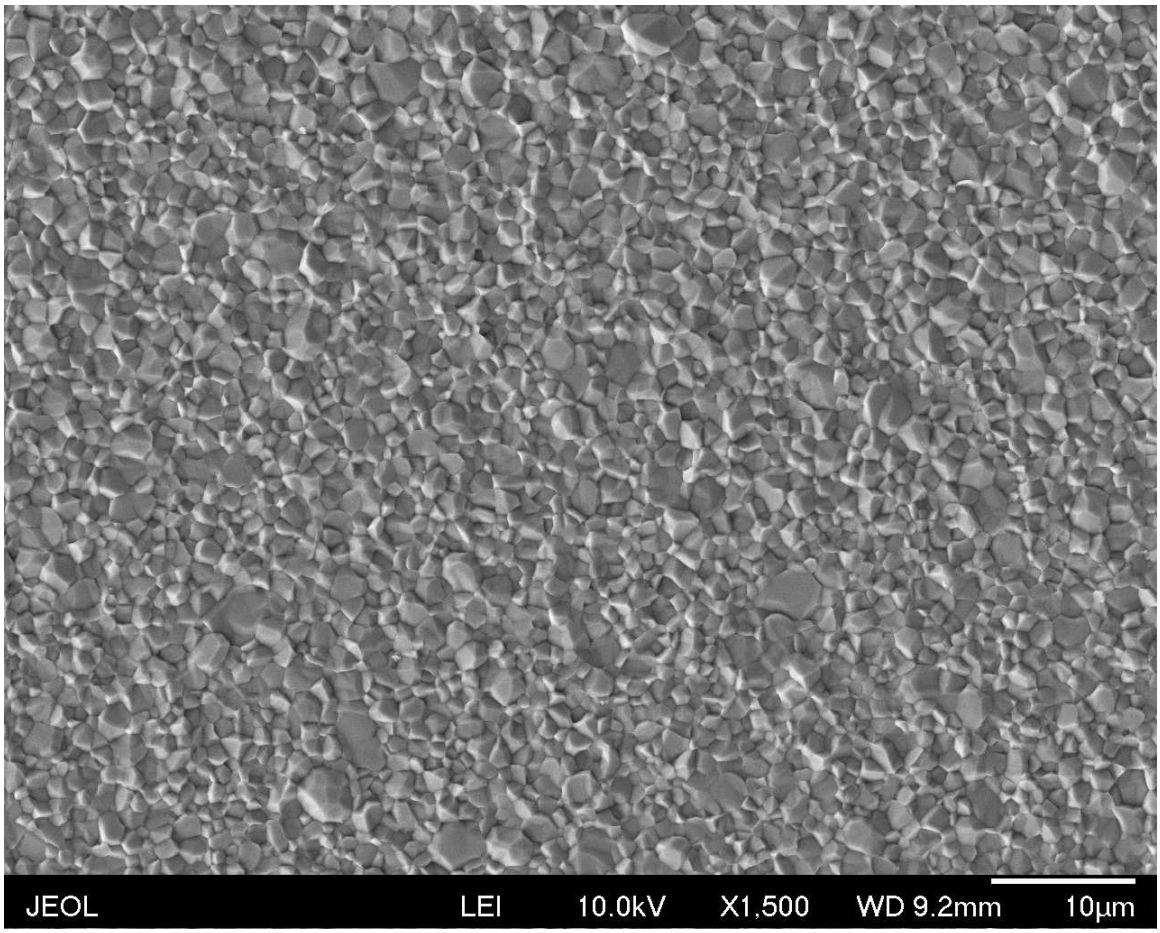

Figure 7.13: SEM image of 2% Nd doped polycrystalline YAG.

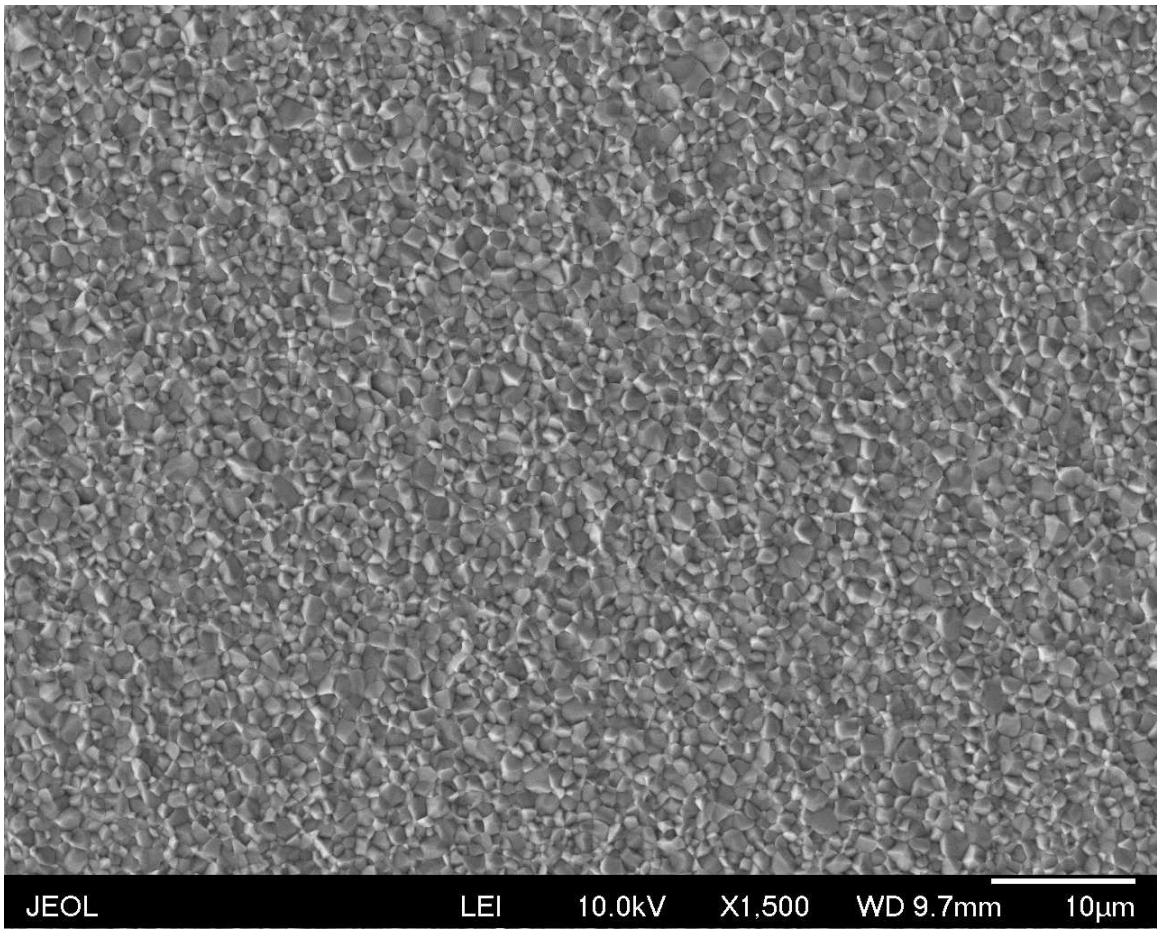

Figure 7.14: SEM image of 4% Nd doped polycrystalline YAG.

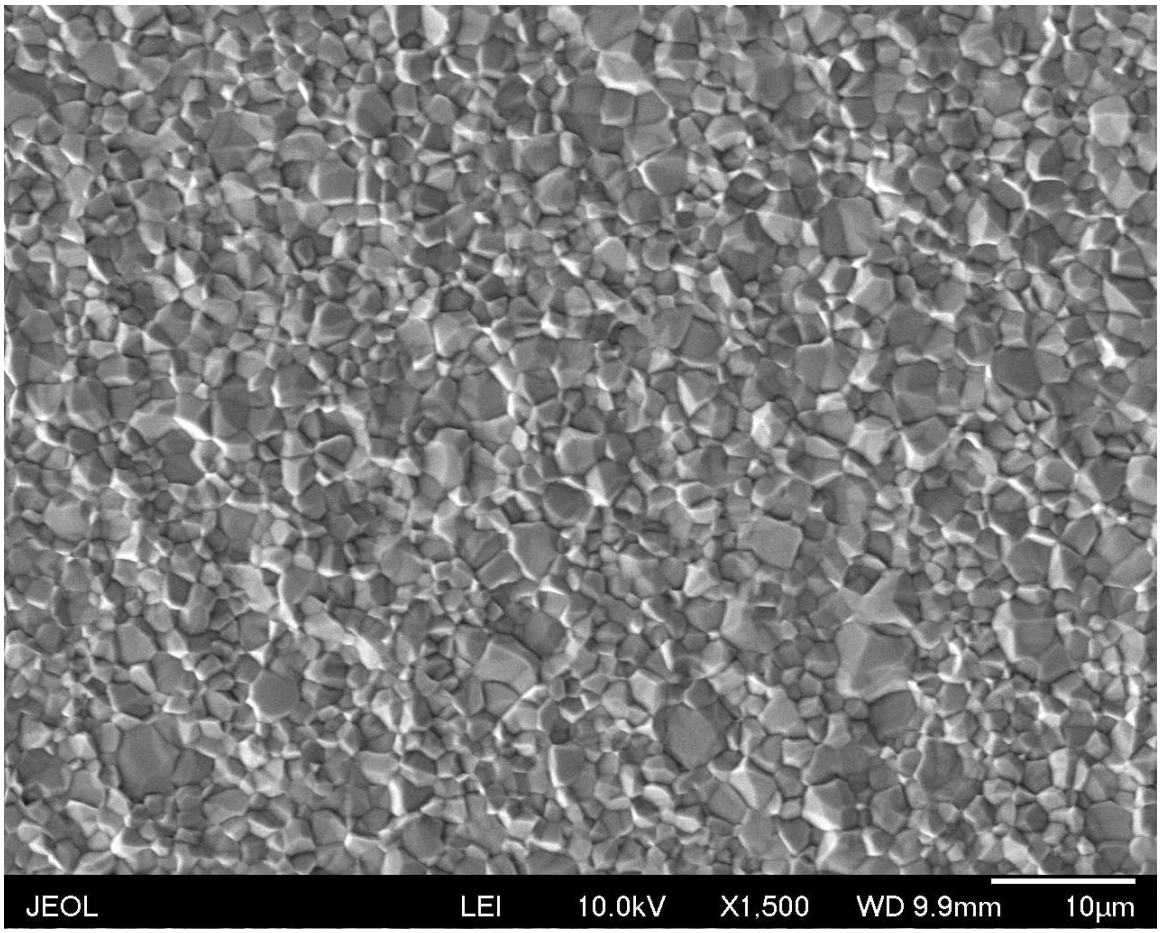

Figure 7.15: SEM image of 6% Nd doped polycrystalline YAG.

Bibliography

[1] J. E. Geusic et al., "Laser oscillations in Nd doped yttrium aluminum, yttrium gallium and gadolinium garnets," Applied Physics Letters, vol. 4, no. 10, pp. 182–184, 1964.

[2] R. W. Wallace and S. E. Harris, "Oscillation and doubling of the 0.946-μm line in Nd3+:YAG," Applied Physics Letters, vol. 15, no. 4, pp. 111–112, 1969.

[3] N. Jerlov, Marine Optics. New York, NY: Elsevier Science, 1976.

[4] R. W. Austin and T. J. Petzold, "Spectral dependence of the diffuse attenuation coefficient of light in ocean waters," Optical Engineering, vol. 25, no. 3, pp. 253 471–253 471–, 1986.

[5] T. J. Axenson et al., "High-energy Q-switched 0.946-μm solid-state diode pumped laser," J. Opt. Soc. Am. B, vol. 19, no. 7, pp. 1535–1538, Jul 2002.

[6] Y. Chen et al., "Intracavity frequency doubling of an active Q-switched Nd:YAG

laser with 2.25w output power at 473nm," Optics Communications, vol. 270, no. 1, pp. 58 – 62, 2007.

[7] J. K. Neeland and V. Evtuhov, "Measurement of the laser transition cross section for nd^{+3} in yttrium aluminum garnet," Phys. Rev., vol. 156, pp. 244–246, Apr 1967.

[8] T. Kushida et al., "Laser transition cross section and fluorescence branching ratio for nd^{3+} in yttrium aluminum garnet," Phys. Rev., vol. 167, pp. 289–291, Mar 1968.

[9] T. Kushida, "Linewidths and thermal shifts of spectral lines in neodymium-doped yttrium aluminum garnet and calcium fluorophosphate," Phys. Rev., vol. 185, pp. 500–508, Sep 1969.

[10] S. Singh et al., "Stimulated-emission cross section and fluorescent quantum efficiency of nd^{3+} in yttrium aluminum garnet at room temperature," Phys. Rev. B, vol. 10, pp. 2566–2572, Sep 1974.

[11] A. A. Kaminskii, Laser crystals. New York, NY: Springer-Verlag, Jan 1990.

[12] D. Brown, "Heat, fluorescence, and stimulated-emission power densities and fractions in nd:yag," Quantum Electronics, IEEE Journal of, vol. 34, no. 3, pp. 560–572, Mar 1998.

[13] N. P. Barnes and B. M. Walsh, "Amplified spontaneous emission-application

to nd: Yag lasers," Quantum Electronics, IEEE Journal of, vol. 35, no. 1, pp. 101–109, 1999.

[14] J. T. Verdeyen, Laser Electronics. Englewood Cliffs, NJ, USA: Prentice-Hall, 1995.

[15] W. Koechner, Solid State Laser Engineering. New York, NY, USA: Springer-Verlag, 2006.

[16] A. Kaminskii, Crystalline Lasers: Physical Processes and Operating Schemes. Boca Raton, FL: CRC Press, 1996.

[17] W. P. Risk and W. Lenth, "Room-temperature, continuous-wave, 946-nm Nd:YAG laser pumped by laser-diode arrays and intracavity frequency doubling to 473 nm," Opt. Lett., vol. 12, no. 12, pp. 993–995, Dec 1987.

[18] R. Springer and M. Thomas, "Analysis and comparison of single crystal and polycrystalline Nd:YAG, absorption," Quantum Electronics, IEEE Journal of, vol. 49, no. 8, pp. 667–676, 2013.

[19] R. Springer et al., "Analysis and comparison of single crystal and polycrystalline Nd:YAG, scatter," Quantum Electronics, IEEE Journal of, vol. 51, no. 8, 2015.

[20] D. E. McCumber and M. D. Sturge, "Linewidth and temperature shift of the r lines in ruby," Journal of Applied Physics, vol. 34, no. 6, pp. 1682–1684, 1963.

[21] A. Ikesue, "Polycrystalline Nd:YAG ceramics lasers," Optical Materials, vol. 19, no. 1, pp. 183 – 187, 2002.

[22] M. D. J. Wisdom and R. L. Byer, "Ceramic lasers: ready for action," Photon. Spectra, vol. 28, no. 2, pp. 50–55, Feb 2004.

[23] T. Taira, "Re3+ ion doped yag ceramic lasers," Selected Topics in Quantum Electronics, IEEE Journal of, vol. 13, no. 3, pp. 798–809, 2007.

[24] D. Kracht et al., "Comparison of crystalline and ceramic composite Nd:YAG for high power diode end-pumping," Opt. Express, vol. 13, no. 16, pp. 6212–6216, Aug 2005.

[25] L. D. Merkle et al., "Concentration quenching in fine-grained ceramic Nd:YAG," Opt. Express, vol. 14, no. 9, pp. 3893–3905, May 2006.

[26] C. Jacinto et al., "Microstructuration induced differences in the thermo-optical and luminescence properties of Nd:YAG fine grain ceramics and crystals," The Journal of Chemical Physics, vol. 129, no. 10, 2008.

[27] A. Benayas et al., "Luminescence quantum efficiency of Nd:YAG garnet laser ceramics determined by pump-induced line broadening," Quantum Electronics, IEEE Journal of, vol. 46, no. 12, pp. 1870–1876, 2010.

[28] A. S. E112-13, "Standard test methods for determining average grain size." West Conshohocken, PA: ASTM International, 2010.

[29] H. Yagi et al., "The physical properties of composite YAG ceramics," Laser Physics, vol. 15, no. 9, pp. 1338–1344, 2005.

[30] H. Furuse et al., "Thermo-optic properties of ceramic yag at high temperatures," Opt. Mater. Express, vol. 4, no. 9, pp. 1794–1799, Sep 2014.

[31] J. D. Foster and L. M. Osterink, "Thermal effects in a nd:yag laser," Journal of Applied Physics, vol. 41, no. 9, pp. 3656–3663, 1970.

[32] W. Koechner and D. Rice, "Effect of birefringence on the performance of linearly polarized yag:nd lasers," Quantum Electronics, IEEE Journal of, vol. 6, no. 9, pp. 557–566, Sep 1970.

[33] Q. Lu et al., "Photoelastic effects in nd:yag rod and slab lasers," Optics and Laser Technology, vol. 27, no. 2, pp. 95 – 101, 1995.

[34] A. Ikesue et al., "Optical scattering centers in polycrystalline Nd:YAG laser," Journal of the American Ceramic Society, vol. 80, no. 6, pp. 1517–1522, 1997.

[35] J. Lu et al., "Development of Nd:YAG ceramic lasers," Advanced Solid-State Lasers, p. WE1, 2002.

[36] M. E. Thomas, Optical Propagation in Linear Media. London, UK: Oxford University Press, 2006.

[37] E. F. Zalewski, "NBS measurement series: The NBS photodetector spectral

response calibration transfer program." Washington, DC, USA: National Bureau of Standards, Mar 1988.

[38] M. Bass et al., Handbook of Optics, Third Edition Volume II: Design, Fabrication and Testing, Sources and Detectors, Radiometry and Photometry (Set), 3rd ed. New York, NY, USA: McGraw-Hill, Inc., 2010.

[39] A. Kramida et al. (2014, September) NIST atomic spectra database (version 5.2). Gaithersburg, MD.

[40] T. Kushida and M. Kikuchi, "R, r' and b absorption linewidths and phonon-induced relaxations in ruby," Journal of the Physical Society of Japan, vol. 23, no. 6, pp. 1333–1348, 1967.

[41] T. Y. Fan and R. Byer, "Modeling and CW operation of a quasi-three-level 946 nm Nd:YAG laser," Quantum Electronics, IEEE Journal of, vol. 23, no. 5, pp. 605–612, 1987.

[42] M. E. Thomas and D. D. Duncan, "BRDF and BSDF models for diffuse surface and bulk scatter from transparent windows," Proc. SPIE, vol. 6545, 2007.

[43] D. D. Duncan et al., "Physics-based polarimetric BRDF models," Proc. SPIE, vol. 5192, pp. 129–140, 2003.

[44] F. Zernike, "The concept of degree of coherence and its application to optical problems," Physica, vol. 5, no. 8, pp. 785 – 795, 1938.

[45] J. W. Goodman, Statistical Optics. New York, NY: John Wiley and Sons, Inc, 1984.

[46] M. E. Thomas et al., "Optical properties of Nd doped and undoped polycrystalline YAG," Proc. SPIE, vol. 6545, pp. 65 450F–65 450F–8, 2007.

[47] H. C. van de Hulst, Light Scattering by Small Particles. New York, NY, USA: Dover Publications, 1957.

[48] R. Boulesteix et al., "Mechanism of the liquid-phase sintering for nd:yag ceramics," Optical Materials, vol. 31, no. 5, pp. 711 – 715, 2009.

[49] R. Boulesteix, "The effect of silica doping on neodymium diffusion in yttrium aluminum garnet ceramics: implications for sintering mechanisms," Journal of the European Ceramic Society, vol. 29, no. 12, pp. 2517 – 2526, 2009.

[50] A. Matre et al., "Effect of silica on the reactive sintering of polycrystalline Nd:YAG ceramics," Journal of the American Ceramic Society, vol. 91, no. 2, pp. 406–413, 2008.

[51] V. J. Morris and B. R. Jennings, "Anomalous diffraction approximation to the low-angle scattering from coated spheres: a model for biological cells," Biophysical Journal, vol. 17, no. 1, pp. 95–101, 1977.

[52] S. S. Strong et al., "Improving earth background characterization through mod-

eling and measurements of leaf bidirectional reflectivity," Johns Hopkins APL Technical Digest, vol. 32, no. 5, pp. 787–802, 2014.

[53] R. I. Joseph and M. E. Thomas, "How accurate is the Kubelka-Munk theory of diffuse reflection? A quantitative answer," Proc. SPIE, vol. 8495, pp. 84 950I–84 950I–9, 2012.

[54] A. Ikesue and K. Yoshida, "Influence of pore volume on laser performance of Nd:YAG ceramics," Journal of Materials Science, vol. 34, no. 6, pp. 1189–1195, 1999.

[55] L. Guo et al., "Diode-end-pumped passively mode-locked ceramic nd:yag laser with a semiconductor saturable mirror," Opt. Express, vol. 13, no. 11, pp. 4085–4089, May 2005.

Vita

Ryan M. Springer holds a B.S degree in Electrical Engineering from the University of Texas, Austin and a M.S.E. degree in Electrical Engineering from Johns Hopkins University. Since 2010 he has been working on his PhD in the Department of Electrical and Computer Engineering at Johns Hopkins University. He currently works at the Naval Air Warfare Center, Patuxent River MD as an Electrical Engineer in E.O. and Special Mission Sensors Division.

His research interests include solid state laser materials and lasers emitting in the blue. He currently has two IEEE Journal of Quantum Electronics publications *Analysis and comparison of single crystal and polycrystalline Nd:YAG, absorption* and *Analysis and comparison of single crystal and polycrystalline Nd:YAG, scatter.* This work was supported by the U.S. Department of Defense, Naval Air Warfare Center Aircraft Division, Section 219 Naval Innovative Science and Engineering (NISE) Workforce Development program and the Applied Physics Laboratory, Johns Hopkins University, Laurel, MD, USA.